HAL
open science

Improvement and integration of the in-situ heat pump performance assessment method

Maria Niznik

To cite this version:

Maria Niznik. Improvement and integration of the in-situ heat pump performance assessment method. Fluids mechanics [physics.class-ph]. Université Paris sciences et lettres, 2017. English. NNT : 2017PSLEM029 . tel-01753394

HAL Id: tel-01753394

https://pastel.hal.science/tel-01753394v1

Submitted on 29 Mar 2018

HAL is a multi-disciplinary open access archive for the deposit and dissemination of scientific research documents, whether they are published or not. The documents may come from teaching and research institutions in France or abroad, or from public or private research centers.

L'archive ouverte pluridisciplinaire **HAL**, est destinée au dépôt et à la diffusion de documents scientifiques de niveau recherche, publiés ou non, émanant des établissements d'enseignement et de recherche français ou étrangers, des laboratoires publics ou privés.

THÈSE DE DOCTORAT

de l'Université de recherche Paris Sciences et Lettres
PSL Research University

Préparée à MINES ParisTech

Improvement and integration of the in-situ heat pump performance assessment method

Amélioration et intégration d'une méthode d'affichage des performances en temps réel d'une pompe à chaleur

Ecole doctorale n°432

SMI - SCIENCES DES MÉTIERS DE L'INGÉNIEUR

Spécialité
ÉNERGÉTIQUE ET PROCÉDÉS

COMPOSITION DU JURY :

M. Eckhard GROLL
Purdue University,
Rapporteur

M. Jocelyn BONJOUR
INSA de Lyon,
Rapporteur

M. Vincent LEMORT
University of Liège,
Examinateur, Président du jury

M. Dominique MARCHIO
PSL Mines ParisTech,
Examinateur

M. Philippe RIVIERE
PSL Mines ParisTech,
Examinateur

Mme. Odile CAURET
EDF R&D,
Examinateur

Soutenue par
Maria **NIZNIK**
le 10 juillet 2017

Dirigée par **Dominique MARCHIO**

ACKNOWLEDGEMENTS

This PhD was done as a partnership between PSL Mines ParisTech, Centre for Energy efficiency of Systems, and EDF R&D, Energy in Buildings and Territories Department.

I would like to thank my academic supervisors and mentors, Professor Dominique Marchio and Associate Professor Philippe Rivière, for sharing their abundant knowledge in the heat transfer domain, for their dedication, guidance, valuable feedback, and advice.

I would like to express my overwhelming gratitude to my supervisor in EDF R&D, Cedric Teuillières. His extensive experience and vast knowledge on the topic helped me greatly throughout these three years. And most importantly, it is his irreplaceable support and encouragement that gave me strength and endurance to pursue my goals.

These acknowledgements would not be complete without mentioning the input of Odile Cauret; her guidance and interest in this PhD. In addition, a big thank you to the team of Climatron laboratory of EDF R&D for their precious help and technical support.

I owe my deepest gratitude to our group leader, Emmanuel Chabut, for his time, despite his busy schedule, understanding, and constant encouragement. I am very grateful that I had the opportunity to work in such positive work environment.

I wish to thank Professors Eckhard Groll and Jocelyn Bonjour for taking interest in my research and for their willingness to be reviewers of this thesis. Also, I would like to thank Professor Vincent Lemort for agreeing to participate in the jury board. I am honored to have such prominent jury members.

I would also like to thank Mitsubishi Heavy Industries, particularly Yoshiyuki Kimata and Kiyoshi Watanabe, for providing us with valuable experimental data.

I am very grateful to my dear family for your unconditional love, for your support, for your patience, and most importantly for having faith in me. I would not be here without Raphael; without your participation, support, and encouragement

Maria Niznik (Goossens)

To my daughter – to my love

NOMENCLATURE

Symbols

A	*area*	*(m^2)*
C_g	*oil mass fraction*	*(-)*
c_p	*specific heat capacity*	*(J kg^{-1} °C^{-1})*
D	*diameter*	*(m)*
g	*gravitational acceleration*	*(m s^{-2})*
h	*heat transfer coefficient*	*(W m^{-2} °C^{-1})*
h	*specific enthalpy*	*(J kg^{-1})*
k	*thermal conductivity*	*(W m^{-1} °C^{-1})*
L	*length*	*(m)*
$\dot{m}$	*mass flow rate*	*(kg s^{-1})*
Nu	*Nusselt number*	*(-)*
P	*pressure*	*(kPa)*
p	*perimeter*	*(m)*
Pr	*Prandtl*	*(-)*
$\dot{Q}$	*heating power*	*(W)*
R_{HF}	*heat flux ratio*	*(-)*
Ra	*Rayleigh number*	*(-)*
Re	*Reynolds number*	*(-)*
S	*sensitivity index*	*(-)*
T	*temperature*	*(°C)*
t	*time*	*(s)*
$\dot{V}$	*volume flow rate*	*(m^3 s^{-1})*
v	*velocity*	*(m s^{-1})*
$\dot{W}$	*power consumption*	*(W)*
X	*measured variable*	*(-)*
x	*characteristic length*	*(m)*
Y	*calculated variable*	*(-)*
α	*thermal diffusivity*	*(m^2 s^{-1})*
β	*thermal expansion coefficient*	*(K^{-1})*
σ	*standard deviation*	*(-)*
σ	*Stefan-Boltzmann constant*	*(W m^{-2} K^{-4})*
ν	*kinematic viscosity*	*(m^2 s^{-1})*
ρ	*density*	*(kg m^{-3})*
Ω	*angular velocity*	*(rad s^{-1})*

Subscripts

amb	*ambient*
atm	*atmospheric*
ca	*condenser air*
cha-cyl	*compression chamber lateral walls (internal)*
cha-bot	*compression chamber bottom plate (internal)*
cha-top	*compression chamber top plate (internal)*
comp	*component*
comp	*compressor*
comp-cham	*compression chamber*
cond	*condenser*
dis	*discharge*
e	*electric*
ea	*evaporator air*
eff	*effective*
evap	*evaporator*
in	*inlet*
is	*isentropic*
non-is	*non-isentropic*
o	*oil*
out	*outlet*
r	*refrigerant*
ref	*reference*
s	*surface*
sc	*subcooling*
sh	*superheat*
suc	*suction*
w	*water*

Abbreviations

AC	*air conditioner*
CFD	*computational fluid dynamics*
COP	*coefficient of performance*
CO_2	*carbon dioxide*
DHW	*domestic hot water*
EEV	*electronic expansion valve*
EU	*European Union*

FDD	*fault detection and diagnostic*
FDM	*finite difference method*
FEM	*finite element method*
FT	*flash tank*
FVM	*finite volume method*
FXO	*fixed orifice expansion valve*
GHG	*greenhouse gas*
HP	*heat pump*
HP	*high pressure*
IHX	*internal heat exchnager*
LP	*low pressure*
OC	*oil concentration*
PDE	*partial differential equation*
RMS	*root-mean-square*
R134a	*refrigerant type*
R407C	*refrigerant type*
TNW	*thermal network*
TXV	*thermostatic expansion valve*
2D	*two-dimensional*
3D	*three-dimensional*

TABLE OF CONTENTS

INTRODUCTION 1

CHAPTER 1 BACKGROUND AND LITERATURE REVIEW 7

1.1 Overview of heat pumps 8
1.2 Performance assessment method using indirect measurement of refrigerant mass flow rate 15
1.2.1 Compressor energy balance 15
1.2.2 Influence of compressor heat losses 19
1.3 Fault detection and diagnostic using mass flow rate measurements 21
1.3.1 Main faults in the heat pump unit 21
1.3.2 Fault detection and diagnostic method 24
1.4 Conclusions 26

CHAPTER 2 COMPRESSOR HEAT TRANSFER MODEL 29

2.1 State-of-the-art of compressor heat transfer 30
2.1.1 Correlations based on experimental measurements 30
2.1.2 Numerical models 32
2.2 Numerical model of compressor heat transfer 35
2.2.1 Modelling approach 35
2.2.2 Scroll 38
2.2.3 Rotary 54
2.3 Conclusions 60

CHAPTER 3 EXPERIMENTAL VALIDATION OF THE NUMERICAL MODEL 63

3.1 Experimental setup 64
3.2 Comparison of thermal profiles 66
3.2.1 Scroll 67
3.2.2 Rotary 72
3.3 Discussion 75
3.3.1 Simplifications 77
3.3.2 Model applicability to different compressor dimensions and component layouts 80
3.4 Future development 81
3.5 Conclusions 82

CHAPTER 4 IMPROVED IN SITU EVALUATION METHOD OF COMPRESSOR HEAT LOSSES FOR PERFORMANCE ASSESSMENT 83

4.1 Introduction 84
4.2 Existing methods of compressor heat loss modelling 84

4.3 Improved calculation method of compressor heat losses 86
4.3.1 Nusselt number correlations for convective heat transfer coefficients 86
4.3.2 Optimal on-field instrumentation for T_{shell} 88
4.3.3 Heat loss expression for compressors 91
4.4 Conclusions 92

CHAPTER 5 EXPERIMENTAL VALIDATION OF THE PERFORMANCE ASSESSMENT METHOD 93

5.1 Introduction 94
5.2 Heat pump prototype 94
5.3 Experimental setup 96
5.4 Comparison of proposed performance assessment method with reference method 102
5.4.1 Reference heating capacities 103
5.4.2 Additional factors influencing the results of the method 103
5.4.3 Comparison with other heat loss values 104
5.4.4 Operating conditions 104
5.5 Uncertainty values analysis 105
5.6 Results of on-field performance assessment method 107
5.7 Conclusions 115

CONCLUSIONS AND PERSPECTIVES 119

BIBLIOGRAPHY 124

APPENDIX A EXTENSION OF THE PERFORMANCE ASSESSMENT METHOD TO A FDD METHOD 130

A.1 Fault detection and diagnostic methods 131
A.2 Promising fault detection and diagnostic method 132
A.3 Conclusions 137

APPENDIX B EXPERIMENTAL TECHNIQUES FOR COMPRESSOR THERMAL ANALYSIS 138

APPENDIX C ADDITIONAL NUSSELT NUMBER CORRELATIONS 142

C.1 Nusselt number correlation for the stator-rotor gap 143
C.2 Nusselt number correlation for the stator-shell gap 144

LIST OF FIGURES

Figure 1.1 Schematic (a) and P-h diagram (b) of a HP refrigeration cycle *9*
Figure 1.2 Reversible heat pump in heating (a) and cooling (b) mode (COSTIC, 2004) *10*
Figure 1.3 Working principle of a scroll compressor (Hitachi Industrial Equipment Systems, 2017) *11*
Figure 1.4 Working principle of a rotary compressor (Lee, Shim, & Kim, 2016) *12*
Figure 1.5 Refrigeration cycle P-h diagram (a) and schematic with required measurements (b) of basic cycles *16*
Figure 1.6. Refrigeration cycle P-h diagram (a) and schematic with required measurements (b) of FT injection cycle *18*
Figure 1.7. Refrigeration cycle P-h diagram (a) and schematic with required measurements (b) of IHX injection cycles *19*
Figure 2.1. Example of heat flux sensors used to measure compressor heat fluxes in the work of Dutra & Deschamps (2013) *31*
Figure 2.2. Illustration of a hybrid model approach when modeling heat transfer of stator *34*
Figure 2.3. Schematic of the three calculation steps of the model *36*
Figure 2.4. Computational domains of scroll (a) and rotary (b) compressors *37*
Figure 2.5. Thermodynamic refrigeration cycle of a heat pump with associated power distributions inside the compressor *39*
Figure 2.6. Computational domain of scroll compressor in ANSYS Workbench pre-processing tool, Design Modeler *43*
Figure 2.7. Structured (on the left) and unstructured (on the right) grids *44*
Figure 2.8. Scroll compressor mesh in ANSYS Workbench pre-processin tool, Mechanical *45*
Figure 2.9. Equilateral and highly skewed triangle *46*
Figure 2.10. Thin layer of oil in solid phase between refrigerant and oil sump in liquid state *48*
Figure 2.11. Required heat to reach T_{dis} (temperature of the compressed fluid at discharge) *48*
Figure 2.12. Heat fluxes released from the fluid to compression chamber *51*
Figure 2.13. Flow inside the compression chamber (above) is approximated as the flow inside a pipe (below) *53*
Figure 2.14. Computational domian of rotary compressor in ANSYS Workbench pre-processing tool, Design Modeler *56*
Figure 2.15. Insulation layer high-lighted in green around the exterior shell of the compressor *57*
Figure 2.16. Rotary compressor mesh in ANSYS Workbench pre-processing tool, Mechanical *58*

Figure 3.1. Calorimeter chamber of the scroll and rotary compressor test bench used for experimental validation *64*
Figure 3.2. Location of thermocouples on compressor shells of scroll (a) and rotary (b) compressors *66*
Figure 3.3. Experimental and numerical shell temperature distributions in scroll compressor at $\mathrm{Tcond} = 40\ °\mathrm{C}$, $\mathrm{Tevap} = 0\ °\mathrm{C}$, *and* $\mathrm{Tamb} = 10\ °\mathrm{C}$, *30 rps (operating condition 1)* *68*
Figure 3.4. Experimental and numerical shell temperature distributions in scroll compressor at $\mathrm{Tcond} = 40\ °\mathrm{C}$, $\mathrm{Tevap} = 0\ °\mathrm{C}$, *and* $\mathrm{Tamb} = 10\ °\mathrm{C}$, *60 rps (operating condition 2)* *68*
Figure 3.5. Experimental and numerical shell temperature distributions in scroll compressor at $\mathrm{Tcond} = 60\ \mathrm{C}$, $\mathrm{Tevap} = 0\ \mathrm{C}$, *and* $\mathrm{Tamb} = 10$, *30 rps (operating condition 3)* *69*
Figure 3.6. Experimental and numerical shell temperature distributions in scroll compressor at $\mathrm{Tcond} = 40\ °\mathrm{C}$, $\mathrm{Tevap} = 15\ °\mathrm{C}$, *and* $\mathrm{Tamb} = 25\ °\mathrm{C}$, *30 rps (operating condition 4)* *69*
Figure 3.7. Experimental and numerical shell temperature distributions in scroll compressor at $\mathrm{Tcond} = 40\ °\mathrm{C}$, $\mathrm{Tevap} = 15\ °\mathrm{C}$, *and* $\mathrm{Tamb} = 25\ °\mathrm{C}$, *90 rps (operating condition 5)* *70*
Figure 3.8. Experimental and numerical component temperatures in scroll compressor at $\mathrm{Tcond} = 40\ °\mathrm{C}$, $\mathrm{Tevap} = 0\ °\mathrm{C}$, *and* $\mathrm{Tamb} = 10\ °\mathrm{C}$, *30 rps (operating condition 1)* *71*
Figure 3.9. Experimental and numerical component temperatures in scroll compressor at $\mathrm{Tcond} = 40\ °\mathrm{C}$, $\mathrm{Tevap} = 15\ °\mathrm{C}$, *and* $\mathrm{Tamb} = 25\ °\mathrm{C}$, *30 rps (operating condition 4)* *71*
Figure 3.10. Experimental and numerical component temperatures in scroll compressor at $\mathrm{Tcond} = 40\ °\mathrm{C}$, $\mathrm{Tevap} = 15\ °\mathrm{C}$, *and* $\mathrm{Tamb} = 25\ °\mathrm{C}$, *90 rps (operating condition 5)* *72*
Figure 3.11. Experimental and numerical shell temperature distributions in rotary compressor at $\mathrm{Tcond} = 40\ °\mathrm{C}$, $\mathrm{Tevap} = 0\ °\mathrm{C}$, *and* $\mathrm{Tamb} = 10\ °\mathrm{C}$, *30 rps (operating condition 1)* *73*
Figure 3.12. Experimental and numerical shell temperature distributions in rotary compressor at $\mathrm{Tcond} = 40\ °\mathrm{C}$, $\mathrm{Tevap} = 0\ °\mathrm{C}$, *and* $\mathrm{Tamb} = 10\ °\mathrm{C}$, *60 rps (operating condition 2)* *73*
Figure 3.13. Experimental and numerical shell temperature distributions in rotary compressor at $\mathrm{Tcond} = 60\ ^{\circ}\ \mathrm{C}$, $\mathrm{Tevap} = 0\ ^{\circ}\ \mathrm{C}$, *and* $\mathrm{Tamb} = 10\ ^{\circ}\ \mathrm{C}$, *30 rps (operating condition 3)* *74*
Figure 3.14. Experimental and numerical shell temperature distributions in rotary compressor at $\mathrm{Tcond} = 40\ ^{\circ}\ \mathrm{C}$, $\mathrm{Tevap} = 15\ ^{\circ}\ \mathrm{C}$, *and* $\mathrm{Tamb} = 25\ ^{\circ}\ \mathrm{C}$, *30 rps (operating condition 4)* *74*

Figure 3.15. Experimental and numerical shell temperature distribution in rotary compressor at Tcond = 40 °C, Tevap = 15 °C, *and* Tamb = 25 °C, *90 rps (operating condition 5)* *75*
Figure 3.16. Temperature contours of rotary compressor shell in absolute temperature (K) *76*
Figure 3.17. Temperature contours of scroll compressor shell in absolute temperature (K) *77*
Figure 3.18. Thin oil film forming an interface betwee the refirgerant gas and a solid component *78*
Figure 3.19. Different inlet locations in scroll compressor and their effect on the refrigerant flow paths *80*
Figure 4.1. Location of temperature sensors required to evaluate heat losses of rotary (on the left) and scroll (on the right) compressors *91*
Figure 5.1. Exterior unit with a compressor and EEV separated by a metallic sheet from the evaporator and fan *95*
Figure 5.2. Exterior unit from the side of the evaporator *95*
Figure 5.3 Exterior unit from the side of the fan *96*
Figure 5.4. Exterior unit located in the climatic chamber 2 (outdoor chamber) *97*
Figure 5.5. Indoor unit with condenser coupled to a water loop (on the left) and contorl unit of water inlet temperature located in room number 3 (on the right) *97*
Figure 5.6. Air-to-water HP prototype and required instrumentation installed in three climatic chambers *98*
Figure 5.7. Locations of sensors used to measure the temperature of air surrounding the compressor *100*
Figure 5.8. Thermometer (PT100) used to measure the evaporator inlet air, i.e. T_{ext} *101*
Figure 5.9. Refrigeration cycle P-h diagram (a) and a schematic with required measurements (b) for the experimental validation of the performance assessment method *102*
Figure 5.10. Root mean square errors of the estimated heating capacities when Qamb *is obtained using different air temperature sensors* *107*
Figure 5.11. Deviations of heating capacities from reference values when Qamb *is obtained using different air temperature sensors* *108*
Figure 5.12. Deviations of heating capacities calculated using the previosuly defined Qamb *evaluation method and the more accurate method from the reference values as a function of compressor speeds* *109*
Figure 5.13. Comparison of heating capacities deviations from the reference values with different Cg *values* *110*
Figure 5.14. Required instrumentation to measure rotary compressor heat losses on-field *111*

Figure 5.15. Reference and calculated heating capacities at different operating conditions *111*
Figure 5.16. Compressor heat losses calculated from the new heat loss evaluation method, Eq. (5.1), old heat loss evaluation method, Eq. (1.19) and reference values Eq. (5.8) in tested operating conditions *112*
Figure 5.17. Deviations in heating capacities from reference values as a function of compressor speed *113*
Figure 5.18. Deviations in heating capacities from reference values as a function of compressor power input *114*
Figure 5.19. Deviations in heating capacities from reference values as a function of evaporation temperature *114*
Figure 5.20. Deviations in heating capacities from reference values as a function of temperature difference between compressor shell and ambient temperatures *115*
Figure A.1. Flow chart diagram of condenser fouling detection algorithm *134*
Figure A.2. Flow chart diagram of evaporator fouling detection algorithm *135*

LIST OF TABLES

Table 1.1 Most common faults occurring in the HP unit *23*
Table 3.1 Operating conditions used to obtain experimental results for numerical model validation *67*
Table 3.2 Dimensionless RMS errors of external profiles in different operating conditions in scroll compressor *70*
Table 3.3 Dimensionless RMS errors of external profiles in different operating conditions in rotary compressor *75*
Table 4.1. The RMS errors of temperature values measured from different temperature sensors from the area-weighted average temperatures of the rotary compressor shell *85*
Table 4.2. Shell heat flux ratio of scroll compressor extracted from Fluent in different operating conditions *89*
Table 5.1. Location of ambient temperature sensors *100*
Table 5.2. Operating conditions tested in the experimental test bench *105*
Table 5.3. Sensors used in measurements and their respective uncertainties *105*
Table 5.4 Sensitivity index of each variable in the final uncertainty of the calculated heating power in operating condition 6 ..... *113*
Table 5.5. Optimal instrumentation used to determine T_{shell} *in scroll and rotary compressors* *117*
Table A.1. Fault decoupling features, required temperature measurements, and virtual measurements *137*
Table B.2 Measurement techniques used to determine compressor thermal behavior *140*

INTRODUCTION

Le développement des pompes à chaleur (PAC), qui offrent des efficacités énergétiques élevées, est essentiel pour réduire la consommation d'énergie dans les bâtiments et répondre aux enjeux énergétiques et environnementaux à l'échelle nationale ou européenne. Cependant, les performances réelles des PAC sont difficiles à évaluer sur site. Une méthode adaptée par Tran *et al.* (2013) permet de mesurer leurs performances sur le terrain mais sa précision reste fortement dépendante de l'évaluation des pertes thermiques du compresseur.

L'objectif de cette thèse est d'améliorer cette méthode de mesure en identifiant et validant une approche simplifiée d'évaluation sur site des pertes thermiques du compresseur.

La méthode de mesure des performances est détaillée dans le chapitre 1. Deux modèles numériques de comportement thermique de compresseurs (scroll et rotary) sont exposés dans le chapitre 2. Après leur validation expérimentale (chapitre 3), les modèles sont utilisés dans le chapitre 4 pour déterminer l'approche à adopter pour pouvoir évaluer précisément les pertes thermiques sur site. Cette approche est ensuite intégrée dans la méthode de mesure des performances réelles et validée en laboratoire sur un prototype de pompe à chaleur air-eau dans le chapitre 5.

Research objective

The three key targets for 2020 of the European Union (EU) climate action is to reduce greenhouse gas (GHG) emissions by 20% when compared with emission levels in 1990, ensure that 20% of total energy consumption is from renewable energy, and a 20% increase in energy efficiency (European Commission, 2017). It has been shown that a major part of the GHG emissions originate from heating and domestic hot water (DHW) consumption. According to French Environment and Energy Management Agency (2014), heating and DHW production was responsible for 25% of total CO_2 emissions and 40% of final energy consumption in France. For these reasons, efficient and environmentally friendly energy solutions for heating and DHW production are in demand. One of these solutions consists of using residential heat pumps (HPs).

Due to high theoretical efficiency of residential HPs, their development is essential when attempting to reduce heating energy consumption in dwellings. However, current methods to evaluate HP efficiencies have become problematic since efficiencies are measured and established in controlled laboratory conditions (Ertesvåg, 2011). Performance values obtained in such conditions may differ from the ones obtained on-field due to several factors, such as installation quality, design of the heating system, and climatic conditions. Therefore, real-time on-field performance measurements provide more reliable data. Nevertheless, measuring accurately on-field heating capacity and coefficient of performance (COP) of HPs is difficult, particularly, of air-to-air HPs, since measuring air enthalpies and specifically air mass flow rate on-field is challenging (McWilliams, 2002).

A performance assessment method, presented and validated in the work of (Tran *et al*., 2013) demonstrates that air-to-air HP efficiencies can be measured using mass/energy balances of the refrigeration components. The measurements necessary for this method, located on the refrigerant side, require only non-intrusive supplementary sensors, surface temperature sensors, in addition to already installed pressure sensors. The method is, therefore, well-adapted for in-situ performance evaluation.

Performance assessment method is based on compressor energy balance, where compressor heat losses towards the ambient air must be estimated. Tran *et al.* (2013) stated that the sensitivity index of heat losses in the relative uncertainty of heating capacity predicted by the method is 40 %. Thus, compressor heat losses must be evaluated more accurately as they influence significantly the overall accuracy of the method.

The method consists of measuring indirectly the refrigerant mass flow rate using the compressor energy balance. The heating capacity is then obtained using this value and by measuring condenser inlet and outlet enthalpies. Finally, the COP value of HP can then be calculated directly as a ratio of heating capacity to the measured HP electrical

power input. An advantage of this on-field performance measurement is to ensure optimal operation of HP systems by promptly detecting significant performance degradation. This diagnosis reflects positively on energy and cost savings. Additionally, refrigerant mass flow rate also provides in itself valuable information in terms of fault detection and diagnostics (FDD). Therefore, integrating an on-field FDD technology is important to minimize performance degradation, maintenance costs, such as field inspections and component replacements, and machine down-time. To sum up, the method provides means for the optimization of HP operation and maintenance quality.

The aim of this thesis is to improve the method presented by Tran *et al.* (2013) by investigating the simplest way to measure precisely compressor heat losses on-field, and then to experimentally validate this fully operational and reliable in-situ assessment method of HP performances. The newly proposed method should be compatible with various refrigeration cycles, such as air-to-air HPs, with and without vapor injection, and easily applicable in already-installed machines.

Research objectives stated above are achieved in three steps:

- First, a more accurate method to evaluate compressor heat losses on-field will be established in order to minimize the influence of compressor heat losses on the uncertainty of the performance assessment method. For this purpose, a numerical model that simulates compressor thermal behavior is developed. The model couples integral and differential formulations. Exterior thermal profiles of scroll and rotary compressor shells are validated with experimental data obtained for both compressor types in Mitsubishi Heavy Industries (MHI) laboratory.
- The simulation model is then used to observe the thermal behavior of compressor shells and to determine the minimum non-intrusive instrumentation, *i.e.* the minimal number of surface temperature sensors and their locations on the rotary and scroll compressor shells, necessary to estimate compressor heat losses on-field. Also, the required correlations in order to evaluate convective heat transfer coefficients used to calculate compressor heat losses on-field are selected. The methodology to measure scroll and rotary compressor heat losses on-field is established and integrated in the performance assessment method.
- The improved method is then experimentally validated in EDF R&D Lab Renardières, France, using an air-to-water HP prototype in several operating conditions.

Thesis overview

Chapter 1 first presents a brief overview of the thermodynamic cycle that constitutes a HP system: compression, condensation, expansion, and evaporation. In this chapter, state-of-the-art performance measurement methods are presented and their limitations are highlighted.

Chapter 1 also introduces a promising performance measurement method that uses indirect mass flow rate measurement, presented in the work of Tran *et al.* (2013), and the influence of the current compressor heat loss evaluation integrated in the method on the overall result uncertainty. Finally, a FDD method that can potentially be integrated in the proposed performance assessment method is presented.

Chapter 2 illustrates the developed numerical model that simulates heat transfer of scroll and rotary compressors. Two distinct numerical models have been developed for both compressor types due to differences in the internal component layouts, specifically the location of the electrical motor. The model is a hybrid model where a computational fluid dynamics (CFD) analysis is supported and optimized by integral formulations programmed in MATLAB. Simulations are done in steady state conditions. The limitations of the numerical models and suggestions for future development conclude Chapter 2.

Consequently, **Chapter 3** deals with the experimental validation of the developed model using measurement results obtained for both compressor types, scroll and rotary. The experimental test bench for both compressor types is presented. Introduced simplifications, applicability of the model to different internal component layouts and dimensions, and suggestions for future development are discussed. The chapter concludes that the accuracy of the model is sufficient for it to be used to determine the temperature sensor location for measuring on-field compressor heat losses.

Chapter 4 presents the required instrumentation, in terms of temperature sensor locations for scroll and rotary compressors, and the selected heat transfer correlations that can be employed when the shell temperature and the temperature of air surrounding the compressor are known. Thus, Chapter 4 establishes the improved on-field heat loss evaluation method for scroll and rotary compressors.

The performance assessment method with improved heat loss evaluation method is experimentally validated in **Chapter 5** with a specific HP test bench. The air-to-water HP prototype built specifically for the HP test bench along with the experimental test set up is presented. The deviations between the heating capacities obtained from the performance assessment method and reference values are presented and discussed.

Finally, conclusions are drawn on the reliability and applicability of the method in on-field conditions. The possibilities to further exploit the numerical model in order to characterize scroll and rotary compressors of different sizes and to adapt the heat loss evaluation methods accordingly, are explored. It is also proposed to validate the performance assessment method coupled with the chosen FDD method with the experimental test bench presented in Chapter 5.

CHAPTER 1

BACKGROUND AND LITERATURE REVIEW

Pour optimiser la consommation énergétique des PAC, l'évaluation de la puissance thermique et du coefficient de performance sur site en temps réel est importante. Néanmoins, déterminer les performances des PAC reste problématique, notamment dans le cas de PAC air-air, car l'estimation de l'enthalpie et du débit massique de l'air est difficile. Tran *et al.* (2013) a adapté une méthode qui est basée sur les mesures des propriétés de fluide frigorigène et les bilans énergétique/massique afin d'obtenir les performances d'une PAC en temps réel sur site. Cette méthode utilise seulement des capteurs non-intrusifs. Elle est compatible avec différents types de PAC, y compris les PAC air-air, et est adaptée aux cycles plus complexes (cycles à injection).

La méthode intègre l'évaluation de pertes thermiques du compresseur. Tran *et al.* (2013) a déterminé que l'incertitude sur l'évaluation de ces pertes contribue à hauteur de 40% sur l'erreur d'estimation de la puissance thermique. Cela illustre l'importance de développer une approche plus aboutie et plus fiable pour évaluer les pertes thermiques sur site, afin de réduire l'incertitude sur la méthode de mesures des performances. L'approche utilisée à l'origine dans cette méthode reposait sur l'approximation que la température de l'enveloppe du compresseur est homogène et égale à la température du réfrigérant au refoulement. Toutefois, ceci n'est pas toujours le cas, en particulier pour les compresseurs scroll où la chambre de compression est en haut.

La méthode de mesures des performances calcule le débit massique. La connaissance du débit en temps réel est utile dans le modèle de détection et de diagnostic de défauts, présentée dans le travail de Li & Braun (2007). Prochainement, les défauts les plus communs dans les PAC pourraient être testés afin de valider expérimentalement la méthode de détection et de diagnostic de défauts couplée avec la méthode de mesure des performances.

1.1 Overview of heat pumps

Following widespread concern with greenhouse gas emissions, climate change, and increasing energy demand in heating and air-conditioning, the development of residential HPs has been a driving force for diminishing heating energy consumption of dwellings, due to their high theoretical efficiency. Currently, millions of HPs are installed worldwide.

Heat pumps constitute heating units or systems that extract heat from outdoor air, which is then used to heat a building. Vapor-compression refrigeration cycle is the basis of the heat transfer cycle, where a chemical substance, the refrigerant, alternately changes phase from liquid to gas and gas to liquid, as depicted in Figure 1.1. The heat transfer cycle consists of four distinct steps:

1. Compression (1-2):

Refrigerant gas entering at low pressure (LP) and temperature is compressed to a higher pressure (HP), thus elevating the temperature, by consuming electrical power input. In some cases injection of refrigerant fluid at intermediate pressure is installed (see Subsection 1.2.1).

2. Condensation (2-3):

Refrigerant gas at high temperature and pressure releases thermal energy to a medium, such as water or air that serves as a heat sink, undergoing phase change from gas to liquid state.

3. Expansion (3-4):

High-pressure and medium-temperature refrigerant liquid is submitted to an expansion by flowing through an orifice in the expansion valve, thus, reducing liquid pressure and temperature.

4. Evaporation (4-1):

Refrigerant at low temperature and pressure absorbs heat from a medium, such air or water that serve as a heat source, undergoing phase change. Finally, low-temperature and low-pressure refrigerant gas flows to the compressor and the cycle is repeated.

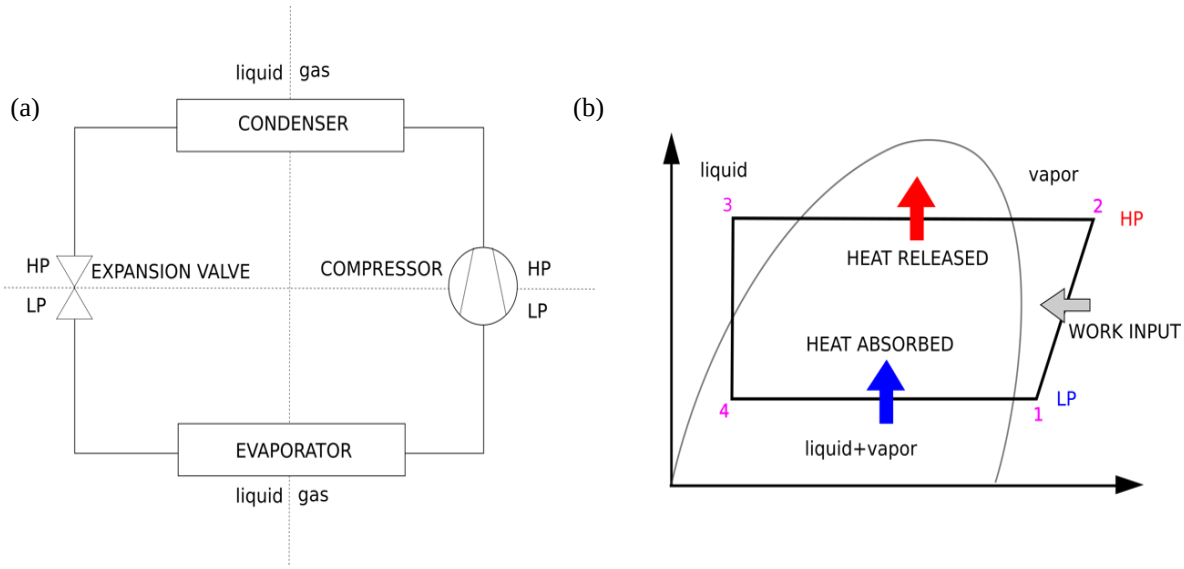

Figure 1.1 *Schematic (a) and P-h diagram (b) of a HP refrigeration cycle*

Reversible heat pumps can reverse the direction of the refrigerant flow between the two heat exchangers, condenser and evaporator, using a reversing valve, as illustrated in Figure 1.2. In such case, the heat pump will operate in a cooling mode, extracting heat from a building and rejecting it to the outdoor air.

Reversible heat pump systems consist of four primary components:

- compressor;
- condenser;
- expansion valve and
- evaporator.

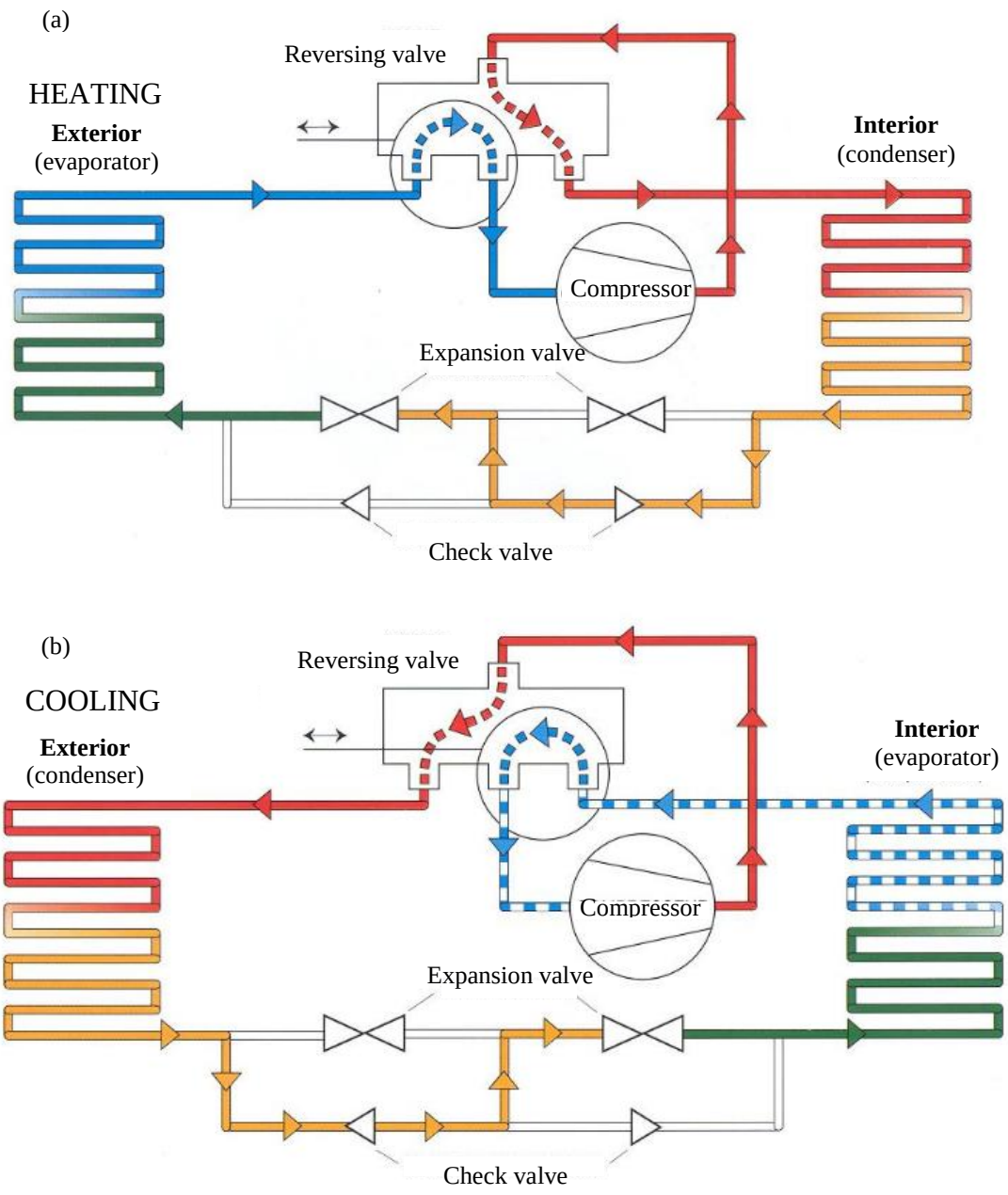

Figure 1.2 *Reversible heat pump in heating (a) and cooling (b) mode (COSTIC, 2004)*

Compressor – The refrigerant entering in a gaseous phase is compressed to a higher pressure. In the process, the refrigerant temperature is also increased. Heat pump compressors require electrical power input. Lubricant oil is used to prevent damage of internal compressor components. In hermetic compressors, the motor and compression chamber are confined in a steel shell. In such compressor types, oil is present in a sump (reservoir) at the bottom of the compressor, and covers the majority of internal components. Droplets of oil are mixed with refrigerant and part of the oil migrates into the refrigeration cycle. For this reason, the working fluid of a HP cycle is a mix of refrigerant and lubricant oil.

Scroll and rotary compressors are the two most commonly employed compressor types in residential air-to-air HPs (Tran, 2012). Both compressors are positive displacement compressor types. Scroll compressors have one scroll, or spiral, orbiting in a path that is defined by a matching fixed scroll, creating gas pockets between the scrolls. The orbiting scroll is attached to the crankshaft and the fixed one is attached to the compressor body. The gas is drawn in from the outer side portion of the scroll, creating a gas pocket that travels in between the scrolls. The gas then moves towards the center of the scrolls (discharge) simultaneously decreasing the pocket size, increasing the pressure and temperature. The working principle of scroll compressors is illustrated in Figure 1.3.

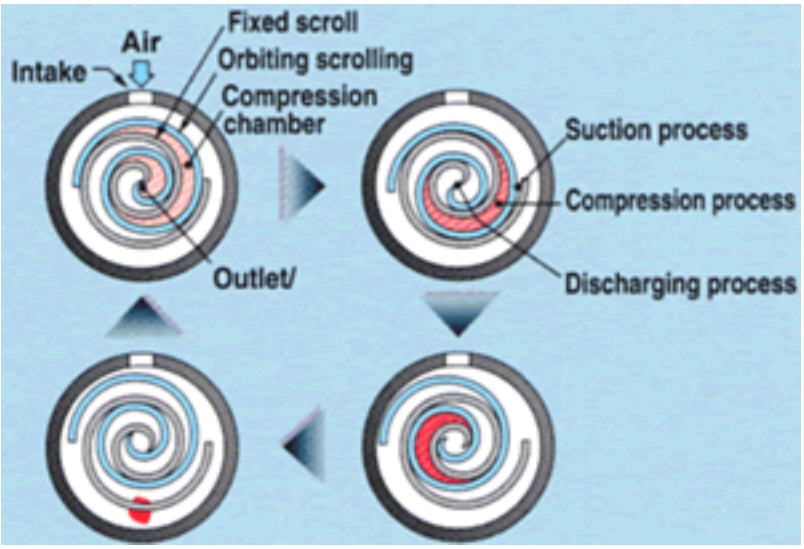

Figure 1.3 *Working principle of a scroll compressor (Hitachi Industrial Equipment Systems, 2017)*

In rotary compressors the rotating shaft sets in rotating motion a roller, named the rotor, inside a cavity. The circular rotor rotates inside a circular cavity eccentrically,

since the centers of the circular cavity and rotor are offset. This compresses the refrigerant gas to a desired pressure, as the volume of the gas decreases. The working principle of a rotary compressor is depicted in Figure 1.4.

Condenser – The heat exchanger condenses refrigerant fluid from gaseous to liquid state, and delivers extracted heat from the heat source (outdoor air) to the heat sink (indoor air). Typically, a condenser consists of copper coils with aluminum fins. A fan is used to pull the ambient air through the finned coils, creating indoor air circulation across the exchanger. At the same time, the refrigerant circulates inside the finned coils.

Expansion valve – The aim of the expansion valve is to decrease the refrigerant pressure. Thermostatic (TXV) or electronic expansion valves (EEV) are, typically, used to adjust the device opening to ensure a certain pressure drop. Generally, the fluid is in a two-phase state when exiting the expansion valve.

Evaporator – Similar to a condenser, an evaporator, typically, consists of copper coils with aluminum fins. The refrigerant in a two-phase state in an evaporator is converted to a gaseous state by extracting thermal energy from a heat source (outdoor air). Generally, the refrigerant exiting the evaporator must be in a completely gaseous state, since liquid droplets can damage the compressor. As in the case of condensers, the air crossing the exchanger coils can also be regulated with a fan.

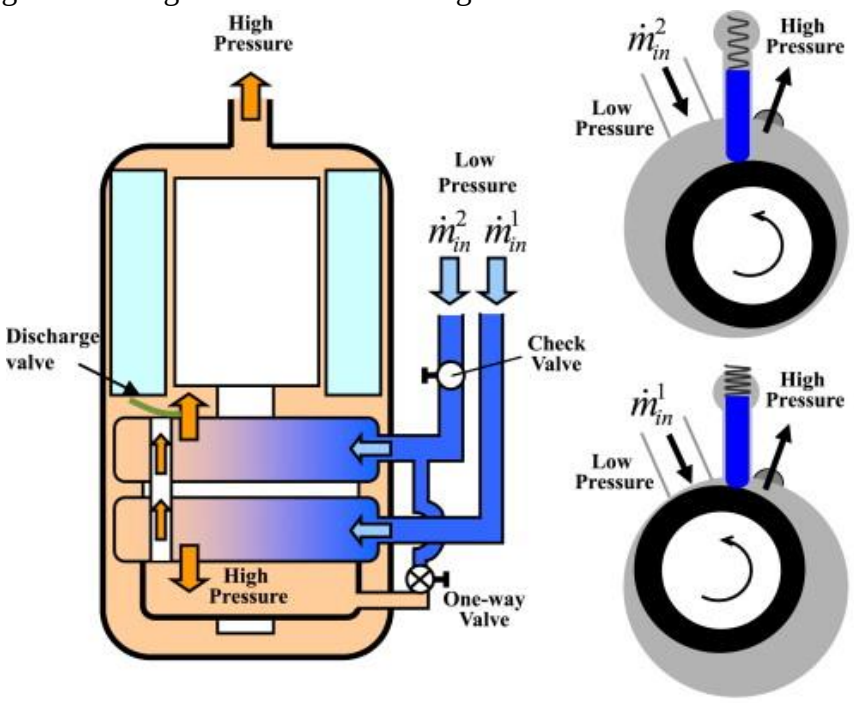

Figure 1.4 *Working principle of a rotary compressor (Lee, Shim, & Kim, 2016)*

The First Law of Thermodynamics postulates the conservation of energy stating that energy cannot be created or destroyed, but can be transformed. Assuming that work and heat are the only forms of energy exchanged between the system and surroundings, the First Law is described in:

$$\dot{m}\Delta h = \dot{Q} + \dot{W} \tag{1.1}$$

The equation above is an energy balance for open systems formulated as an enthalpy balance.

Coefficient of performance (COP_{HP}) is the most common indicator of heat pump efficiency. Coefficient of performance is a dimensionless value defined as a ratio of the net heating capacity, $\dot{Q}_{cond}$, and electrical power input, $\dot{W}_{HP}$, under designated operating conditions, as listed below:

$$COP_{HP} = \frac{\dot{Q}_{cond}}{\dot{W}_{HP}} \tag{1.2}$$

The condensation heat, $\dot{Q}_{cond}$, is determined from the condenser energy balance in steady-state, as follows:

$$\dot{Q}_{cond} = \dot{m}\left(h_{cond,in} - h_{cond,out}\right) \tag{1.3}$$

where $\dot{m}$ is the mass flow rate of the working fluid, h is the working fluid enthalpy, *in* and *out* are condenser inlet and outlet sides, respectively.

As mentioned previously, the working fluid of the HP refrigeration cycle is a refrigerant and oil mixture, and the enthalpy change at the condenser can be calculated as follows:

$$\Delta h_{cond,in\rightarrow out} = \left(1 - C_g\right)\left(h_{r,cond,in} - h_{r,cond,out}\right) + C_g \Delta h_o^{T_{cond,out} - T_{cond,in}} \tag{1.4}$$

where C_g is the mass fraction of oil with respect to the working fluid flow, *in* and *out* are the inlet and outlet sides of the condenser, respectively, and $\Delta h_o^{T_{cond,out} - T_{cond,in}}$ is the specific enthalpy change of oil calculated, as follows:

$$\Delta h_o^{T_{cond,out} - T_{cond,in}} = c_{p,o}\left(T_{cond,in} - T_{cond,out}\right) \tag{1.5}$$

where $c_{p,o}(T)$ is the specific heat capacity of oil calculated as in Conde (1996) and Liley and Gambill (1973):

$$\rho_o(T) = \rho_o(T_0) - 0.6(T - T_0) \quad (1.6)$$

$$c_{p,o}(T) = \frac{1684 + 3.4T}{\sqrt{s}} \quad (1.7)$$

where s is the ratio of oil density to water density at 15.56 °C, where T is the temperature in °C, $\rho_o(T_0)$ is the oil density at $T_0 = 38$ °C, typically, provided by the manufacturer.

Finally, the condensation heat is obtained, as follows:

$$\dot{Q}_{cond} = \dot{m}\left[\left(1 - C_g\right)\left(h_{r,cond,in} - h_{r,cond,out}\right) + C_g \Delta h_o^{T_{cond,out} - T_{cond,in}}\right] \quad (1.8)$$

Heat pumps can operate at lower efficiencies that the ones measured and established by manufacturers. Heat pump manufacturers provide COP values obtained in laboratories under standardized controlled operating conditions specified in EN14511 and ISO5151. These COP values are not necessarily representative of those obtained on-field due to several factors, such as installation quality, system design, climatic conditions, and faults occurring in the system.

Performances can be easily estimated on-field in water-to-water and air-to-water HPs by measuring the thermal energy supplied to the water circuit, which is calculated from the water inlet and outlet temperature, and mass flow rate measurements. It is particularly challenging to accurately measure the performances of air-to-air heat pumps (HPs) on-field, since obtaining accurate air enthalpy and flow rate measurements is problematic (McWilliams, 2002).

An anemometer can be used to measure the air flow directly in order to estimate the performances of air-to-air HPs on-field. However, the implementation of such measurement installation on-field is difficult. For instance, it can interfere with the HP operation, due to affected air flow rate that resulted from additional pressure losses. Ichikawa *et al.* (2007) presented another method, where the heating energy is obtained from the air velocity field, temperatures and humidity ratios. This method requires data from the manufacturer, which makes it non-generic and unsuitable for measurements over long periods of time.

Both of the mentioned methods can be classified as external methods since the measurements are based on air properties. Internal methods, on the other hand, require refrigerant fluid measurements. The refrigerant enthalpy is computed from temperature and pressure measurements. Mass flow rate can be obtained using a flow meter or component energy/mass balances, as in the work of Teodorese *et al.*, (2007) and

(Fahlén, 2004). The main drawback of these methods is the requirement of using intrusive flow meter and/or pressure sensors. The importance of using nonintrusive sensors to obtain accurate performance data must be stressed since intrusive sensors cause weak perturbations in the refrigerant flow in functioning machines affecting the performance of the refrigeration cycles. Furthermore, the application of intrusive measurements is expensive, difficult in already-installed machines, and can provoke potential leak sources.

Based on the work of Fahlén (2004), an internal method is presented in the work of Tran, *et al.* (2012). The method constitutes a promising on-field performance assessment method that is based on refrigerant fluid measurements and component energy/mass balances. The method does not require intrusive flow and pressure meters, and is, therefore, perfectly suitable for on-field measurements. In fact, only non-intrusive surface temperature sensors are employed to estimate required pressures, refrigerant mass flow rate, heating capacities, and COP values. The method can be applied in different types of heat pump systems, including air-to-air and more complex refrigeration cycles. The method is described in more detail in Section 1.2.

1.2 Performance assessment method using indirect measurement of refrigerant mass flow rate

As stated previously, the performance assessment method determines indirectly the refrigerant mass flow rate using only non-intrusive sensors. It comprises basic and complex cycles, such as vapor injection cycles. The aim of the method is to determine the performances of HPs in terms of heating capacity and COP.

1.2.1 Compressor energy balance

<u>Basic cycles</u>

In basic refrigeration cycle, shown in the P-h diagram (a) and system schematic with all measurements required (b) in Figure 1.5, the method utilizes solely a steady-state compressor energy balance, as depicted below:

$$\dot{W}_{comp} = \dot{m}\left[\left(1 - C_g\right)\left(h_{r,comp,out} - h_{r,comp,in}\right) + C_g \Delta h_o^{T_{comp,out} - T_{comp,in}}\right] + \dot{Q}_{amb} \tag{1.9}$$

where $\dot{W}_{comp}$ is compressor power input measured with a wattmeter, and $\dot{Q}_{amb}$ is the heat transfer from compressor shell to the ambient air, *i.e.* compressor heat losses,

discussed in more detail in Subsection 1.2.2, and $C_g \Delta h_o^{T_{comp,in} \rightarrow T_{comp,out}}$ is the oil enthalpy change in the compressor.

The refrigerant mass flow rate is determined as follows:

$$\dot{m} = \frac{\dot{W}_{comp} - \dot{Q}_{amb}}{(1 - C_g)(h_{r,comp,out} - h_{r,comp,in})} + C_g \Delta h_o^{T_{comp,in} \rightarrow T_{comp,out}} \qquad (1.10)$$

In order to determine refrigerant enthalpy at a certain point, fluid temperature and pressure must be known. Fluid temperatures are obtained directly from pipe surface measurements. High and low pressures are determined indirectly via non-intrusive saturation temperature measurements on condenser and evaporator heat exchangers. Evaporation pressure is determined by placing a surface temperature sensor at the inlet of the evaporator (point 4 in Figure 1.5), where the fluid is definitely in a two-phase state. Similarly, for the condensation pressure, the saturation temperature is measured in the center of the condenser (point 2' in Figure 1.5), after desuperheating and before subcooling of the fluid. If the fluid is zeotropic, the temperature glide during phase change introduces an error in the calculated pressure. Yet, the influence of the error is limited; for example, in the case of refrigerant R407C, which is a strongly zeotropic fluid with a temperature glide of approximately 6 K, the error is 0.2 bar at most (Tran, 2012).

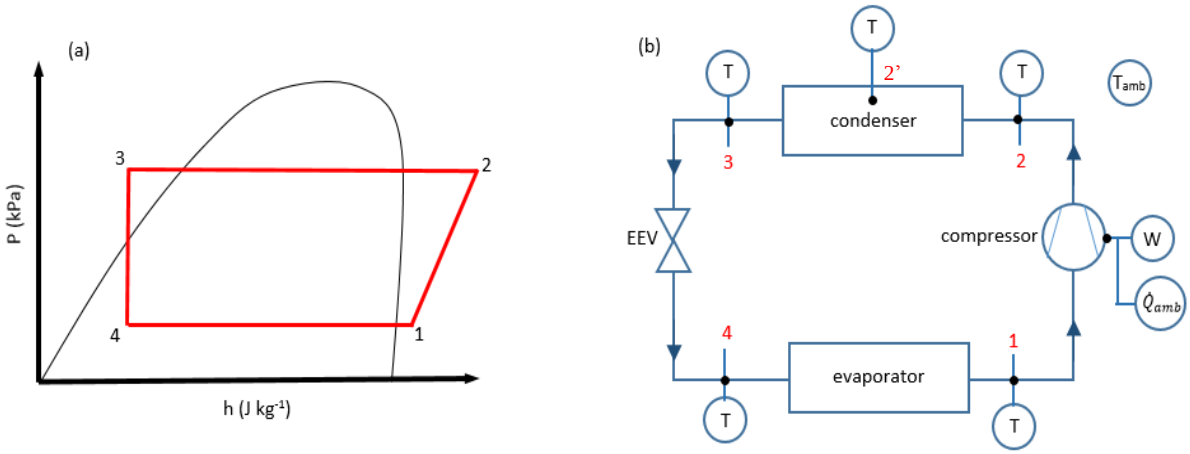

Figure 1.5 *Refrigeration cycle P-h diagram (a) and schematic with required measurements (b) of basic cycles*

<u>Extension to cycles with injection</u>

The efficiency of basic refrigeration cycles has been shown to degrade, when air-source HPs operate at very low and high ambient temperatures, due to increased compressor heat losses and reduced mass flow rate, respectively. Vapor injection cycles

have been proposed by several HP manufacturers as alternatives to basic cycles, in order to increase both performance and heating capacity at these extreme conditions Heo *et al.* (2011). Singer *et al.* (2014), showed that theoretically performance assessment method can be extended to injection cycles. This can be achieved by determining steady-state equation systems to resolve mass flow rates. These equations are based on the component mass/energy balances.

Injection HP cycles can be classified in two main categories: cycles that include a flash tank (FT) and cycles that include an internal heat exchanger (IHX). Various combinations and arrangements of these components and expansion valves can form novel injection refrigerant cycles. However, the main principle of injection cycles is that the refrigerant flow is separated after exiting the condenser and the bypass flow passes through the mentioned components in order to be injected into the multistage compressor unit (Singer *et al.*, 2014).

Flash Tank HP (FT) – In such cycles working fluid exiting the condenser in a liquid state passes by an expansion valve. After which, flash tank separates the fluid in vapor state from the fluid in liquid state. The former is injected in the compressor serving as a cooling agent, and the latter continues further expansion before entering the evaporator in order to complete the cycle. Such maneuver allows lower compressor discharge temperatures, thus, improving the COP and heating capacity. The P-h diagram and flow schematic are depicted in Figure 1.6. Steady-state equation system is used to calculate the mass flow rates. The system of equations consists of compressor mass balance, Eq. (**1.11**), FT energy balance, Eq. (**1.12**), and compressor energy balance, Eq. (**(1.13**):

$$\dot{m}_1 + \dot{m}_9 = \dot{m}_4 \tag{1.11}$$

$$\dot{m}_4 h_6 = \dot{m}_9 h_9 + \dot{m}_1 h_7 \tag{1.12}$$

$$\dot{W}_{comp} = \dot{Q}_{amb} + \dot{m}_4 h_4 - \dot{m}_9 h_9 - \dot{m}_1 h_1 \tag{1.13}$$

where h is the specific enthalpy of working fluid (refrigerant and oil), calculated as follows:

$$h = \left(1 - C_g\right) h_r + C_g h_o \tag{1.14}$$

From the three-equation system mass flow rates are resolved, and $\dot{m}_4$ is used to calculate the condensation heat (heating mode):

$$\dot{Q}_{cond} = \dot{m}_4 \left[(1 - C_g)(h_{r,cond,in} - h_{r,cond,out}) + C_g \Delta h_o^{T_{cond,out} \to T_{cond,in}} \right] \qquad (1.15)$$

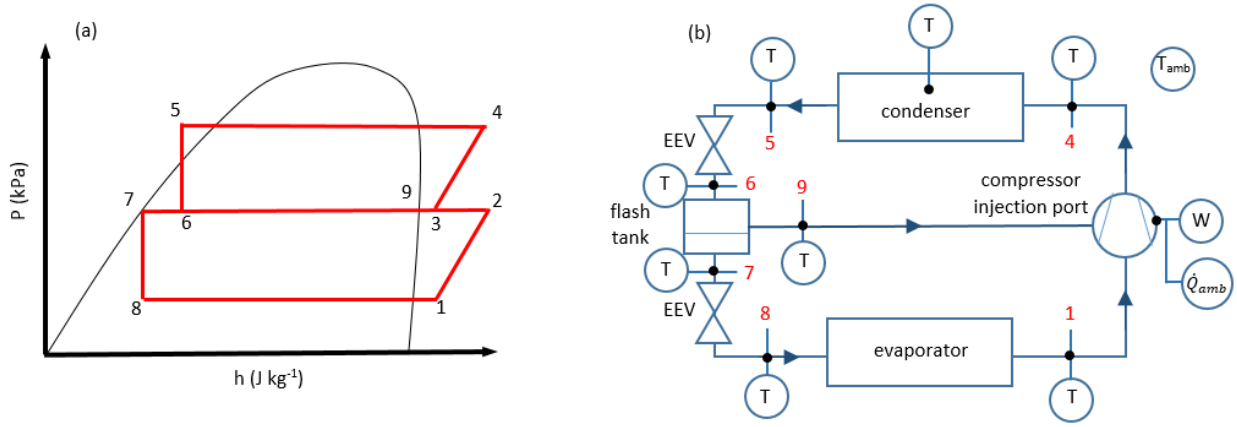

Figure 1.6. *Refrigeration cycle P-h diagram (a) and schematic with required measurements (b) of FT injection cycle*

Internal Heat Exchanger HP (IHX) – Internal heat exchanger (IHX) refrigeration cycle is one of the principle vapor injection cycles (Singer *et al.*, 2014). In such cycles the working fluid is divided in two streams after exiting the condenser and a lesser amount is expanded to a two-phase state. The injected fluid is in vaporized state due to a heat exchange that occurs between the subcooled and two-phase working fluids. The P-h diagram and flow schematic are illustrated in Figure 1.7. One of the main advantages of the IHX system is that injection of the cooled refrigerant vapor allows the working fluid to be compressed to a desired pressure while consuming less electrical energy than a compressor in a simple cycle would under the same operating conditions. The steady-state three-equation system consists of compressor mass balance, Eq. (**1.16**), IHX energy balance, Eq. (**1.17**), and compressor energy balance, Eq. (**1.18**):

$$\dot{m}_1 + \dot{m}_9 = \dot{m}_4 \qquad (1.16)$$

$$\dot{m}_1 (h_5 - h_6) = \dot{m}_9 (h_9 - h_8) \qquad (1.17)$$

$$\dot{W}_{comp} = \dot{Q}_{amb} + \dot{m}_4 h_4 - \dot{m}_9 h_9 - \dot{m}_1 h_1 \qquad (1.18)$$

Similar to the case of FT vapor injection system, thermal capacity is calculated from Eq. (**1.15**) utilizing the total mass flow rate, $\dot{m}_4$, passing through the condenser.

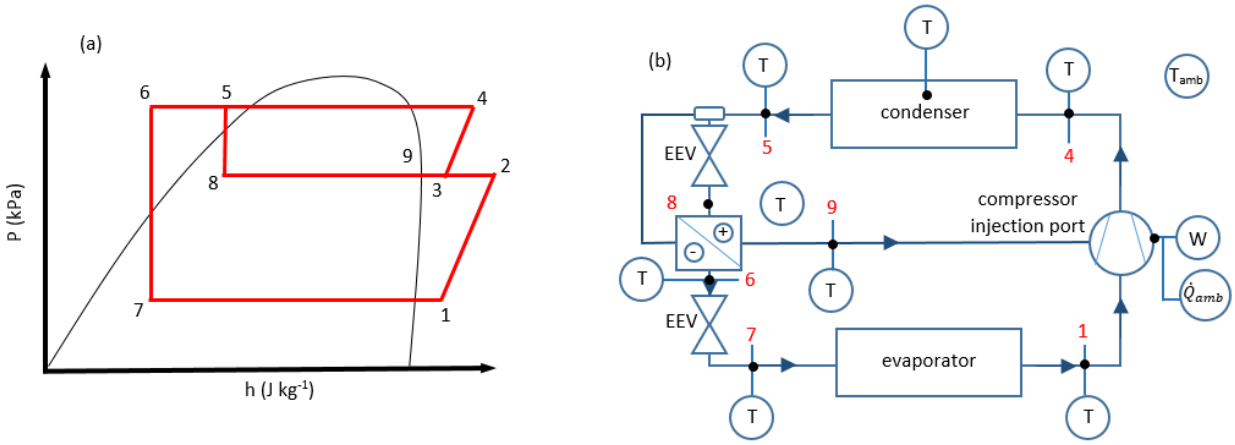

Figure 1.7. *Refrigeration cycle P-h diagram (a) and schematic with required measurements (b) of IHX injection cycles*

The proposed method is incapable of determining the refrigerant enthalpy when the fluid is in two-phase state due to unknown vapor quality. The fluid is certainly in vapor phase at compressor discharge (point 4, Figure 1.7). However, it can be diphasic at condenser discharge (point 5, Figure 1.7), compressor inlet (point 1, Figure 1.7), and injection port (point 9, Figure 1.7). In such cases, a simplification is introduced: the method supposes that the fluid is in saturated state and, thus, the enthalpy determination is possible. During real-time measurements, if the uncertainty of the method is greater than the superheat and subcooling at compressor inlet (point 1, Figure 1.7) and condenser outlet (point 5, Figure 1.7), respectively, then the refrigerant is assumed to be in two-phase state and the enthalpy is determined assuming that the fluid is in saturated state. However, it must be noted that two-phase phenomena at compressor inlet and condenser outlet are, either rare, or the duration is brief. Hence, the effect of this simplification on the seasonal performance of an appropriately designed functional HP system can be considered negligible. Two-phase condition at the compressor injection, on the other hand, is non-negligible as it may result from system control.

1.2.2 Influence of compressor heat losses

The method was experimentally validated in basic cycle air-to-air HP system in Tran *et al.* (2013) in various operating conditions. Refrigerant fluid used in the experimental setup was R410A and compressor type was rotary, and the method was compared to intrusive reference method, developed and validated in Tran *et al.* (2012), where Coriolis mass flow meter and intrusive pressure sensors were used. The deviation in the

refrigerant pressure determined from saturation temperature measurements is 2.7% in comparison with a direct low pressure measurement. The deviation between the indirectly measured mass flow rate, Eq. (**1.10**), and the values measured using a mass flow meter was below 4%.

The method, extended to injection cycles, was also validated in an IHX HP system using experimentally obtained data in several operating conditions by Goossens, *et al.* (2016). Scroll compressor and R407C refrigerant were used during the tests. Since there is no reliable performance measurement method available for comparison in air-to-air HPs, the method was validated in air-to-water HP operating in heating mode in laboratory conditions, where the water enthalpy method is used as a reference method. The maximum deviation between the COP values obtained from performance assessment method extended to IHX injection cycles, described in Subsection 1.2.1 (IHX HPs), and the reference COP values obtained from water side measurements was below 8%.

Tran *et al.* (2013) showed that the influences of indirect pressure measurements are insignificant when compared to compressor heat losses and oil mass fraction, even if the fluid is strongly zeotropic. On the other hand, compressor heat losses influence significantly the overall accuracy of the method.

The presented method integrates a simplified model of compressor heat transfer towards the ambient air. Compressor heat loss expression is composed of two parts – heat transfer by convection and radiation – as follows:

$$\dot{Q}_{amb} = h_c A\left(T_{comp,out} - T_{amb}\right) + \sigma A\left(T_{comp,out}^4 - T_{amb}^4\right) \qquad (1.19)$$

where h_c is the convective heat transfer coefficient, A is the surface area of compressor shell exposed to ambient air, T_{amb} is the ambient air temperature, $T_{comp,out}$ is the refrigerant temperature at the compressor exhaust side, and σ is the Stefan-Boltzmann constant. Compressor surface emissivity is assumed to be equal to unity and the emissivity of the surrounding air can be neglected. Convective heat transfer coefficient consists of three parts: convective heat transfer coefficient for isothermal cylinders (Morgan's correlation), and convective heat transfer coefficients for hot surface facing up and down (McAdams' correlations).

Tran *et al.* (2013) assumed that the shell temperature is homogenous and equal to discharge temperature. Particularly in scroll compressors, where the motor is on the bottom, this can provoke a significant error.

Tran *et al.* (2013) compared the compressor heat losses, $\dot{Q}_{amb}$, obtained from physical considerations, Eq. (**1.19**), to the reference values, $\dot{Q}_{amb}^{ref}$. Reference heat loss values were obtained from the compressor thermal balance, as follows:

$$\dot{Q}_{amb}^{ref} = \dot{W}_{comp} - \dot{m}^{ref}\left[\left(1 - C_g\right)\left(h_{r,comp,out} - h_{r,comp,in}\right) + C_g \Delta h_o^{T_{comp,in} \to T_{comp,out}}\right] \tag{1.20}$$

where $\dot{m}^{ref}$ is the mass flow rate of the working fluid measured with a flow meter. The ratios between $\dot{Q}_{amb}/\dot{Q}_{amb}^{ref}$ lie between 0.7 and 1.2. Based on this information Tran *et al.* (2013) derived a relative uncertainty value of estimated heat losses, Eq. (**1.19**). After performing an uncertainty analysis, it was determined that compressor heat loss terms are responsible for a relatively large portion of the relative uncertainty of heating capacity: the sensitivity index of compressor heat losses was 40%. **Consequently, a more comprehensive and reliable method for evaluating compressor heat losses on-field must be established to decrease the uncertainty of the performance assessment method.**

1.3 Fault detection and diagnostic using mass flow rate measurements

The performance assessment method determines indirectly the refrigerant mass flow rate. This information not only supplies valuable real-time performance data but also provides means to integrate diagnostic features. In other words, the performance assessment method can be coupled with an appropriate fault detection and diagnostic (FDD) method. A more elaborate analysis of FDD methods is presented in Appendix A. In addition, the appendix presents in more detail a promising FDD method, described in the work of Li & Braun (2007), that can be coupled with the performance assessment method.

1.3.1 Main faults in the heat pump unit

On-field efficiency degradation can result from faults occurring in the heating/cooling system. These faults are classified in two categories, those occurring in the thermodynamic cycle of the HP unit, the refrigeration cycle, and those occurring on a system level, such as installation and control faults (Madani, 2014).

Refrigeration cycle faults are the most difficult and expensive to diagnose, according to Li & Braun (2009). These faults complicate maintenance of the machine and promote unnecessary costs. According to case studies done by Downey & Proctor (2002),

and Li & Braun (2007) more than 50% of on-field packaged air conditioning systems were improperly charged due to improper commissioning or refrigerant leakage. Faults that are common in air conditioners (ACs) are common in HPs as well, since ACs are practically HPs operating in cooling-only mode. Cowan (2004) estimated that 5% to 11% of energy costs can be reduced with proper refrigerant charge. It is, therefore, essential to detect and distinguish different faults during installation and, specifically, operating phases, in order to ensure proper maintenance process of the machine and thus, its high performance level, durability, and potential to reduce greenhouse gas emissions during the whole life cycle.

A number of researchers, such as Madani & Roccatello (2014), have conducted extensive literature reviews on the most frequent and costliest faults. In addition, an abundant amount of information regarding these faults is available on HP troubleshooting forums. Faults presented in this section occur in the HP refrigeration cycle only, not the whole heating/cooling system.

Table 1.1 groups the most frequent individual faults in broader categories (grouped faults) and presents the consequences (operating issues) of each fault group on the machine performance. The list is not exhaustive, only the most typical issues are presented. Six fault categories were identified as the most common ones: control/electronics, exchanger fouling, leaking valves, refrigerant issues, superheat issues, and defrosting issues. It must be pointed out that some faults may be interconnected. For example, defrosting issue can be a result of poor defrost activation setting, or be a consequence of an electrical issue and, thus, be classified as a control/electronics fault.

Sensor issues, specifically temperature sensor issues, tend to occur frequently in both air-to-air and air-to-water HPs provoking a number of operating faults. Outdoor temperature sensors are damaged more easily since they are exposed to outside air, where air moisture can enter and freeze inside the sensor. Also, during defrosting period there is a rapid temperature change which can lead to thermal material stresses and, thus, damage the temperature sensor.

Another reason for faulty temperature sensors is bad wiring and loose contacts. Faulty pressure switches occur commonly in air-to-water HPs. Pressure switches may falsely signal that the pressure is too low due to dirt or dust accumulation or due to high vibrations at the compressor discharge line.

Typically, **exchanger fouling** is a result of dirt or frost accumulation on the indoor/outdoor coil or filter, which in turn provokes cooling/heating issues. As the exchanger fouls, the air free flow area and/or coil surface for effective heat exchange is decreased, which in turn increases the pressure drop of air passing through the exchanger, which decreases the air flow. Hence, the heat exchange between the air and the refrigerant is

deteriorated. In addition, frost or dirt can impact the heat transfer coefficient directly by providing an insulating resistance.

In heating mode, the coil temperature of the outdoor exchanger (evaporator) must be cooler than the ambient temperature for heat to be transferred from the ambient air to the coil. If the ambient temperature is below or close to zero, then the coil temperature will most certainly be below zero. Since water freezes at zero at ambient pressure, water droplets in the air will start to freeze on the heat exchanger coil causing frost formation. Typically, activating the defrosting cycle removes the frost formed on the evaporator. There are various defrosting triggering methods, such as setting fixed intervals for defrost on/off cycles, or activating the defrosting cycle after measuring the temperature difference of the ambient and coil temperatures using a thermostat. Faults associated with the **activation of defrosting cycle** can trigger heating/cooling issues, since it leads to frost accumulation on the outdoor coil.

Compressor valve/reversing valve leakage can contribute to cooling/heating issues as well. Compressor valve leakage creates backflows of high pressure refrigerant into the low pressure side of the heat pump system. This in turn provokes losses in the volumetric efficiency and refrigerant mass flow rate.

Refrigerant undercharge/overcharge can originate from incorrect initial refrigerant charge and refrigerant undercharge can originate also from **leaking valves**. These faults, as well as **impurities in the refrigerant**, such as the presence of a non-condensable gas, can deteriorate the thermal capacity of the unit.

Table 1.1 *Most common faults occurring in the HP unit*

Grouped faults	Individual faults (origins)	Operating issues
Control/electronics	• Wiring problems • Loose terminals • Electrical problems in the motor • Compressor overloaded – overload relay problems • Electrical problems in auxiliary components • Sensor issues	Startup Cooling Heating General

Exchanger fouling (condenser/evaporator)	• Dirty indoor/outdoor coil • Dirty indoor/outdoor filter • Frost accumulation (evaporator)	Cooling Heating General
Leaking valves (valve issues)	• Reversing valve • Suction/discharge valve in compressor	Cooling Heating General
Refrigerant issues	• Impurities • Undercharging (leaks) • Overcharging	Cooling Heating General
Superheat issues	• Faulty component • Sensor issues • Poor adjusting of the expansion valve	Cooling Heating General
Defrosting issues	• Poor parametrization of defrost activation cycle • Sensor issues	Cooling Heating General

Superheating issues also contribute to the deterioration of unit thermal capacity and originate from faulty, blocked, or poorly adjusted expansion valve.

1.3.2 Fault detection and diagnostic method

Current fault detection and diagnostic methods are typically based upon pressure and temperature measurements, which are then compared to the values provided by manufacturers in fault-free conditions, referred to as reference values. Any deviation of the measured value from the reference value indicates a fault. Identifying and distinguishing faults with such method is challenging. In addition, the method requires a physical intervention and the fault has already had time to impact the performance of the machine. Ideally, the purpose of FDD methods is to track in real-time the evolution of fault indicating parameters to detect specific faults before they have an impact on the COP.

Fault detection and diagnosis methods range from detailed physical models to simple polynomial black-box models. Different models show advantages and disadvantages in terms of applicability of on-field implementation, cost, accuracy, and data required. Ideally, FDD methods utilize low cost sensors, such as temperature sensors, and preferably sensors that are already integrated in the machine or as little supplementary sensors as possible in order to keep the hardware costs at minimum. FDD method must

guarantee a compromise between hardware cost and diagnosis quality in terms of accuracy, applicability to a wide range of different HP types and sizes, and low computational effort for on-field calculations.

As mentioned above, real-time measurements of the mass flow rate via component energy/mass balances calculated using surface mounted temperature and indirect pressure measurements provide valuable information, concerning not only performances, but also machine diagnostics, on-field. This information coupled with some complementary measurements constitutes a practical and promising FDD tool, termed **decoupling-feature diagnostic method**, as presented in the work of Li & Braun (2007). Li & Braun (2009) extended the method to HPs by including the detection of reversing valve and check valve leakage.

In the method of Li & Braun (2007), each of the fault indicating physical parameters, *i.e.* decoupling features, is uniquely influenced by individual faults. Decoupling features are also insensitive to variations in ambient conditions. Any deviations of these feature values from their reference values indicates a fault in the system. Reference values are evaluated in fault-free conditions, for example, from compressor and fan maps, typically provided by equipment manufacturers.

Decoupling features are determined using physical and virtual sensors. The goal of employing virtual sensors is to limit the use of potentially intrusive system measurements. Compressor energy balance, used for indirect evaluation of refrigerant mass flow rate, Eq. (**1.9**), is an example of a virtual sensor. Another example of a virtual sensor is energy balances with refrigerant and air-side measurements used to estimate exchanger air flow rate. Saturation pressures are estimated with the aid of property relations and mounted surface temperature sensors at locations where refrigerant is in saturated state. Hence, virtual sensors are used to evaluate condensation and evaporation pressures.

Most common faults occurring in residential HPs, such as charge faults and heat exchanger fouling, can be detected with the embarked FDD method solely with the aid of non-intrusive low-cost sensors, particularly temperature sensors. The following list is an example of faults that can be analyzed with the decoupling feature-based diagnostic technique:

- refrigerant overcharge,
- refrigerant undercharge,
- evaporator fouling,
- condenser fouling.

To sum up, the benefits of the method include on-field applicability, low calculation effort, low implementation cost, and its capacity to adapt to numerous vapor compression cycles, since fault detection is based on physical phenomena of thermodynamic cycles.

This particular FDD method coupled with the performance assessment method could be experimentally validated using air-to-air or air-to-water HPs. A more detailed presentation of the method and how it can be used to analyze the most common faults in the HP unit (refrigerant overcharge/undercharge, exchanger fouling) can be found in Appendix A, which can also serve as groundwork for the experimental validation of the FDD method.

1.4 Conclusions

Currently, manufacturers supply HP performance data obtained in standardized and controlled laboratory conditions. This data might not be representative of the performance data obtained on-field, due to installation quality, system design, climatic conditions, and faults occurring in the system. For this reason, estimating the performances of residential HPs, in terms of heating capacity and COP values on-field and in real-time, is of great importance when optimizing energy consumption.

Determining the performances of air-to-air HPs is, particularly, problematic, given that measuring accurately the enthalpy and, specifically, the mass flow rate of air is challenging. Tran *et al.*, (2013) adapted a method that is based on the refrigerant fluid measurements and component energy/mass balances to estimate the performances of such HPs on-field in real-time. Nonintrusive sensors, such as surface temperature sensors, are used to estimate pressure and refrigerant mass flow rate in different types of heat pump systems, including air-to-air. The method was then extended to comprehend more complex cycles, such as IHX and FT injection cycles.

The method integrates the evaluation of compressor heat losses, *i.e.* the heat transfer from compressor shell towards the ambient air. Tran *et al.* (2013) determined that the sensitivity index of compressor heat losses in the relative uncertainty of heating capacity calculated by the method is 40%. This highlights the importance of developing a more comprehensive and reliable method for evaluating compressor heat losses on-field in order to reduce the uncertainty of the performance assessment method. Compressor heat loss model already integrated in the method assumes that compressor shell temperature is uniform and equal to the refrigerant temperature at discharge. This is, specifically not the case in scroll compressors, where the compression chamber is typically at the top of the compressor.

In order to determine a more comprehensive heat loss evaluation method, the thermal behavior of rotary and scroll compressor shells in various operating conditions must be investigated, and an appropriate estimation method of T_{shell} must be selected. Numerical models developed to serve this purpose are presented in Chapter 2. Furthermore, a literature review on the available convective heat transfer correlations must be performed. Correlations that are best suitable for the physical nature of heat transfer and geometry are presented in Chapter 3.

The performance assessment method determines the refrigerant mass flow rate, $\dot{m}$, in real-time. This information can be integrated in a physical FDD model presented in the work of Li & Braun (2007). The performance assessment method can be used in this context as the virtual sensor to measure the refrigerant mass flow rate along with evaporation and condensation pressures, information that is necessary in the particular FDD method. One suggestion for future development, elaborated in Conclusions and perspectives section of this thesis, is experimentally testing the most common faults occurring in HPs in order to determine the validity of the FDD method.

CHAPTER 2

COMPRESSOR HEAT TRANSFER MODEL

Afin d'améliorer l'évaluation des pertes thermiques du compresseur in situ, le comportement thermique de l'enveloppe de deux types de compresseurs (scroll et rotary) est investigué. Le profil thermique extérieur du compresseur dépend de la distribution de chaleur à l'intérieur. Pour cette raison, l'intérieur des compresseurs doit être modélisé.

La modélisation hybride, qui combine les formulations intégrales et différentielles, a été choisie. Ce type de modélisation est plus flexible en termes d'applicabilité à différents types de compresseurs et est moins couteux en temps de calcul que la modélisation différentielle. De plus, l'approche hybride fournit également des résultats plus précis qu'une approche intégrale.

Deux modèles hybrides ont été développés pour les compresseurs de type de scroll et rotary. La méthode de calcul dans les modèles est divisée en trois étapes fondamentales : l'analyse du cycle thermodynamique, l'analyse thermophysique détaillée de l'écoulement et l'analyse du réseau thermique du compresseur.

Les résultats obtenus avec ces modèles sont présentées dans le chapitre 3. Ces résultats sont ensuite utilisés dans le chapitre 4 pour déterminer quelles zones contribuent le plus aux pertes thermiques et quelle zone de l'enveloppe du compresseur est la plus représentative pour déterminer la température moyenne de l'enveloppe ou de la zone de l'enveloppe lorsque plusieurs zones sont considérées.

2.1 State-of-the-art of compressor heat transfer

Performance assessment method described in the work of Tran *et al.* (2013) integrates a simplified model of compressor heat losses, Eq. (**1.19**), that influences significantly the overall accuracy of the method. As mentioned earlier, it was shown that the sensitivity index of heating capacity uncertainty predicted by the internal refrigerant method is 40 %. Thus, a more precise on-field evaluation of compressor heat losses is required in order to improve the performance assessment method.

Examining the thermal profiles of rotary and scroll exterior shells in various operating conditions provides valuable information: the number and location of surface temperature sensors as well as calculation methodology used to measure heat losses on-field can be identified. Exterior thermal profile reflects the thermal behavior of interior components. Thus, overall heat transfer within the compressor domain must be investigated. The computational domain must include internal components that are critical from the heat transfer point of view. For this purpose a numerical model described in Section 2.2 was developed. The model predicts thermal profiles of the exterior shell in various operating conditions in scroll and rotary compressors.

Modeling heat transfer within compressor domain is a challenging task. The complexity of compressor geometry hinders simplifications and contributes to various complex flow and heat transfer phenomena. However, modeling the thermal behavior of compressors tends to be of interest, since interior temperature and pressure distributions at various operating conditions provide valuable information when considering compressor performances, component and material durability, and heat transfer towards the ambient air. Experimental and numerical approaches are, typically, used for this purpose. A short literature review in the following subsections highlights the state-of-the-art of compressor heat transfer modeling. The purpose of this literature review is to help determine the most adequate numerical modeling technique required to establish the thermal behavior of scroll and rotary compressor exterior shells.

2.1.1 Correlations based on experimental measurements

Experimental techniques, where thermocouples are placed inside and/or outside the compressor, are one of the most straightforward and conventional ways to investigate the thermal behavior of compressors (Ribas, *et al.*, 2008). This approach is intrusive and the location of sensors has to be considered very carefully for the flow dynamics and heat transfer inside the compressor to remain unaffected. In addition to thermocouples, heat flux sensors and infrared cameras can be used to investigate the thermal behavior of compressors. Heat flux sensors used in the work of Dutra & Dechamps

(2013) can be seen in Figure 2.1. More information on the advantages and disadvantages of the listed experimental techniques can be found in Appendix B.

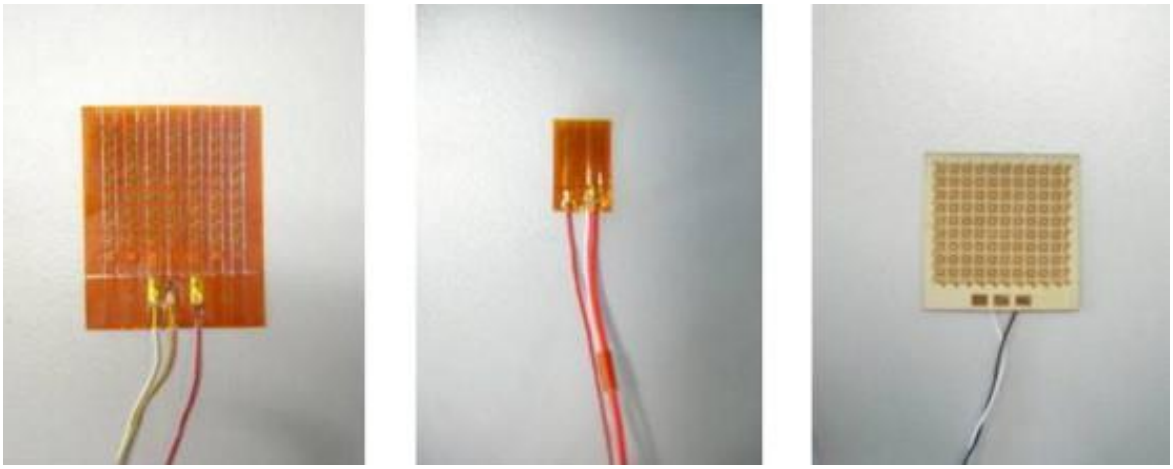

Figure 2.1. *Example of heat flux sensors used to measure compressor heat fluxes in the work of Dutra & Deschamps (2013)*

Experimental data is used to identify the most significant heat transfer zones and mechanisms between component surfaces and the surrounding fluid by locating hot and cold spots within the compressor (Jang & Jeong, 2005). Correlations for compressor heat losses and component thermal conductances are derived from the acquired experimental data.

Derived heat transfer correlations are typically functions of variables that can be measured on-field, for instance, condensation temperature. Correlations can also be used in some numerical models (Diniz, *et al.*, 2015). Some correlations are developed solely with mathematical data analysis methods and have no physical basis. Others are a combination of mathematical and physical analyses. However, the accuracy and overall validity of the derived correlations is limited/unknown outside the calibration range, since they are based on the data obtained from a limited number of operating conditions. Furthermore, such models cannot be adjusted by changing a coefficient/parameter to account for *e.g.* compressor layout modifications or change of refrigerant type (Kim & Bullard, 2002).

More accurate experimental models based on a wider range of operating conditions can guarantee relevancy and sufficient accuracy of the model in various operating modes (different refrigerants, compressor types, rotation speeds, condensation temperatures, *etc.*) However, such models, typically, involve too many variables that are hard to measure on-field, such as the mechanical characteristics of the compressor, *i.e.* volumetric, isentropic efficiencies, *etc.*, required to account for modification in operating modes (Duprez *et al.*, 2010).

2.1.2 Numerical models

Numerical models consist of three different approaches: integral, differential, and hybrid. The choice of modeling approach depends on the desired level of complexity, versatility and application of the model.

Integral models

Integral models consist of building a system of steady or unsteady state energy balance equations (integral formulations) for each control surface. They are often referred to as lumped conductance or thermal network (TNW) models. Control surfaces are usually limited by the geometrical boundaries of the compressor solid components for convenience reasons. With the appropriate energy balances and heat transfer coefficients the compressor components are thermally interconnected, thus forming a network.

Padhy (1992), Sim *et al.*, (2000) and Ooi (2003) developed compressor heat transfer models by deriving heat transfer coefficients using correlations already available in the literature. In this case, the model does not rely on experimental data and can be applied to a wide range of operating conditions. Nevertheless, the accuracy of the model suffers, since there is only a limited number of heat transfer correlations available in the literature and some correlations are poorly adapted to the complex flow pattern and geometries of internal components. Also, a good understanding of the main heat transfer mechanism in every single element is necessary to employ appropriate heat transfer correlations.

Another approach is to use experimental data to calibrate thermal conductances, as in the model developed by Todesca *et al.* (1992). Yet, if the operating conditions deviate significantly in comparison with the reference conditions used to calibrate the model or the compressor internal component layout is modified, experimentally derived thermal conductances need to be corrected, which makes the model less flexible.

The main advantage of the integral method is its relative simplicity and flexibility to adapt to different compressor types and internal component layouts. The main disadvantage of this modeling approach is its poor accuracy originating from the need to assign heat transfer coefficients, difficulty to model multidimensional heat conduction between solid components, and the potential necessity for extensive iterations.

Differential models

Differential models solve the governing partial differential flow equations for each control volume or element. Flow equations consist of mass, momentum, and energy

equations, and typically require the aid of a computational fluid dynamics (CFD) program for their resolution. Differential models can predict flow and thermal profiles in a compressor design.

In the works of Chikurde *et al.* (2002), Birari *et al*. (2006), Pereira & Deschamps (2012), and Raja *et al*. (2003) steady-state thermal behavior of a hermetical reciprocating and scroll compressors is simulated, where different compressor component zones are assigned as heat sources/sinks resulting from motor losses (electrical losses), frictional losses (mechanical losses), and heat losses due to a non-isentropic compression process (thermodynamic losses), using a commercially available CFD code (ANSYS Fluent). The models are validated with experimental results.

The main advantage of such models is that the use of heat transfer coefficients or experimentally calibrated thermal conductances can be avoided. For this reason, practically, any internal component layout can be modeled. Such models provide a very accurate and detailed thermal analysis for a variety of operating conditions. The disadvantages of such models are that the developed model is usually compressor design specific and the computational processing time is quite high and requires powerful computers. In addition, developing differential models for entire compressor domains is time-consuming and some complex physical phenomena inside the compressor, such as flow of lubricating oil, complicate significantly the modeling strategies.

Hybrid models

Hybrid models resolve integral and numerical formulations in a coupled manner: thermal network models are used to optimize simplified CFD models (Diniz *et al.*, 2015). Thus, hybrid models are a compromise between differential and integral models. Hybrid methods assign heat transfer coefficients, as in the case of integral models, and/or other necessary information as boundary conditions to represent the effects of flow dynamics on the heat transfer between solid and fluid interfaces. This eliminates the need to create complex, computationally expensive and detailed differential models. For instance, modeling in detail rotations and other movements of interior components and their effects on the flow and heat transfer can be avoided in the CFD geometry, mesh, and setup. In this case differential formulations resolve the evolution of flow inside the compressor and its effects on the component wall temperature with relatively low computational costs and limited complexity.

Hybrid modeling approach is, typically, customized, *i.e.* different variations of the modeling types and optimization techniques are possible, as long as both types of formulations, integral and differential, are integrated in the model. Hybrid models presented in the works of Almbauer *et al.* (2006), Sanvezzo & Deschamps (2012), and Ribas (2007) have a common approach: they model part of the domain, typically, the

solid components and conduction within them, using differential equations, and the fluid domain using integral formulations.

The main advantage of hybrid models is that they tend to be more accurate than integral models while remaining relatively simplified and more flexible in terms of compressor design and applicability in comparison with differential models (Ribas *et al.*, 2008). The model is partly resolved using differential equations and can, thus, resolve heat conduction in solid components. A disadvantage is that some hybrid models require experimental data to determine heat transfer coefficients. In this case, the accuracy of model is restricted to a specific range of operating conditions, as in the hybrid model of Diniz *et al*. (2015).

Figure 2.2 is a graphical illustration of an example of a hybrid model. Motor assembly enclosed in the compressor shell with the surrounding fluid is portrayed in the figure. Conduction within a volume is modeled with differential formulations and heat transfer between solid and fluid components is modeled with integral formulations. Information is exchanged between integral and differential approaches until convergence is achieved. In Figure 2.2 Δx and Δy are spatial mesh sizes in *x* and *y* directions.

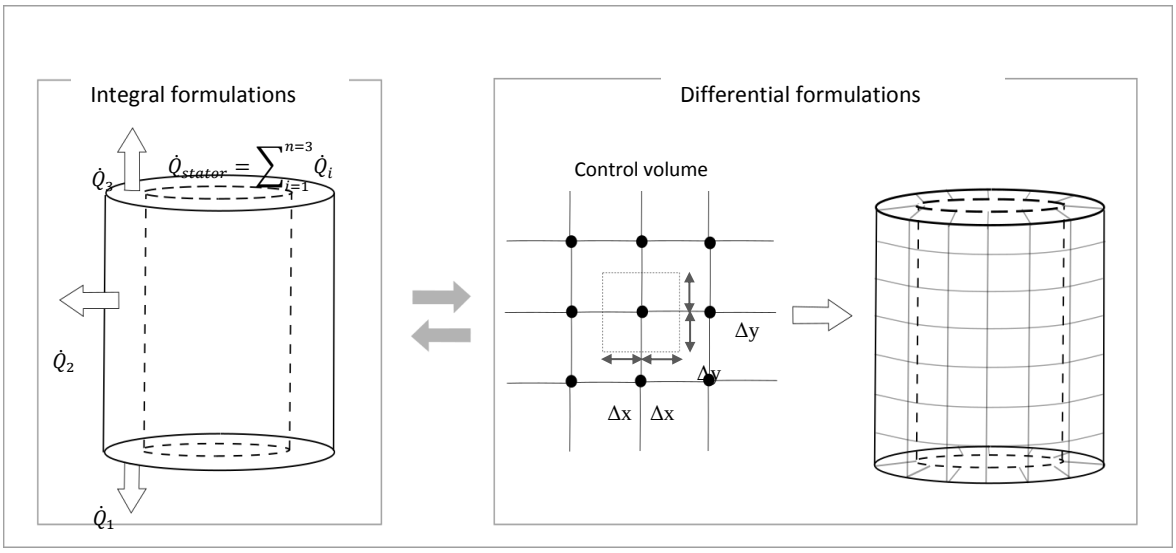

Figure 2.2. *Illustration of a hybrid model approach when modeling heat transfer of stator*

Most hybrid models found in literature consider reciprocating compressors. Diniz *et al.* (2015) developed a hybrid thermal model for scroll compressors. However, the model integrates a detailed modeling of the scroll wraps to obtain temperature distribution along this component. Thus, the model cannot be adapted to rotary compressors as well. Also, thermal profile of compressor shell, as well as heat transfer from the

shell towards the ambient air was not a primary interest of the hybrid models found in literature. The focus of these works was to provide information on the distribution of temperature inside the compressor as well as to investigate gas superheat, *i.e.* heating of the gas as it passes by the hot motor when flowing from the inlet port to the compression chamber. This observation concerns not only the aforementioned hybrid models but also the previously presented differential and integral models. The variation of compressor exterior thermal profile and heat losses in various operating conditions was encountered in none of the presented studies.

2.2 Numerical model of compressor heat transfer

Thermal profiles of compressor exterior shell must be investigated in various operating conditions in order to establish an improved on-field compressor heat loss evaluation method. The developed numerical model must comprehend two hermetic compressor technologies: rotary and scroll. The goal of the model is to avoid referring to a great deal of costly, time-consuming, and technical expertise-requiring measurements. The developed model must possess sufficient accuracy with relatively low computational costs. For the reasons stated here, hybrid model was selected as the most adequate approach. Hybrid models do not rely on complex and detailed CFD models, making them more robust in terms of compressor types and different component layout applicability, yet they are generally more accurate than integral models.

2.2.1 Modelling approach

The developed hybrid model comprises a 3D CFD model that solves partial differential flow equations in order to perform a more elaborate flow and heat transfer analysis, supported by a code written in MATLAB, representing the thermodynamic compression cycle and a thermal network of the compressor domain in 2D. Integral formulations representing various heat transfer configurations of the internal component surfaces and the surrounding fluid in MATLAB are used to verify and validate calculation results obtained from the CFD code. This helps maintain the differential part with low computational costs and limited complexity level, and ensures compressor design flexibility. Thus, the two modelling approaches, integral and differential, are coupled.

The calculation procedure can be divided into three fundamental steps: thermodynamic cycle analysis, detailed thermophysical flow analysis, and compressor thermal network analysis, as depicted in Figure 2.3. The comparison of the $\dot{Q}_{comp}$ values, which is the heat released by the internal components, calculated in the first and third step of the model, is used as the convergence criteria.

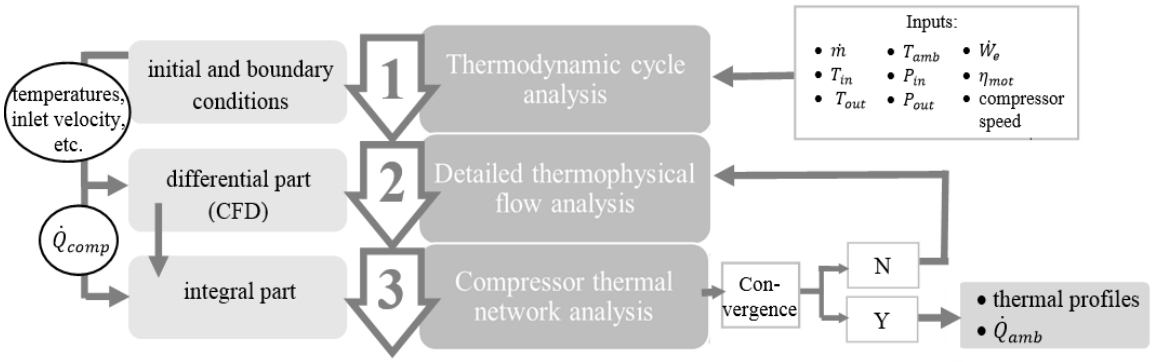

Figure 2.3. *Schematic of the three calculation steps of the model*

Essentially, MATLAB is used to solve a network of energy transfer equations between the solid-fluid interfaces by convection, where heat transfer coefficients are taken from literature. The net energy obtained from these equations (*i.e.* released by the components) must equal to the sum of energy absorbed by the fluid and released to the ambient air.

In order to obtain the net energy released by the components, heat transfer coefficients must be known, which in turn requires the temperatures of the solid components and surrounding fluid, as well as the refrigerant velocities near the solid components. These values can be obtained through an iterative process. Yet, a hybrid model allows to calculate these values with the help of a CFD code. The model in FLUENT performs only a thermal and velocity analyses inside the compressor domain. The values obtained from FLUENT, surface temperatures of components and refrigerant velocities, are communicated to MATLAB and integrated in the thermal network. If the energy is conserved, *i.e.* **the net energy released/absorbed by the fluid, $\dot{Q}_{comp}$, calculated from the thermodynamic analysis (first step) is equal to the net energy released/absorbed by the components, $\dot{Q}_{comp}$, calculated from the thermal analysis (third step), the calculations have converged.** In this case external thermal profiles, which is the primary outcome of the hybrid model, are extracted from the CFD part of the model (second step).

Figure 2.4 (a) and (b) are representations of the computational domains of scroll and rotary compressors, respectively. The model is simplified by removing unnecessary fillets and parts in order to facilitate the meshing in the pre-processing stage and convergence in the CFD solver. Compressor is surrounded by ambient air with enclosure walls maintained at a constant temperature. Depending on the configuration, compres-

sor shell can either be exposed to forced or natural convection. The geometrical domain consists of compression chamber, crankshaft, compressor shell, oil sump at the bottom, rotor, and stator. The listed components were considered as the most essential from the heat transfer point of view.

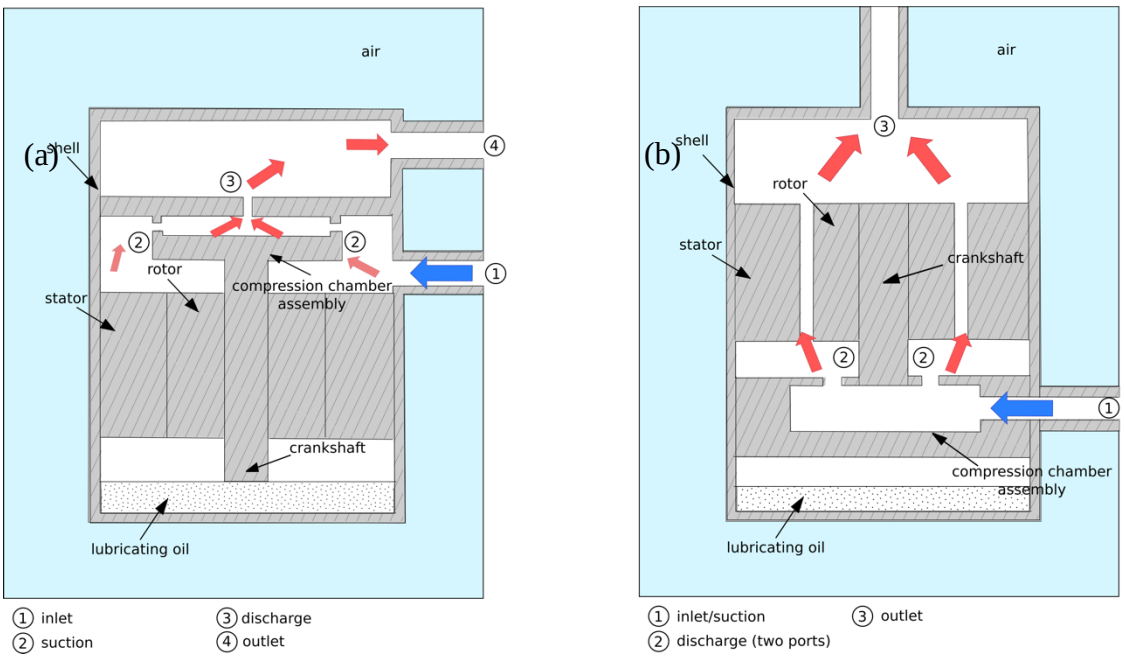

Figure 2.4. *Computational domains of scroll (a) and rotary (b) compressors*

In scroll compressors, the fluid enters from the inlet port (point 1, Figure 2.4 (a)) and passes through the hot motor assembly (rotor-stator) undergoing slight superheating whilst cooling the mentioned compressor components. Next, the refrigerant is directed to enter the compression chamber though the suction cavities (point 2, Figure 2.4 (a)). After compression the gas passes through the discharge cavity (point 3, Figure 2.4 (a)) and exits the compressor from the outlet port (point 4, Figure 2.4 (a)).

In rotary compressors, the fluid enters from the inlet port (point 1, Figure 2.4 (b)) located at the bottom of the compressor and passes directly into the compression chamber. After undergoing the compression process, the gas passes through the discharge port (point 2, Figure 2.4 (b)) and through the narrow gap between the rotor and stator, potentially heating the solid components. Next, the gas fills the discharge plenum and, finally, exits the compressor from the outlet port (point 3, Figure 2.4 (b)).

The model principle and calculation procedure illustrated in Figure 2.3 is identical for

both compressor types, scroll and rotary. Yet, each of the fundamental steps are customized for scroll and rotary domains. The model steps are described in more detail for scroll and rotary compressors in Subsection 2.2.2 and 2.2.3, respectively.

2.2.2 Scroll

2.2.2.1 Thermodynamic cycle analysis

The first part of the model analyzes the thermodynamic cycle in order to evaluate the boundary conditions, such as temperatures, inlet velocity, and heat sources, used in integral and differential parts of the model, steps two and three, respectively. In this part the heat released by the compression process, $\dot{Q}_{comp}$, is calculated. This variable is used in the third step of the model to determine whether the model has converged.

The net heat released by the internal components is:

$$\dot{Q}_{comp} = \dot{Q}_{suc} - \dot{Q}_{non-is} \tag{2.1}$$

where $\dot{Q}_{suc}$ is the heat released by the motor assumed to be equal to the superheat of the refrigerant gas passing from the compressor inlet (point 1, Figure 2.4 (a)) to the compression chamber (point 2, Figure 2.4 (b)), and $\dot{Q}_{non-is}$ is the heat absorbed by the components from the fluid due to a non-isentropic compression process (thermodynamic losses). Gas superheat is assumed to be equal to electrical losses dissipated as heat from the motor, located at the bottom of the hermetical compressor (Figure 2.4 (a)), as depicted below:

$$\dot{Q}_{suc} = (1 - \eta_{mot})\dot{W}_e \tag{2.2}$$

where η_{mot} is the motor efficiency and $\dot{W}_e$ is the electrical power input. In order to calculate $\dot{Q}_{non-is}$, the isentropic compression power must be known:

$$\dot{W}_{is} = \dot{m}\left(h_{dis,is} - h_{suc}\right) \tag{2.3}$$

where $\dot{m}$ is the mass flow rate of the fluid, h_{suc} is the refrigerant enthalpy at the suction chamber cavity, and $h_{dis,is}$ is the discharge enthalpy of an isentropic compression determined from:

$$h_{dis,is} = h(s(T_{suc}, P_{suc}), P_{dis}) \tag{2.4}$$

where P_{dis} is the discharge a pressure and $s(T_{suc}, P_{suc})$ is the fluid entropy at the suction chamber cavity. Consequently, $\dot{Q}_{non-is}$ is obtained from:

$$\dot{Q}_{non-is} = \eta_{mot}\dot{W}_e - \dot{W}_{is} \tag{2.5}$$

Refrigerant enthalpy at the suction cavity of compression chamber, h_{suc}, is calculated from suction heat and inlet conditions as follows:

$$h_{suc} = h_{in} + \frac{\dot{Q}_{suc}}{\dot{m}} \tag{2.6}$$

Figure 2.5 illustrates the refrigeration cycle of a heat pump and associated compressor power distributions. This step is coded in MATLAB. Refrigerant gas properties, such as enthalpies, are obtained from the libraries of REFPROP (NIST, 2008).

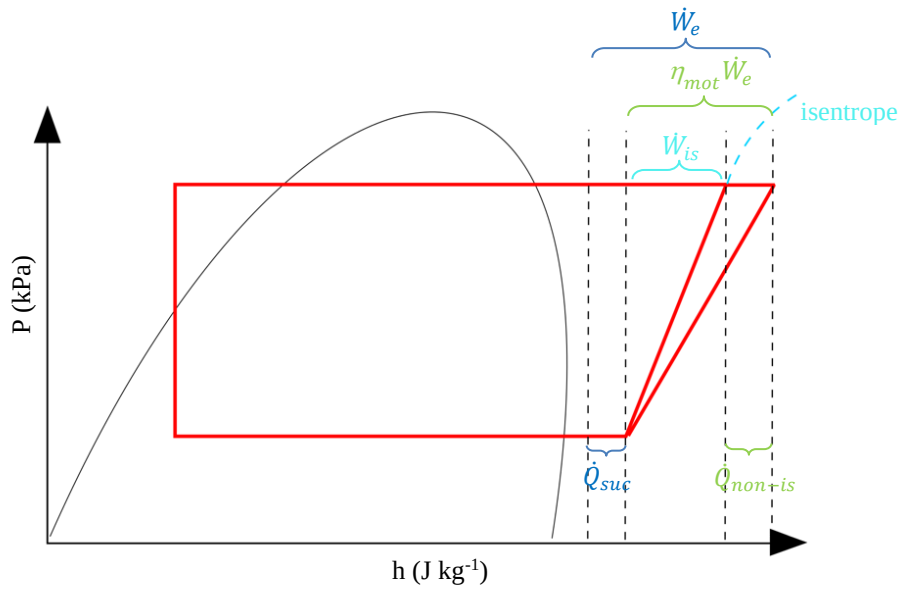

Figure 2.5. *Thermodynamic refrigeration cycle of a heat pump with associated power distributions inside the compressor*

2.2.2.2 Detailed thermophysical flow analysis

The second step of the model is executed in ANSYS Fluent, a CFD code based on finite control-volume technique to numerically solve a set of governing relations of fluid in motion. The output of this part of the model is refrigerant thermal and velocity profiles, as well as solid zone temperatures. This information is subsequently transmitted to the final step of the model in order to perform a TNW analysis that verifies the validity of the CFD simulation results.

The laws of fluid mechanics are governed by the conservation equations of mass, momentum, and energy. These equations, otherwise called flow equations, constitute a

system of partial differential equations (PDEs) in space or space-time, where second order is the highest space derivative. A set of equations, called Navier-Stokes (N-S) equations, is an example of flow equations with a specific degree of approximation, yet providing the most general flow description. These equations represent how the velocity, pressure, temperature, and density are related in a moving fluid and can be applied to linear Newtonian viscous fluids. Unsteady N-S equations consist of time-dependent conservation of mass, Eq. (**2.7**), momentum, Eq. (**2.8**), and energy Eq. (**2.9**):

$$\frac{\partial \rho}{\partial t} + \vec{\nabla} \cdot (\rho \vec{v}) = 0 \tag{2.7}$$

$$\frac{\partial \rho \vec{v}}{\partial t} + \vec{\nabla} \cdot \left(\rho \vec{v} \otimes \vec{v} + P\bar{\bar{I}} - \bar{\bar{\tau}}\right) = \rho \overrightarrow{f_e} \tag{2.8}$$

$$\frac{\partial \rho E}{\partial t} + \vec{\nabla} \cdot \left(\rho \vec{v} H - k\vec{\nabla} T - \bar{\bar{\tau}} \cdot \vec{v}\right) = W_f + q_H \tag{2.9}$$

where ρ is the fluid density, $\vec{v}(u, v, w)$ is a velocity vector with u, v, w components, $\bar{\bar{\tau}}$ is a stress tensor, P is the fluid pressure, $\bar{\bar{I}}$ is the unit tensor, $\overrightarrow{f_e}$ is the external force vector, k is the thermal conductivity, E is the total energy, H is the stagnation enthalpy, W_f is the work of external forces, and q_H is the external heat sources (Hirsch, 2007). Navier-Stokes equations are extensions of the Euler equations, which are used to describe inviscid flows.

The relations presented above, Eq. (**2.7**)-(**2.9**), are fairly general and need to satisfy only few restrictive assumptions:

- fluid forms a mathematical continuum,
- the particles are in thermodynamic equilibrium,
- only effective forces are due to gravity,
- heat conduction follows Fourier's law,
- there is no internal heat sources.

The equations are extremely complex since they are non-linear, coupled (*i.e.* must be solved simultaneously), three-dimensional, and time-dependent. For this reason approximation tools, such as control volume method (FVM), are used to solve these equations. In the FVM flow equations are represented in integral form in order to calculate the gross fluxes of mass, momentum, and energy passing through a finite region, control volume, of the flow. Other methods are finite difference method (FDM) and finite element method (FEM). More information about the conservation equations, their derivation, and resolution can be obtained from fluid dynamics text books, such

as Viscous Fluid Flow by F. M. White and Numerical Computation of Internal and External Flows by C. Hirsch.

Finite difference method consists of solving discretized PDEs by Taylor expansions. This method is applicable in practice only to structured grids. Finite element method, on the other hand, is most widely used in the world of structural mechanics. In finite element method, governing equations are transformed to weak formulations with some mathematical modifications using a weighting function.

Finite volume method is a technique that is most widely applied in CFD due to its generality, conceptual simplicity, and its ease of implementation to arbitrary structured and unstructured mesh. This method associates a local finite volume, or control volume, to each mesh point constituting a computational domain, once the grid has been generated. Conservation equations in integral form are applied to each local volume. Thus, in FVM the discretized space is formed by a set of small cells, where each cell is associated to one mesh point. Each cell center contains an unknown scalar quantity making FVM a cell-centered approach, unlike in the case of FDM and FEM.

The FVM discretization technique can be illustrated by considering a general form of a conservation equation for a scalar quantity U written in an integral form for an arbitrary control volume, Ω_J associated to mesh point j:

$$\frac{\partial}{\partial t}\int_{\Omega_j} U\, d\Omega + \oint_{S_j} \vec{F}\cdot d\vec{S} = \int_{\Omega_j} Q\, d\Omega \qquad (2.10)$$

where $\vec{F}$ flux vector, $\vec{S}$ is the surface vector, and Q is the source term.

The equation is then replaced by its discrete form:

$$\frac{\partial}{\partial t}\left(U_j\Omega_j\right) + \sum_{faces} \vec{F}\cdot\Delta\vec{S} = Q_j\Omega_j \qquad (2.11)$$

In discrete form, the volume integral is expressed as the averaged values over the cell and the surface integral is replaced by a sum over all the bounding faces of the considered Ω_j volume.

In steady-state and in the absence of source terms, the finite volume formulation reduces to a balance equation of all the fluxes entering and leaving the control volume:

$$\sum_{faces} \vec{F} \cdot \Delta\vec{S} = 0 \qquad (2.12)$$

Algebraic conservation equations are linearized in each cell forming a system of equations with a sparse coefficient matrix that can be solved numerically. Fluent solves the linear system using a point implicit (Gauss-Seidel) linear equation solver in conjunction with an algebraic multi-grid method. More information on the linearization and linear system solution method can be obtained from Hirsch (2007).

Geometry

The domain geometry of the CFD model is decomposed into solid and fluid zones. The subdomains are oil continuum (on the bottom of the compressor cylinder), discrete refrigerant fluid zones, surrounding air continuum, and solid zones bounded by simplified geometrical boundaries of the components. Figure 2.6 is the scroll computational domain drawn with the aid of ANSYS preprocessing tool, Designer Modeler. The computational domain consists of compressor shell, crankshaft, fluid gap between rotor and stator, suction and discharge ports, compression chamber, and cylinder inlet and outlet cavities through which the refrigerant enters and exits the domain. The computational domain in CFD is coherent with the TNW programmed in MATLAB (step 3, integral part of the model). The crankcase and rotor are modeled to be stationary, unlike in the TNW, where the parts in question are rotating.

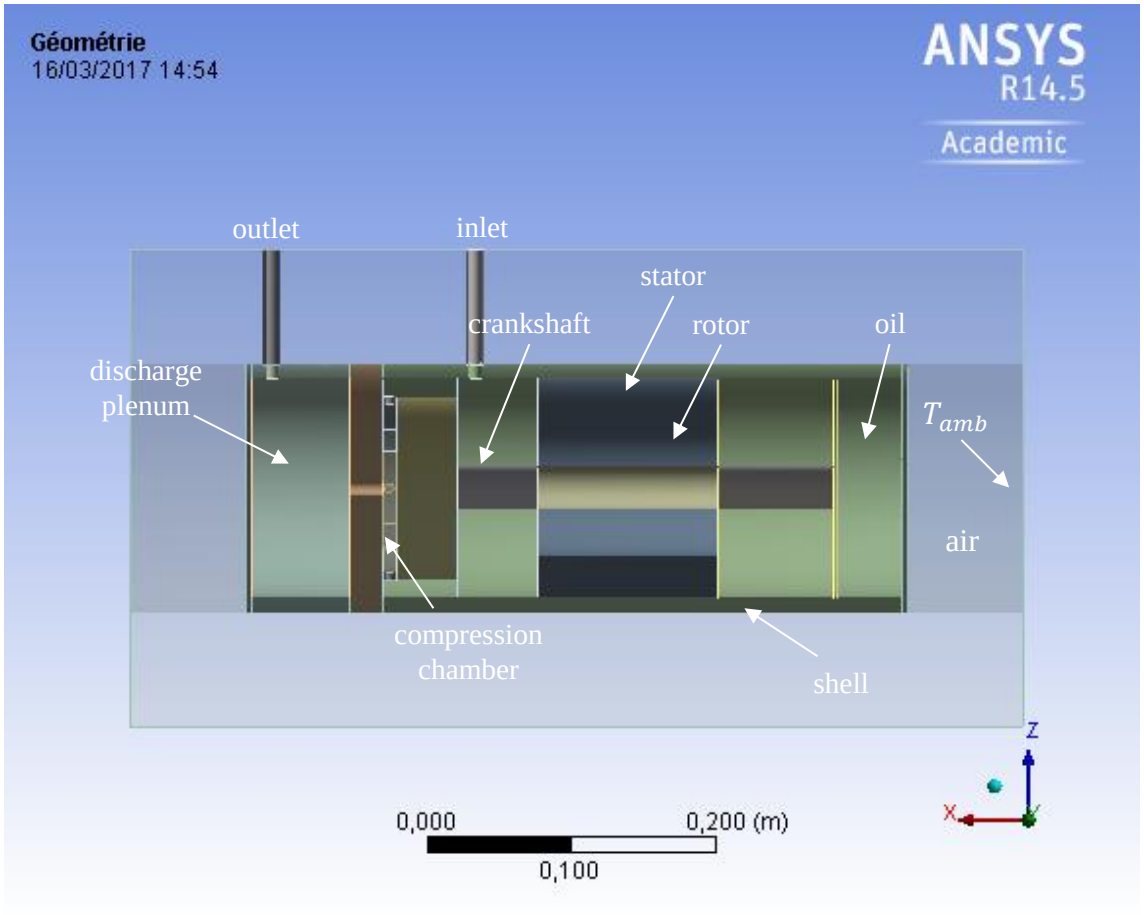

Figure 2.6. *Computational domain of scroll compressor in ANSYS Workbench pre-processing tool, Design Modeler*

Seeing that both compressor types, scroll and rotary, are hermetic ones, every part of the compressor assembly inside the shell is in contact with refrigerant or oil. However, to simplify the CFD model, oil is present only on the bottom of the compressor. Dimension parameterization was enabled in the geometry ensuring that the dimensions of the components can be easily changed when necessary.

Mesh

The scroll domain mesh consists of $3.19 \cdot 10^6$ tetrahedrons. The mesh type is unstructured. Unstructured mesh is defined by irregular connectivity typically of triangles in 2D and tetrahedral elements in 3D. Structured mesh typically comprises quadrilateral in 2D and hexahedral elements in 3D and the node connectivity follows a fixed pattern. Figure 2.7 is an illustration of structured and unstructured grids.

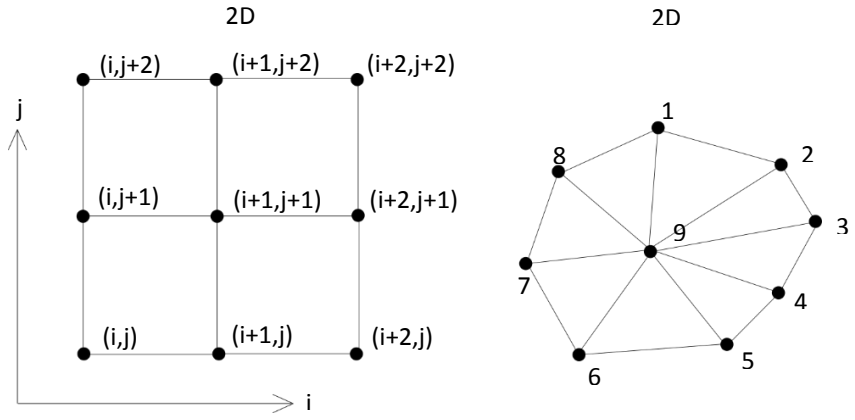

Figure 2.7. *Structured (on the left) and unstructured (on the right) grids*

Given the complexity of the geometry, it was nearly impossible to generate a structured mesh. Structured meshes are believed to generate more accurate solutions, however, the accuracy of the mesh depends on the flow problem in question. The adaptivity of unstructured mesh to more complex flows and geometry may generate more accurate solutions. However, the central processing unit time to attain convergence is longer in problems involving unstructured grids: calculating the residuals requires data of the neighboring nodes, which can be found by adding/subtracting 1 from the neighboring cell index of i, j space for 2D and i, j, k space for 3D in structured grids, which requires less storage, and, thus, faster execution. This is not the case for unstructured mesh types since explicit storage is required.

Meshed domain can be seen in Figure 2.8. The mesh was generated with the ANSYS Workbench meshing tool, Mechanical. Denser mesh is imposed in narrow passages and regions with more significant curvature, such as small cylindrical cavities (compressor inlet and outlet, suction and discharge).

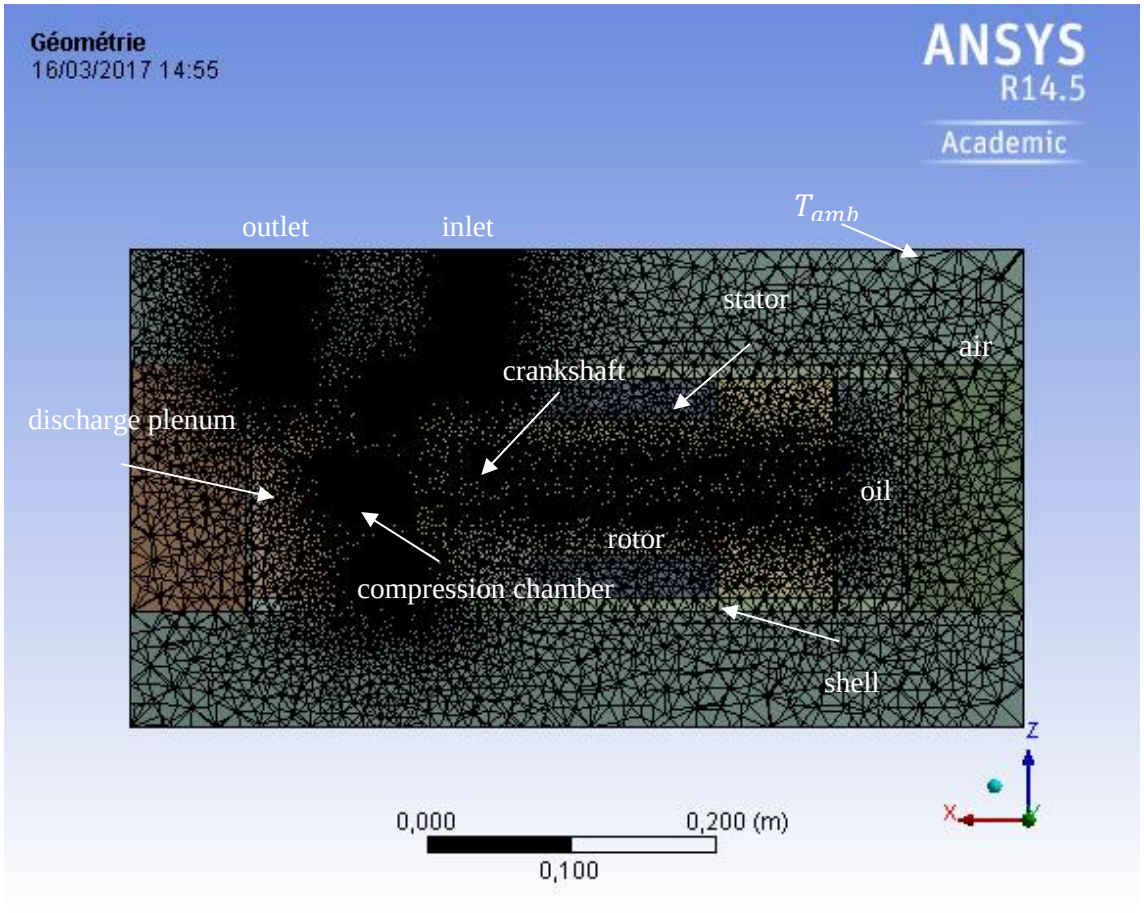

Figure 2.8. *Scroll compressor mesh in ANSYS Workbench pre-processin tool, Mechanical*

The average orthogonal quality of the mesh is 0.84. Orthogonal quality is calculated from the relationship of the vector that is normal to the edge of a face and the vector from the center of the face to the center of the edge. Its values range from 0 to 1, where 0 corresponds to low quality. The maximum aspect ratio of the mesh is 17.6 and average aspect ratio 1.85. Aspect ratio is the ratio of the longest edge length to the shortest edge length. Ideally, the aspect ratio will be 1, which is the case for an equilateral face or cell.

One the most important mesh quality measures is skewness, which determines how close to ideal shape, *i.e.* equilateral shape, a face or cell is. Figure 2.9 illustrates highly skewed versus equilateral element. Elements that have skewness close to 1 are defined as degenerate elements and significantly influence the quality of the mesh. Degenerate cells are characterized by nearly coplanar nodes. Skewness value close to 0 indicates an equilateral cell and is the best achievable skewness value. Cells beyond skewness

level of 0.98 were kept to a minimum – three elements have a skewness above 0.98. The average skewness in the scroll mesh was 0.23.

Skewness, orthogonal quality, maximum aspect ratio are three main parameters to evaluate the mesh quality. Mesh quality influences the convergence and the accuracy of the results. Based on the investigation of the mentioned quality parameters, it can be concluded that the mesh is of good quality.

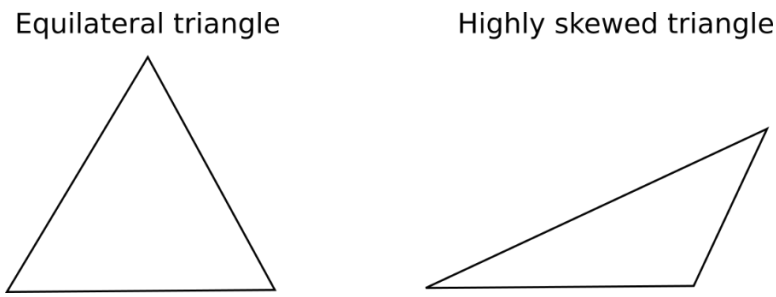

Figure 2.9. *Equilateral and highly skewed triangle*

Setup

Steady-state, conduction between solid-solid and convection and radiation between fluid-solid interfaces is enabled in the domain. Heat transfer in the model domain is enabled by activating the energy equation in the setup. Double-sided walls (walls and their shadows) at solid-solid and fluid-solid interfaces were created to enable heat exchange between the fluid and solid subdomains by thermally coupling the interfaces without assigning temperature, heat transfer coefficient, or other boundary conditions.

The solver type is segregated and pressure-based. Gravitational acceleration is enabled in the domain and set in negative *x*-direction to 9.8 m/s. Standard k-epsilon model was chosen as turbulence model for its robustness, economy, and reasonable accuracy. The model adds two additional PDEs to the system of equations: turbulent kinetic energy equation, k, and the equation for the dissipation rate of turbulent kinetic energy, ε.

Velocity inlet (point 1, Figure 2.4 (a)) and outflow (point 4, Figure 2.4 (a)) were set at the inlet and outlet boundary conditions, respectively. The inlet velocity was calculated in MATLAB using the inlet mass flow rate:

$$v_{in} = \frac{\dot{m}}{A_{inlet}\rho} \tag{2.13}$$

where A_{inlet} is the cross-sectional area of the inlet tube and ρ is the density of the refrigerant at the inlet condition. The path of the refrigerant was modeled to be identical to the one portrayed in Figure 2.4. Outflow boundary condition is used when the details of the flow velocity and pressure are unknown prior to the solution of the flow problem. In other words, no conditions at the outlet are predefined, instead Fluent extrapolates the required information from the interior. Operating pressure of the domain is set at atmospheric pressure, $P_{atm} = 101325\ Pa$, and the operating temperature is the ambient air temperature.

Refrigerant, air, and engine oil are materials used in fluid domains, and steel is the material set in solid domains (internal components and compressor shell). Boussinesq approximation was applied for air density. Refrigerant fluid properties, thermal conductivity, specific heat, dynamic viscosity, and density are assumed to be constant. Thus, the model assumes that the refrigerant is at constant pressure and density. Refrigerant properties are taken at inlet conditions.

Engine oil is defined as a "solid" and fluid material. A thin oil layer considered to be in a solid state is modeled between the liquid oil (oil sump at the bottom, Figure 2.4) and the refrigerant interface, in order to model heat transfer between oil sump and the refrigerant on the bottom, as shown in Figure 2.10. Oil in solid state is assumed to have similar properties as oil in liquid state. This approximation is justified due to the high viscosity of oil. The velocity of the oil sump was assigned as zero in *x*, *y*, and *z* direction.

Oil sump and top of the crankshaft temperatures are set as constant and calculated from a multivariate correlation for oil temperature, as listed below:

$$T_{oil} = 0.28T_{out} + 0.32T_{in} + 9.8 \qquad (2.14)$$

where T_{in} and T_{out} are refrigerant temperatures at compressor inlet and outlet.

The correlation was derived from experimental data over a range of operating conditions, where the difference between condensation and evaporation temperatures varied from 25 to 60 °C. Each operating point was tested at three compressor speeds: 30, 60, and 90 rps. Ambient temperatures were set to 10 and 25 °C.

Volumetric and surface heat fluxes were added to the computational domain. Surface heat flux was assigned as a boundary condition on the rotor top plate, which is equal to $\dot{Q}_{suc}$ calculated from Eq. (**2.2**).

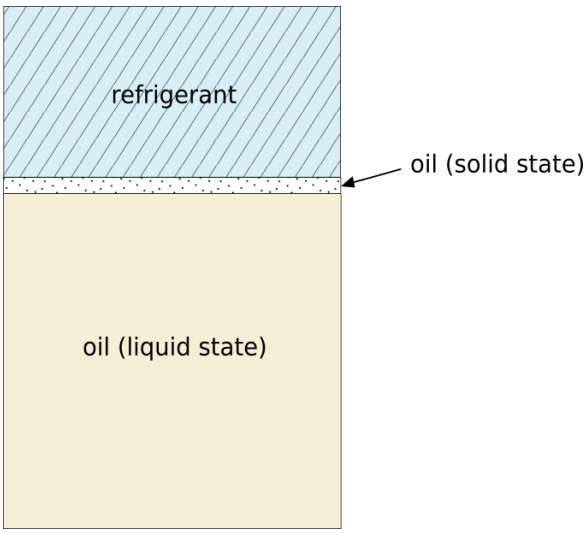

Figure 2.10. *Thin layer of oil in solid phase between refrigerant and oil sump in liquid state*

The CFD model performs a thermal analysis exclusively, and, therefore, no compression is assumed to take place in this part of the model (second step). To represent an increase in temperature from T_{suc} and T_{dis}, temperatures of the refrigerant at suction and discharge, respectively, due to compression and non-isentropic heat release, a heat flux is introduced in the compression chamber, $\dot{Q}_{comp-cham}$, as depicted in Figure 2.11. Suction temperature was calculated from the suction enthalpy in Eq. (**2.6**)

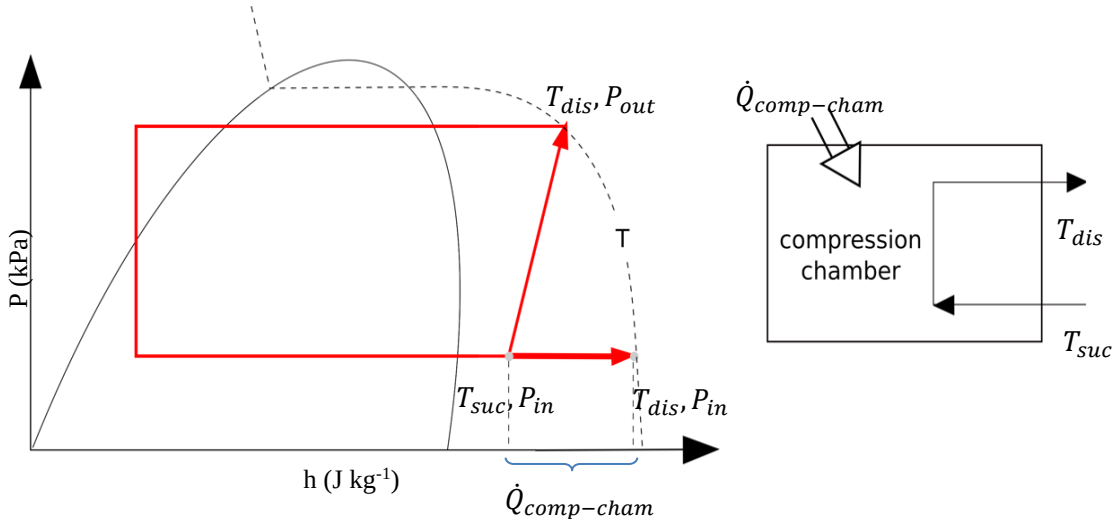

Figure 2.11. *Required heat to reach T_{dis} (temperature of the compressed fluid at discharge)*

Besides refrigerant and oil fluid domains, there is a domain of air that surrounds the compressor. The walls of this domain are set as constant, isothermal wall boundary condition, to represent the ambient temperature surrounding the compressor, T_{amb}. Heat is transferred from compressor shell to ambient air by natural convection and radiation. As mentioned earlier Boussinesq approximation was configured for air density. Boussinesq approximation was chosen due to its ability to reduce the nonlinearity of the model and the number of iterations required for convergence, thus lower computational costs. The approximation implies that the density variations are small and density has no effect on the flow field. In other words, air density is assumed to give rise only to buoyancy forces – density variation is important in the buoyance term of N-S equations. Otherwise in the equations, the density is assumed to be constant. The emissivity of solid components was set as 1 and P1 radiation model was selected. Such radiation model accounts for absorption, scattering, and emissivity in the domain.

Solution was initialized from the inlet boundary condition. In the solution methods menu, the pressure-velocity coupling method was set to SIMPLE, which is an algorithm that is appropriate for steady-state calculations. The gradient was set to Least Square Based and pressure as *standard* in the spatial digitalization. The upwinding of momentum, energy, turbulent kinetic energy and turbulent dissipation rate were set as first order upwind scheme. The convergence criteria were the scaled residuals RMS errors, heat flux and mass flow rate imbalances (<1 %), and the physical nature of the results.

2.2.2.3 Compressor thermal network analysis

The final step of the model involves a network analysis of energy transfer equations between solid-fluid interfaces by convection. The goal of the TNW analysis is to verify that the heat, $\dot{Q}_{comp}$, calculated from Eq. (**2.1**) equals to the net heat dissipated from compressor components:

$$\dot{Q}_{comp} = \dot{Q}_{rotor} + \dot{Q}_{stator} + \dot{Q}_{crank} + \dot{Q}_{comp-cham} \qquad (2.15)$$

The total heat flux of each component is the sum of all heat fluxes of individual surfaces that constitute the component. For instance, heat transferred from the rotor to the surroundings is the sum of heat fluxes between the fluid and rotor surfaces in contact with the fluid. If heat released due to an imperfect compression process, $\dot{Q}_{comp}$, obtained from Eq. (**2.1**) is equal to the heat released by the compressor components obtained from Eq.(2.15), the model converged. If not, more boundary conditions may be assigned in CFD model to guide the differential step more effectively, until convergence in step 3 is achieved.

In order to obtain the net energy released by components, temperatures of the solid components and the surrounding fluid, as well as the refrigerant velocities in proximity to the solid components must be known. These values are obtained from the CFD model. Consequently, using this information, convective heat transfer coefficients are evaluated. Nusselt number correlations for different flow regimes and geometries were taken from the literature. Correlations for internal and external flows for horizontal and vertical, rotating and static plates and cylinders were considered. The relation between Nusselt number and convective heat transfer coefficient is:

$$Nu_x = h_x x / k \tag{2.16}$$

where x is the characteristic length, which depends on the geometry of the object and flow characteristics. It can be a diameter, radius, or length, k is the thermal conductivity of the fluid, and h_x is the convective heat transfer coefficient (Incropera & DeWitt, 2002).

Fluid thermal properties and convective heat transfer coefficients were evaluated at mean film temperatures obtained from the following equation (Incropera & DeWitt, 2002):

$$T_{film} = \frac{T_s + T_r}{2} \tag{2.17}$$

where T_s is component surface temperature and T_r is the refrigerant gas temperature.

Heat transfer from the rotor is the heat flux from the top disk of the rotor. Similarly, total heat transfer from the stator is equal to the heat flux from the top disk of the stator. Heat transfer from the crankshaft equals to the heat released from the top lateral side of the shaft (above the motor assembly). Only the top surfaces of these components are considered in the thermal analysis since this is where heat exchange between suction gas and these components is assumed to occur.

There is a narrow rotor-stator and stator-shell gap, where heat exchange occurs as well. However, according to compressor manufacturers, the gaps are extremely narrow and a very small portion of the fluid (oil and refrigerant) is assumed to pass in such gaps. Due to this, it can be assumed that the fluid passes directly from the inlet port to the compression chamber, and there is only a small portion of fluid at the bottom of the compressor, in the cavity between the shell bottom and crankshaft and motor assembly. The fluid can be assumed to be stagnant and inert – no thermal interaction between fluid and solid components. For this reason, stator-rotor and stator-shell gaps are not modeled from a thermal point of view in this part of the model (step 3). Similarly, heat

transfer from the bottom of the motor assembly and the crankcase is assumed to be zero.

If the stator-rotor and stator-shell gaps are significant in size, heat exchange from these parts cannot be neglected from the analysis. Appendix C presents the correlation found in literature that are appropriate for quantifying the heat exchange between two concentric cylinders (rotor-stator gap), where one cylinder represents a rotor – hotter and rotating cylinder, and another one represents the stator – cooler and static concentric cylinder, as well as correlation found in literature for two static concentric cylinders (stator-shell gap).

Heat transfer from the compression chamber is expressed in the following equation:

$$\dot{Q}_{comp-cham} = \dot{Q}_{cha-cyl} + \dot{Q}_{cha-top} + \dot{Q}_{cha-bot} \qquad (2.18)$$

where $\dot{Q}_{cha-cyl}$ is the heat absorbed by the lateral walls inside the compression chamber, $\dot{Q}_{cha-top}$ is the is the heat absorbed by the top circular plate inside the compression chamber, and $\dot{Q}_{cha-bot}$ is the heat absorbed by the bottom circular plate of the compression chamber, as illustrated in Figure 2.12.

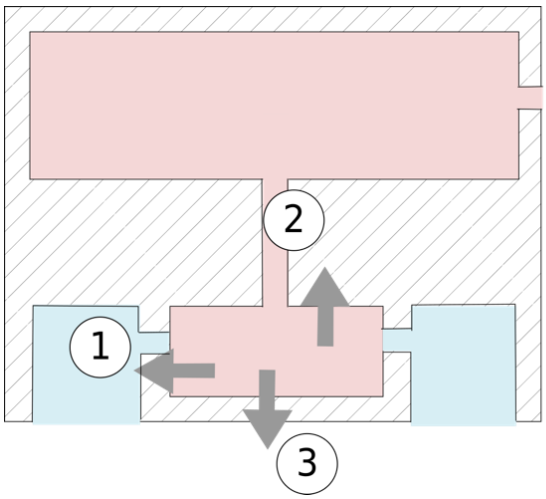

1: $\dot{Q}_{cha-cyl}$
2: $\dot{Q}_{cha-top}$
3: $\dot{Q}_{cha-bot}$

Figure 2.12. *Heat fluxes released from the fluid to compression chamber*

As mentioned earlier, oil can be found in many places inside the compressor. Practically, oil forms a thin film on the majority of the interior surfaces. At the bottom of the compressor, where the fluid is assumed to be stagnant, refrigerant is mixed with droplets of oil, and beneath that is an oil sump (Figure 2.4). Simplifications made in the model that concern oil are discussed in more detail in Subsection 3.3.1.

Since most of the flow over the interior compressor components was assumed to be forced, (average flow velocity more than 2 m/s), a dimensionless Reynolds number is required to estimate whether the flow is in a turbulent or laminar regime:

$$Re_x = \frac{vx}{\upsilon} \tag{2.19}$$

where ν is the kinematic viscosity and v is the flow velocity (Incropera & DeWitt, 2002).

Nusselt number correlation for forced convection for turbulent and external flows over a flat round plate is presented in the following equation (Padet, 2008):

$$\overline{Nu}_D = 0.035 Re_D^{0.8} Pr^{1/3} \tag{2.20}$$

where Pr is the Prandtl number evaluated from the mean film temperature and D is the surface diameter. Such correlations were used for top and bottom surfaces of the rotor, stator, and compression chamber.

Churchill & Bernstein (1977) suggested a Nusselt number correlations for forced and external convection across vertical cylindrical surfaces, such as the rotor, stator, crankcase, and compression chamber cylinder walls, presented in the following set of equations:

$$Nu_D = 0.3 + \frac{0.62 Re_D^{1/2} Pr^{1/3}}{\left[1 + \left(\frac{0.4}{Pr}\right)^{2/3}\right]^{1/4}} \left[1 + \left(\frac{Re_D}{282000}\right)^{5/8}\right]^{4/5} \qquad (4 \cdot 10^5 < Re_D < 5 \cdot 10^6) \tag{2.21}$$

or

$$Nu_D = 0.3 + \frac{0.62 Re_D^{1/2} Pr^{1/3}}{\left[1 + \left(\frac{0.4}{Pr}\right)^{2/3}\right]^{1/4}} \left[1 + \left(\frac{Re_D}{282000}\right)^{1/2}\right] \qquad (2 \cdot 10^4 < Re_D < 4 \cdot 10^5) \tag{2.22}$$

or

$$Nu_D = 0.3 + \frac{0.62 Re_D^{1/2} Pr^{1/3}}{\left[1 + \left(\frac{0.4}{Pr}\right)^{2/3}\right]^{1/4}} \qquad (Re_D < 10^4) \tag{2.23}$$

Gnielinski (1976) recommended the following Nusselt number correlation for static vertical cylinder for an internal flow:

$$Nu_D = \frac{\left(\frac{f}{8}\right)(Re_D - 1000)Pr}{1 + 12.7\left(\frac{f}{8}\right)^{1/2}(Pr^{2/3} - 1)} \quad (Pr \geq 0.5, 3 \cdot 10^3 \leq Re_D \leq 5 \cdot 10^6) \qquad (2.24)$$

where f is the internal friction for a smooth wall obtained from a formula suggested by Petukhov (1970):

$$f = (0.790.\, lnRe_D - 1.64)^2 \qquad (2.25)$$

Such correlation is used to estimate heat transfer inside the compression chamber.

As seen in Figure 2.13 (top), fluid enters the compression chamber from the four entrances and exits from the discharge located on the top of the chamber. However, there is no heat transfer correlation available directly from the literature for this type of flow configuration, hence, Eq. (**2.3**) was used. The hydraulic diameter, D_h, that is typically a pipe diameter in such correlation ($D_{h,2}$ in Figure 2.13) was assumed to be equal to the height of the compression chamber inner wall ($D_{h,1}$ in Figure 2.13). The heat transfer area was considered to be the total inner area of the compression chamber: top, bottom, and lateral surfaces.

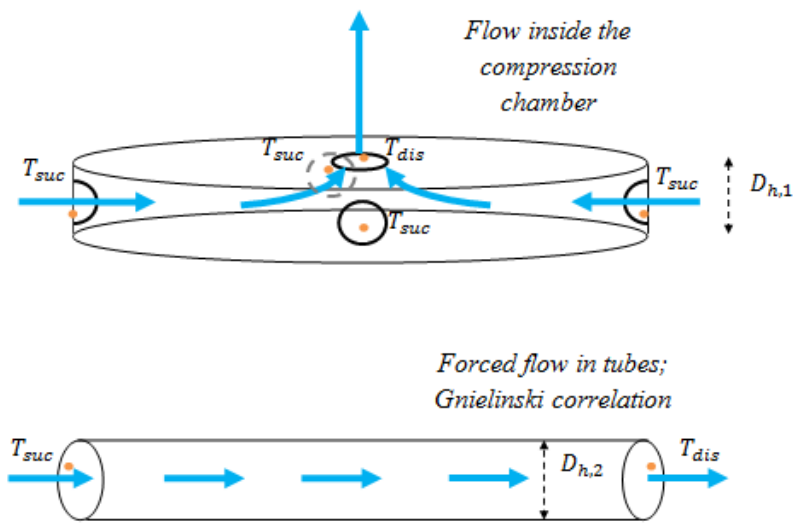

Figure 2.13. *Flow inside the compression chamber (above) is approximated as the flow inside a pipe (below)*

For a rotating disk heated from the bottom or cooled from the top, *i.e.* rotor top surface, in laminar flow the following Nusselt number correlation can be used (Incropera & DeWitt, 2002):

$$Nu_D = 0.33 Re_{\Omega}^{1/2} \qquad (10^3 \leq Re_{\Omega} \leq 2 \cdot 10^5) \qquad (2.26)$$

where Re_{Ω} is the Reynolds number for rotating surface calculated using the following formula:

$$Re_{\Omega} = \frac{\Omega D^2}{\upsilon} \qquad (2.27)$$

where ν is the kinematic viscosity, Ω is the angular velocity, and D is the diameter of the body (characteristic length).

Kreith *et al*. (1963) recommended Nusselt number correlation for a rotating cylinder used to calculate the heat transfer from top lateral part of the crankshaft is listed below:

$$Nu_D = 0.133 Re_{\Omega}^{2/3} Pr^{1/3} \qquad (Re_{\Omega} < 4.3 \cdot 10^5) \qquad (2.28)$$

where the cylinder diameter is the characteristic length, D. This correlation takes into account only the rotational flow (vortex) and, hence, the angular velocity is the characteristic velocity of the fluid used to calculate Reynolds numbers. Fluid that flows past the crankshaft also has an axial velocity, since it flows towards the compression chamber. However, in order to keep the thermal analysis simplified, it is assumed that the fluid surrounding the crankcase has only an angular velocity and no axial flow takes place.

If the deviation between the values obtained from Eq. (**2.1**) (step one) and Eq. (**2.15**) (step three) are within the 10 % range, then the model is considered to be converged. If not, the second step of the model must be guided more efficiently, for instance, assigning more boundary conditions might be necessary.

2.2.3 Rotary

2.2.3.1 Thermodynamic cycle analysis

The heat absorbed by the rotary compression chamber (components) is assumed to be equal to the heat released by the fluid due to a non-isentropic compression (thermodynamic losses), as depicted in the following equation:

$$\dot{Q}_{comp} = \dot{Q}_{non-is} = \dot{W}_e - \dot{W}_{is} \qquad (2.29)$$

where $\dot{W}_{is}$ is calculated as described in Subsection 2.2.2.1 in Eq. (**2.3**). The heat released by the fluid is calculated in the third step of the model, the thermal network analysis, where $\dot{Q}_{comp}$ is calculated as the heat transfer from the fluid to the walls of the compression chamber. As in the case of scroll model, the two values are compared to verify the validity of the CFD model.

The main difference between this step in rotary and scroll compressor models is that there is no gas superheat in rotary compressors: the gas passing by the motor assembly is hotter than the motor surfaces and releases thermal energy instead, since the compression chamber is located before the motor. Therefore, calculating the motor heat is only required for the second step (CFD part) of the model in order to assign it as surface heat flux boundary condition.

2.2.3.2 Detailed thermophysical flow analysis

Generally, this step of the model is quite similar to the one described in Subsection 2.2.2.2 for scroll compressors in terms of geometry, mesh, and setup configurations. The main difference is the component layout.

Geometry

As in the scroll compressor model, the domain geometry of the CFD model is decomposed into solid and fluid zones: sub domains are oil continuum (the bottom of the compressor cylinder), discrete refrigerant fluid zones, surrounding air continuum, and solid zones bounded by simplified geometrical boundaries of the components. Figure 2.14 portrays the computational domain in Designer Modeler. The computational domain consists of compressor shell, crankshaft, fluid gap between rotor and stator, suction and discharge ports, compression chamber, and cylinder inlet and outlet cavities through which the refrigerant enters and exits the domain. The computational domain in CFD is coherent with the TNW programmed in MATLAB (step 3, integral part of the model). The crankcase and rotor are considered to be stationary, unlike in the TNW, where the parts in question are considered to be rotating.

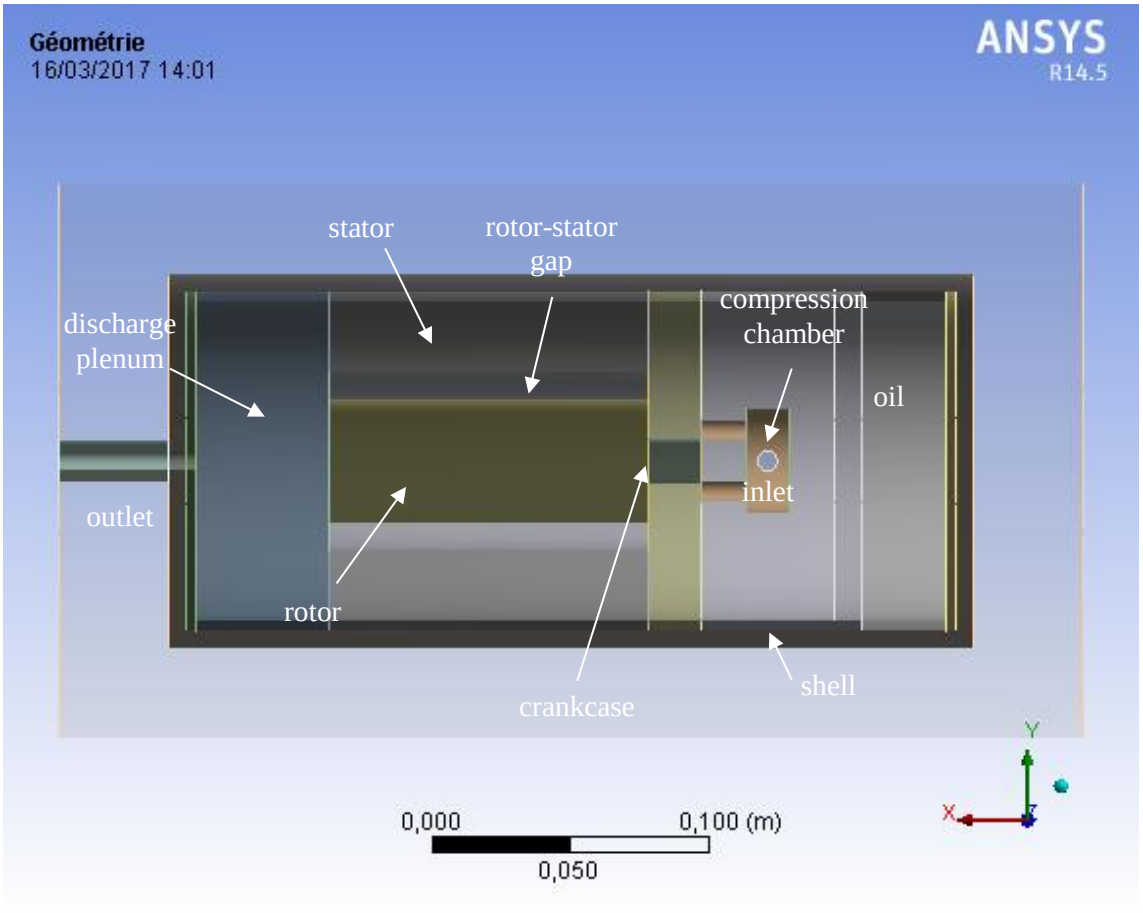

Figure 2.14. *Computational domian of rotary compressor in ANSYS Workbench pre-processing tool, Design Modeler*

Dimension parameterization was enabled in the geometry ensuring that the dimensions of the components can be easily changed when necessary.

A supplementary layer on the compressor shell can be seen, as highlighted in green in Figure 2.15. Modifying the material of this part, for instance, to wool-fiber, can represent an insulation layer. In that case the wall boundary types are set to double-sided wall (*wall* and *wall-shadow*). However, if no insulation layer is desired, this part of the shell can be set to steel material, in which case the wall boundaries must be changed from *wall* to *interior*. The thickness of the insulation layer can be adjusted in the parametrization settings.

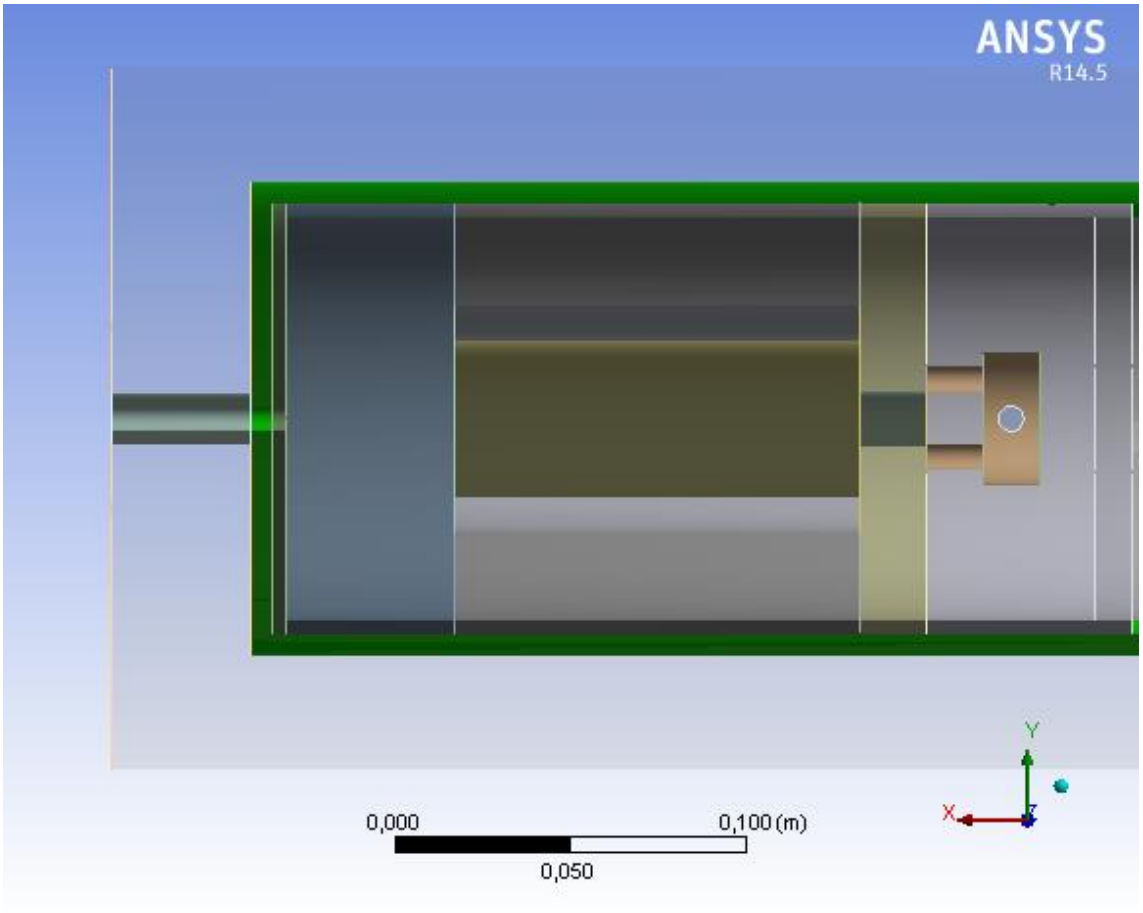

Figure 2.15. *Insulation layer high-lighted in green around the exterior shell of the compressor*

Mesh

The domain mesh consists of $2.3 \cdot 10^6$ tetrahedrons, hexahedrons, wedges, and pyramids. The mesh in rotary domain is a hybrid mesh; consists of portions of structured grid (stator and oil sump) and unstructured grid (rest of the domain).

Meshed domain is presented in Figure 2.16. Similar to scroll compressor domain, denser mesh is imposed in narrow passages and regions with more significant curvature, such as small cylindrical cavities (compressor inlet and outlet, suction and discharge). The average orthogonal quality of the mesh is 0.86. The maximum aspect ratio is 21.0 and the average is 1.86. The maximum skewness is 0.98 of one element. The average skewness in the scroll mesh was 0.23. The mesh of rotary domain is of good quality.

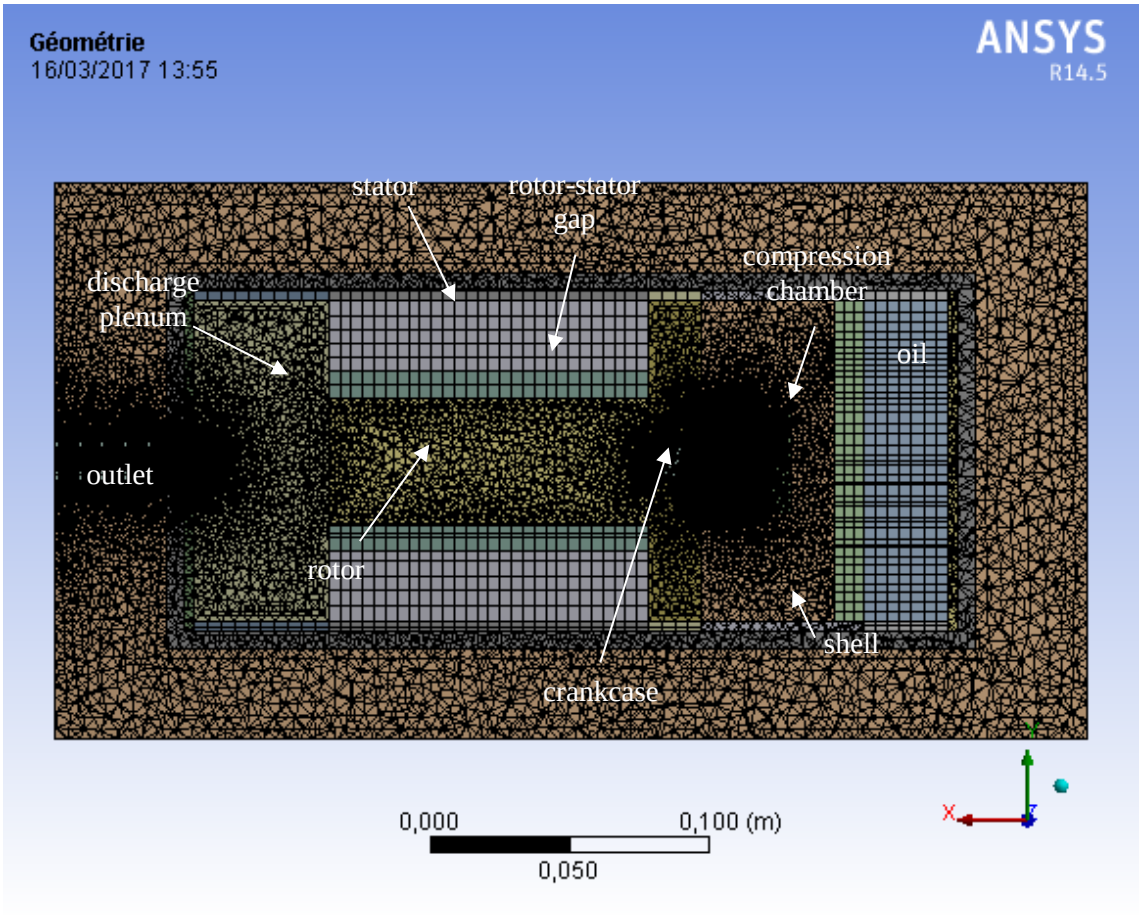

Figure 2.16. *Rotary compressor mesh in ANSYS Workbench pre-processing tool, Mechanical*

Setup

The configuration of the CFD model for rotary compressor is identical to the CFD setup of the scroll model. For instance, steady-state, conduction between solid-solid and convection and radiation between fluid-solid interfaces is enabled in the domain, solver type is segregated and pressure-based, gravitational acceleration is enabled in the model, and standard k-epsilon model is chosen as turbulence model. Similarly, velocity inlet, and outflow were set at inlet (point 1, Figure 2.4 (b)) and outlet (point 3, Figure 2.4 (b)) boundary conditions. The path of the refrigerant was modeled identically as the one portrayed in Figure 2.4 (b). Materials used for the solid and fluid domains and their properties were identical as the ones in the scroll model. Boussinesq approximation was also used to model natural convection. Thin oil layer in solid state was modeled as in scroll model to divide the two fluid interfaces, oil and refrigerant.

The emissivity of internal components was set to be equal to 1 and P1 model was chosen as the radiation model, as in the scroll model setup.

Oil sump and top of the crankshaft temperatures are set as constant and calculated from a correlation for oil temperature, as listed below:

$$T_{oil} = -0.0235T_{out}^2 + 4.045T_{out} - 96.699 \qquad (2.30)$$

Unlike in the case of scroll compressors, a parametric analysis showed that oil temperature is primarily dependent on condensation temperature. The correlation was derived from experimental data over a range of operating conditions, identical to the ones considered in scroll.

Temperature measurements from the experimental tests showed that the exterior wall temperature at the motor level is hotter. The CFD model does not model the stator-shell gap, since imposing a mesh in such a confined space is challenging, considering that the aim was to keep the number of mesh elements and, thus, the calculation time to a minimum. In order to represent working fluid passing through this narrow passage, constant temperature, T_{dis}, was set as a boundary condition of the wall between the shell and stator.

Volumetric and surface heat fluxes were added to the computational domain. Similar to the scroll model, second step of the rotary model performs a thermal analysis exclusively and heat flux required to represent an increase in temperature from T_{suc} to T_{dis} is calculated as depicted in Figure 2.11. Motor losses were assigned as surface heat flux boundary condition, calculated from Eq. (**2.2**).

2.2.3.3 Compressor thermal network analysis

As mentioned above in Subsection 2.2.2.3, the heat released by the fluid to the solid components due to thermodynamic losses during the compression process is equal to the heat absorbed by the solid parts of the compression chamber, as listed below (identical to Eq. (**2.18**):

$$\dot{Q}_{comp} = \dot{Q}_{comp-cham} = \dot{Q}_{cha-cyl} + \dot{Q}_{cha-top} + \dot{Q}_{cha-bot} \qquad (2.31)$$

The flow of refrigerant within the compression chamber was approximated as the flow of fluid in a pipe, depicted in Figure 2.13.

If the deviation between the values obtained from Eq. (**2.29**) (step one) and Eq. (**2.31**) (step three) are within the 10 % range, then the model is considered to be converged.

If not, the second step of the model must be guided more efficiently, for instance, assigning more boundary conditions might be necessary.

2.3 Conclusions

Tran *et al.* (2013) established that compressor heat losses contribute significantly to the relative uncertainty of the performance assessment method. Therefore, in order to improve the performance assessment method, the estimation of compressor heat losses on-field must be more accurate. One of the main sources of uncertainty in the current method used to estimate compressor heat losses, presented in Eq. (**1.19**), is the fact that the compressor shell was assumed to be isothermal and equal to the refrigerant discharge temperature. For this reason, the first step in improving the compressor heat loss model was to investigate the thermal behavior of the rotary and compressor shell in various operating conditions.

In order to establish the temperature distribution of the compressor shell, internal compressor components must be modeled, *i.e.* the computational domain of the model is the entire compressor. However, thermal analysis of compressors is a challenging task due to complex interior geometry that hinders simplifications. A literature review led us to choose a hybrid modeling approach. Such approach combines integral and differential formulations. It is more flexible in terms of its applicability to various compressor types and less computationally expensive than differential models, and it yields more accurate results than integral models.

Two hybrid models were developed; for scroll and rotary compressors. The calculation procedure in the models is divided in three fundamental steps: thermodynamic cycle analysis, detailed thermophysical flow analysis executed with the aid of a CFD program, and a compressor thermal network analysis.

The calculation procedure of the numerical models is the following:

1. **The first step** of the model analyzes the thermodynamic compression cycle in order to evaluate the initial and boundary conditions used in integral and differential parts of the model, steps two and three, respectively.

2. **The second step** of the model uses a CFD code to numerically solve a set of governing differential equations. The outcomes of this part of the model are transmitted to the final step of the model in order to perform a TNW analysis that verifies the CFD simulations.

3. **The third step** of the model involves a network of energy transfer equations between the solid-fluid interfaces by convection. The goal is to verify that the

value of $\dot{Q}_{comp}$ calculated in the first step from Eq. (**2.1**) and (**2.29**), for scroll and rotary compressor, respectively, equals to the net heat dissipated/absorbed by the components calculated from Eqs.(**2.15**) and (**2.31**), for scroll and rotary compressor, respectively. If the difference between the two values is less than 10 %, the model is considered converged, and the external and internal thermal profiles (if necessary) can be extracted from the second part (CFD) of the model.

The results obtained from the models presented in Chapter 3 are used to determine which zones contribute most to the heat losses and which location of temperature sensor can be used best to represent the average temperature of the shell or shell zone, presented in Chapter 4.

CHAPTER 3

EXPERIMENTAL VALIDATION OF THE NUMERICAL MODEL

Les températures d'enveloppe des compresseurs scroll et rotary ont été comparées aux températures obtenues sur banc d'essai, pour cinq points de fonctionnement. Nous observons une bonne cohérence entre les valeurs issues du modèle numérique et les valeurs expérimentales, pour les deux types de compresseurs.

Le modèle numérique a montré que l'enveloppe du compresseur rotary est homogène pour tous les points de fonctionnement. Cependant, le compresseur scroll a présenté une forte hausse de température au niveau de la chambre de compression, indiquant que la majeure partie des pertes thermiques provient de la partie haute pression du compresseur.

Les valeurs de température des composants internes ont été extraites du modèle numérique pour le compresseur scroll. Nous observons une bonne cohérence entre ces valeurs et les valeurs expérimentales. Cette information peut être utile pour évaluer la sensibilité des composants à l'endommagement thermique.

Les simplifications introduites dans le modèle numérique, comme par exemple les simplifications liée à la lubrification d'huile et la géométrie de composants, ont une influence sur la précision des modèles numériques. Néanmoins, ces simplifications ont été nécessaires afin de maintenir le modèle flexible pour qu'il puisse rester adapté à différentes configurations géométriques, et afin d'assurer un temps de calcul raisonnable.

3.1 Experimental setup

Numerical results were compared to experimental data obtained from a scroll and rotary compressor test bench in Mitsubishi Heavy Industries (MHI) laboratory, Air-Conditioning & Refrigeration Systems.

Figure 3.1 is a schematic representation of the calorimeter chamber, where scroll and rotary compressors were placed, each at a time. A small fan inside the calorimeter chamber was used to help homogenize the ambient temperature. Depending on the ambient air setting the outlet ambient air was either cooled or chilled by a heat exchanger and later directed by a fan from the heat exchanger to the inlet mesh, on the top of the calorimeter chamber. Ambient temperature was measured at the air inlet.

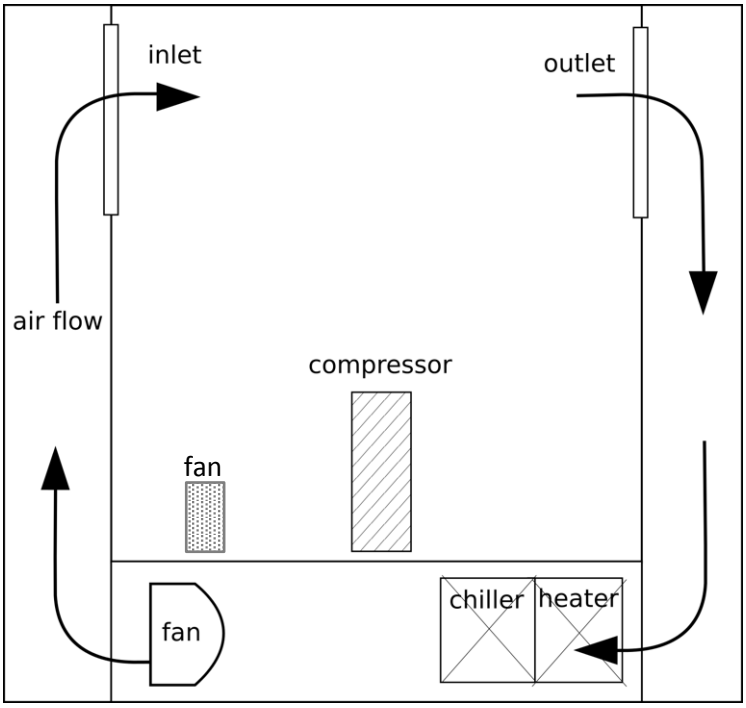

Figure 3.1. *Calorimeter chamber of the scroll and rotary compressor test bench used for experimental validation*

Compressor component layouts used in the experiments was identical to the ones in the numerical model, presented in Figure 2.4 (a) and (b) for scroll and rotary domains, respectively. Compressor dimensions in the numerical models were adapted to the ones tested in the experiments.

The refrigerant fluid used in tests were R407C and R134a in scroll and rotary compressor, respectively. Various operating conditions were tested in order to validate the

numerical models for the two compressor types. Various operating conditions were achieved by varying specific parameters: compressor speed, ambient temperature, inlet and outlet pressures.

In the experimental setup 40 and 42 thermocouples were placed along the compressor shell and on the internal components of scroll and rotary compressors, respectively. The uncertainty of these sensors was 0.6 K. In addition, inlet and outlet pressures were measured with pressure sensors, as well as compressor power input with a wattmeter, and a flow meter was used to measure the refrigerant mass flow rate and oil concentration in the refrigerant circuit using an oil separator.

Thermocouples were placed on the static parts of the motor top and bottom, in close proximity to the stator in order to establish the motor temperature. Similarly, in order to determine the temperature of the crankshaft, thermocouples were placed on the frame located in close proximity to the crankshaft. Also, temperatures of the discharge baffle (bottom of the discharge plenum) were measured, as well as the shell temperature at various locations, and oil temperature at the bottom of the compressor. In the experimental setup rotary compressor had an accumulator tank. Temperature sensors were placed on the exterior shell of this tank. Refrigerant temperature at inlet, outlet, and discharge were measured. In scroll compressors, refrigerant temperature at the compression chamber suction cavity was measured as well.

Measuring points 1-7 and 1-6 for scroll and rotary compressor, respectively, represent the locations of thermocouples along the shell, from the bottom to the top, as depicted in Figure 3.2.

The tested compressors had no insulation layer. Typically, in residential applications, compressors have an insulation layer. However, as mentioned earlier in Subsection 2.2, the numerical model can be easily adapted to integrate an insulation layer around the compressor shell. During the tests, all values were registered in steady operating state, about 10 minutes after startup.

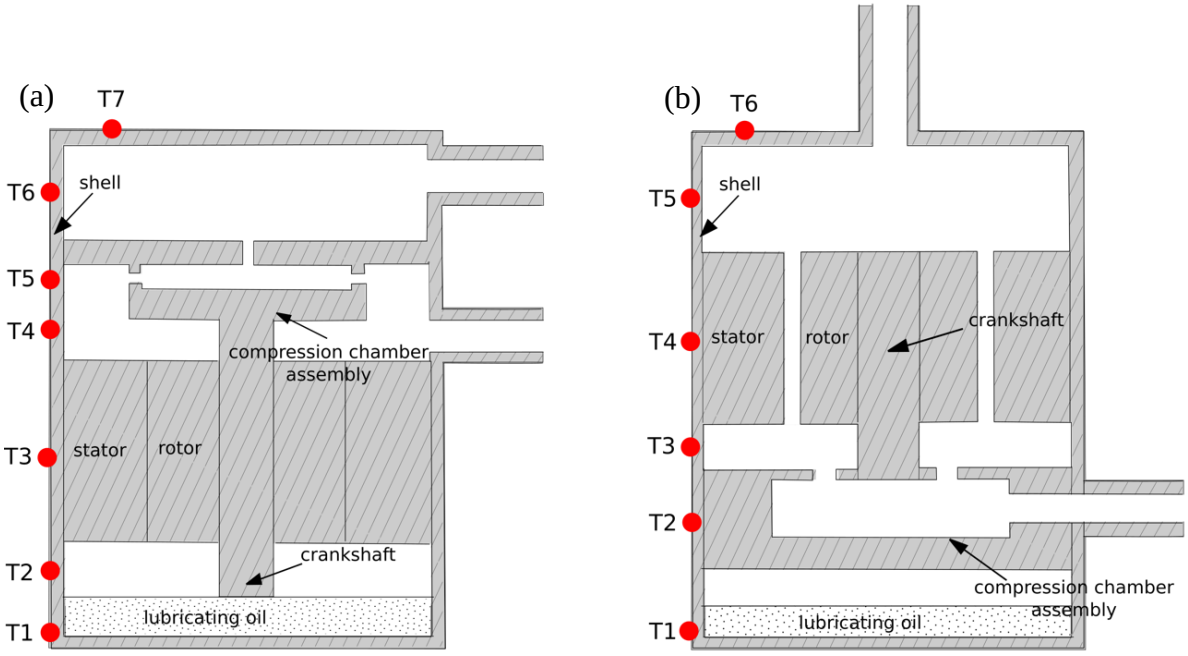

Figure 3.2. *Location of thermocouples on compressor shells of scroll (a) and rotary (b) compressors*

3.2 Comparison of thermal profiles

The numerical models were validated using the results obtained from the experimental test bench in five operating conditions.

In the validation the experimental thermal profiles of scroll and rotary compressor were compared to the temperature values in the corresponding locations extracted from the numerical model. For confidentiality reasons, the temperature values are expressed as dimensionless values.

The operating conditions are listed in Table 3.1.

Table 3.1 *Operating conditions used to obtain experimental results for numerical model validation*

Operating condition	T_{cond} (°C)	T_{evap}(°C)	T_{amb}(°C)	speed (rps)
1	40	0	10	30
2	40	0	10	60
3	60	0	10	30
4	40	15	25	30
5	40	15	25	90

3.2.1 Scroll

Starting from Figure 3.4 to Figure 3.7, numerical and experimental temperatures distributed along the exterior compressor shell are compared in various operating conditions. Measuring points 1-7 represent the locations of thermocouples along the shell, from the bottom to the top (Figure 3.2 (a)).

As mentioned previously, the numerical model consists of three fundamental steps: thermodynamic analysis of the compression cycle, thermophsyical flow analysis (CFD model), and a thermal network analysis. The third step, thermal network analysis, verifies that the results obtained in the second part, CFD model, are reliable. The model was considered globally converged when the $\dot{Q}_{comp}$ value obtained in Eq. (**2.1**) fell within the ±10% range of the $\dot{Q}_{comp}$ value obtained from Eq. (**2.15**). The second step (CFD model) took approximately 4 hours to converge.

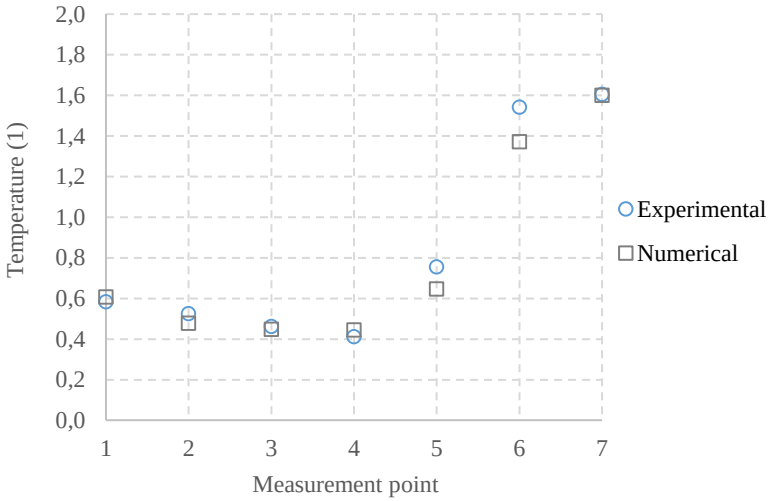

Figure 3.3. *Experimental and numerical shell temperature distributions in scroll compressor at* $\boldsymbol{T_{cond} = 40\ °C}$, $\boldsymbol{T_{evap} = 0\ °C}$, *and* $\boldsymbol{T_{amb} = 10\ °C}$, *30 rps (operating condition 1)*

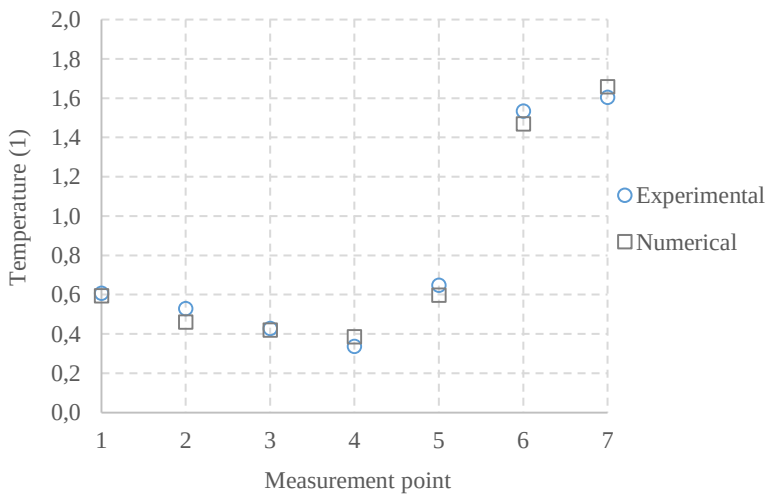

Figure 3.4. *Experimental and numerical shell temperature distributions in scroll compressor at* $\boldsymbol{T_{cond} = 40\ °C}$, $\boldsymbol{T_{evap} = 0\ °C}$, *and* $\boldsymbol{T_{amb} = 10\ °C}$, *60 rps (operating condition 2)*

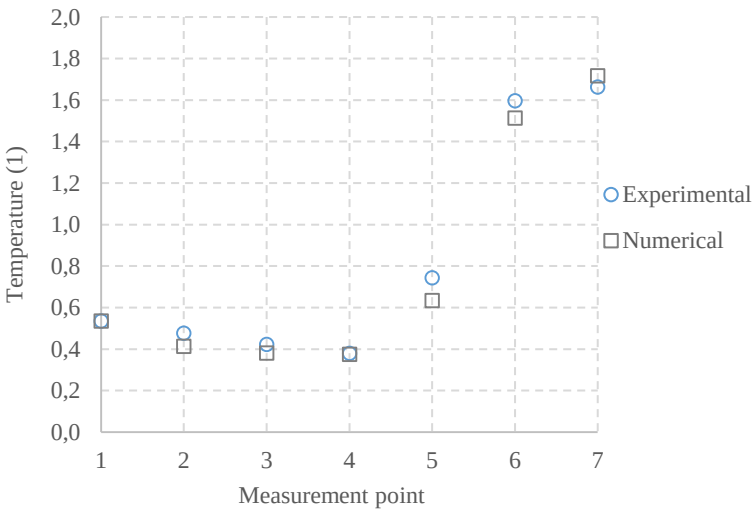

Figure 3.5. *Experimental and numerical shell temperature distributions in scroll compressor at* $\boldsymbol{T_{cond} = 60\ C}$, $\boldsymbol{T_{evap} = 0\ C}$, *and* $\boldsymbol{T_{amb} = 10}$, *30 rps (operating condition 3)*

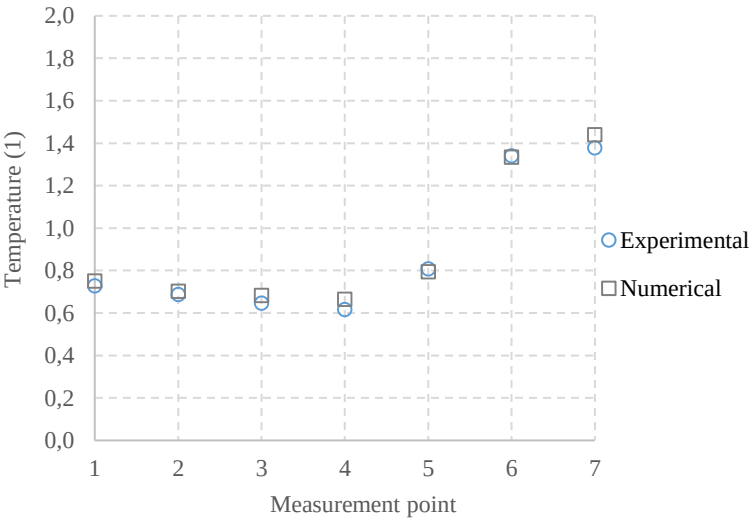

Figure 3.6. *Experimental and numerical shell temperature distributions in scroll compressor at* $\boldsymbol{T_{cond} = 40\ °C}$, $\boldsymbol{T_{evap} = 15\ °C}$, *and* $\boldsymbol{T_{amb} = 25\ °C}$, *30 rps (operating condition 4)*

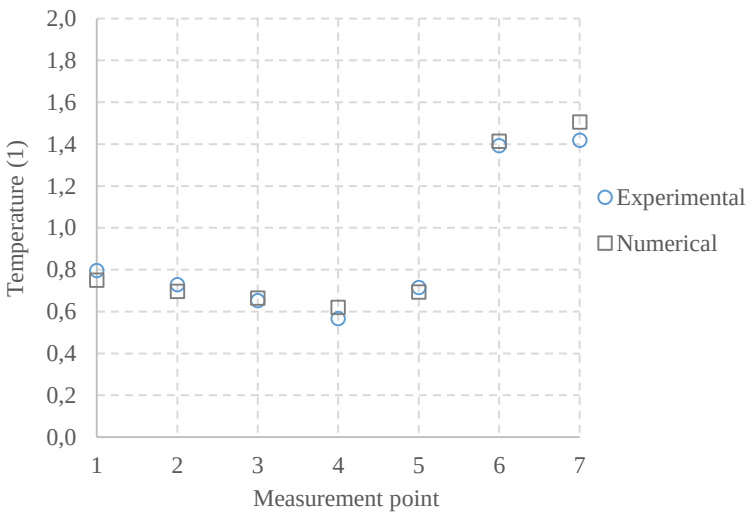

Figure 3.7. *Experimental and numerical shell temperature distributions in scroll compressor at* $\boldsymbol{T_{cond} = 40\ °C}$, $\boldsymbol{T_{evap} = 15\ °C}$, *and* $\boldsymbol{T_{amb} = 25\ °C}$, *90 rps (operating condition 5)*

The dimensionless RMS errors of external profiles are depicted in Table 3.2 at corresponding operating conditions.

Table 3.2 *Dimensionless RMS errors of external profiles in different operating conditions in scroll compressor*

Operating condition	1	2	3	4	5
RMSE (1)	0.080	0.049	0.063	0.035	0.046

Numerical and experimental temperature values of the internal components are compared in Figure 3.8, Figure 3.9, and Figure 3.10. Only few operating conditions are presented since internal temperature distribution was not of primary interest in the scope of this work.

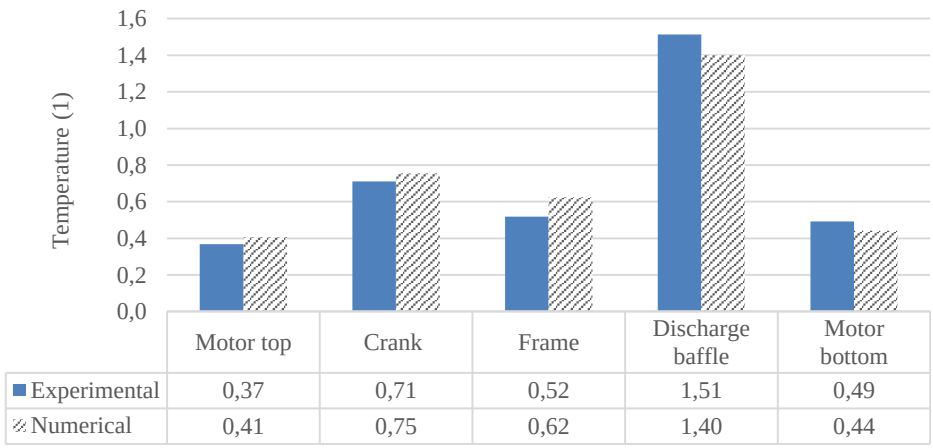

Figure 3.8. *Experimental and numerical component temperatures in scroll compressor at* $\boldsymbol{T_{cond} = 40\ °C}$, $\boldsymbol{T_{evap} = 0\ °C}$, *and* $\boldsymbol{T_{amb} = 10\ °C}$, *30 rps (operating condition 1)*

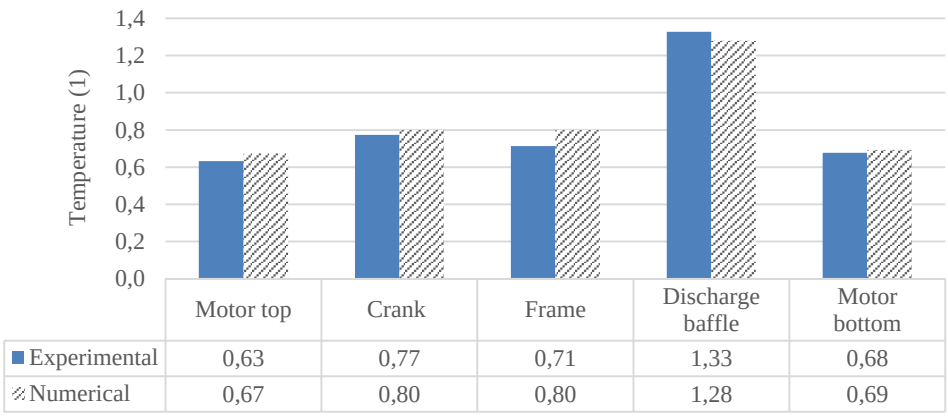

Figure 3.9. *Experimental and numerical component temperatures in scroll compressor at* $\boldsymbol{T_{cond} = 40\ °C}$, $\boldsymbol{T_{evap} = 15\ °C}$, *and* $\boldsymbol{T_{amb} = 25\ °C}$, *30 rps (operating condition 4)*

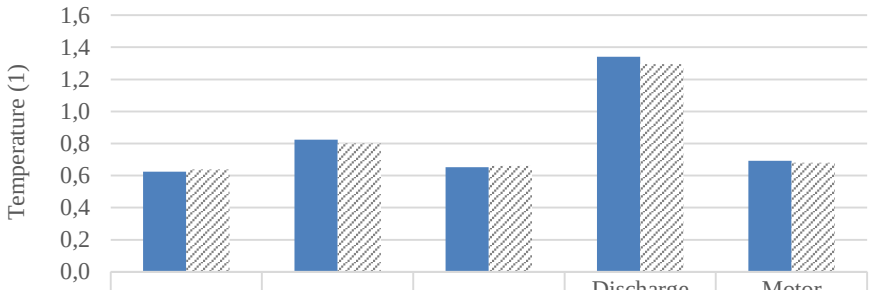

	Motor top	Crank	Frame	Discharge baffle	Motor bottom
Experimental	0,62	0,82	0,65	1,34	0,69
Numerical	0,64	0,80	0,66	1,30	0,68

Figure 3.10. *Experimental and numerical component temperatures in scroll compressor at* $\boldsymbol{T_{cond} = 40\ °C}$, $\boldsymbol{T_{evap} = 15\ °C}$, *and* $\boldsymbol{T_{amb} = 25\ °C}$, *90 rps (operating condition 5)*

3.2.2 Rotary

Numerical and experimental temperature values of external rotary shell expressed in dimensionless values for confidentiality reasons were compared starting from Figure 3.11 to Figure 3.15 in the same operating conditions as in scroll (Table 3.1). Measuring points 1-6 represent the locations of thermocouples along the shell, from the bottom to the top (Figure 3.2 (b)).

The second step (CFD model) took approximately 2 hours to converge, and for the third step to converge, the value obtained in Eq. (**2.29**) had to fall within the ±10% range of the value obtained from Eq. (**2.31**). Less time was required for rotary model to converge due to smaller number of mesh elements and the presence of structured grid in some subdomains.

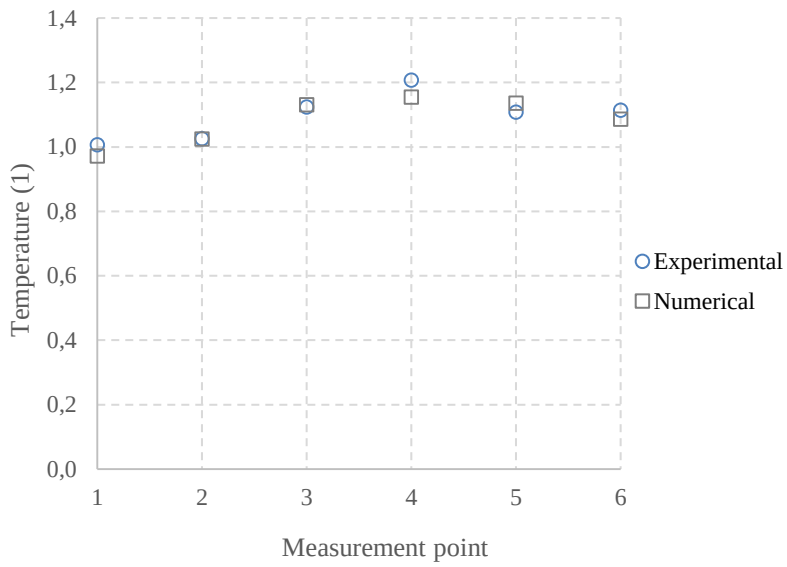

Figure 3.11. *Experimental and numerical shell temperature distributions in rotary compressor at* $\boldsymbol{T_{cond} = 40\ °C}$, $\boldsymbol{T_{evap} = 0\ °C}$, *and* $\boldsymbol{T_{amb} = 10\ °C}$, *30 rps (operating condition 1)*

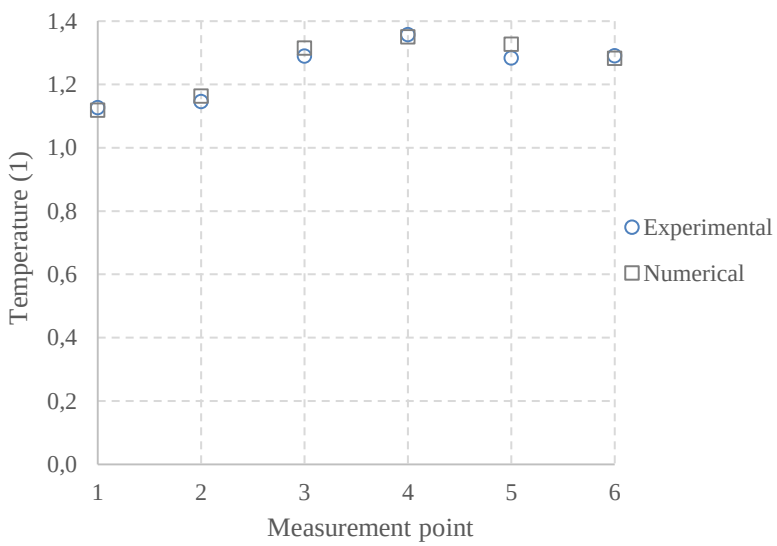

Figure 3.12. *Experimental and numerical shell temperature distributions in rotary compressor at* $\boldsymbol{T_{cond} = 40\ °C}$, $\boldsymbol{T_{evap} = 0\ °C}$, *and* $\boldsymbol{T_{amb} = 10\ °C}$, *60 rps (operating condition 2)*

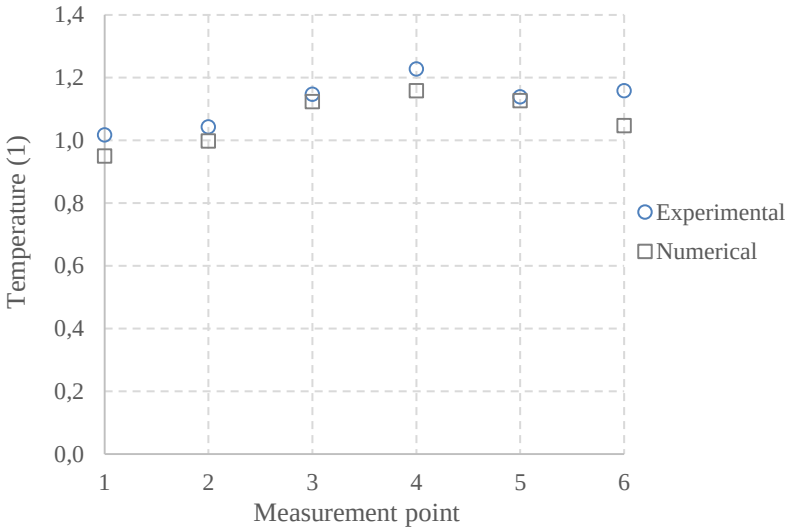

Figure 3.13. *Experimental and numerical shell temperature distributions in rotary compressor at* $\boldsymbol{T_{cond} = 60\ °C}$, $\boldsymbol{T_{evap} = 0\ °C}$, *and* $\boldsymbol{T_{amb} = 10\ °C}$, *30 rps (operating condition 3)*

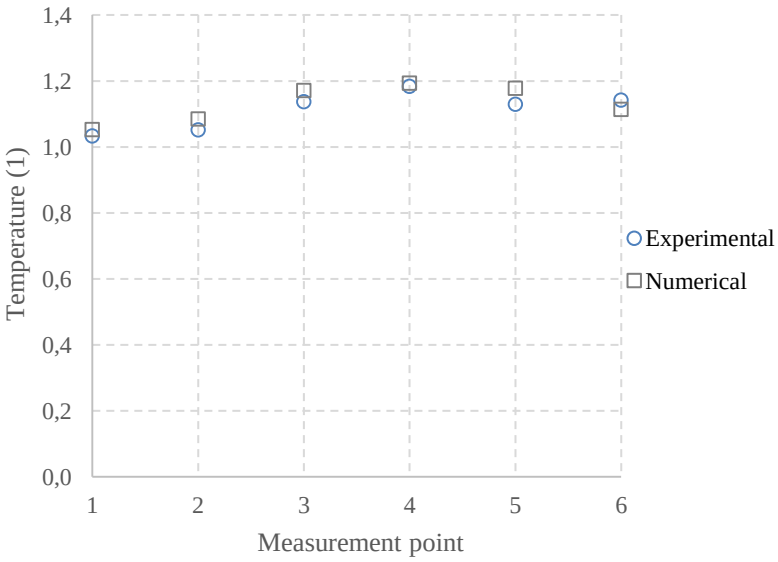

Figure 3.14. *Experimental and numerical shell temperature distributions in rotary compressor at* $\boldsymbol{T_{cond} = 40\ °C}$, $\boldsymbol{T_{evap} = 15\ °C}$, *and* $\boldsymbol{T_{amb} = 25\ °C}$, *30 rps (operating condition 4)*

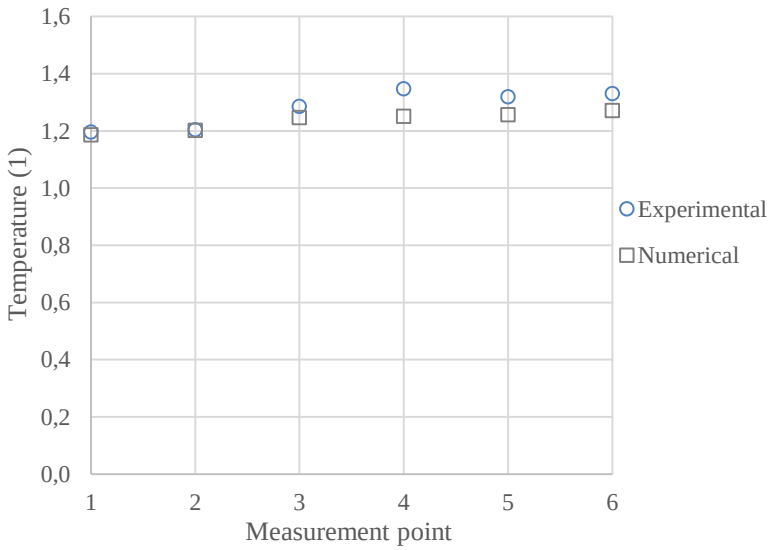

Figure 3.15. *Experimental and numerical shell temperature distribution in rotary compressor at* $\boldsymbol{T_{cond} = 40\ °C}$, $\boldsymbol{T_{evap} = 15\ °C}$, *and* $\boldsymbol{T_{amb} = 25\ °C}$, *90 rps (operating condition 5)*

The dimensionless RMS errors of external profiles are depicted in Table 3.3 at corresponding operating conditions.

Table 3.3 *Dimensionless RMS errors of external profiles in different operating conditions in rotary compressor*

Operating condition	1	2	3	4	5
RMSE (1)	0.031	0.023	0.039	0.029	0.050

3.3 Discussion

The sources of discrepancies between the experimental and numerical values, potentially due to introduced model simplifications, and the model applicability to various component layouts and dimensions are discussed in this subsection.

Numerical values seem to agree with experimental data. The root-mean square errors range from 0.04 to 0.08 and from 0.02 to 0.05 (dimensionless values) in scroll and rotary compressors, respectively. The deviations seem to be smaller in rotary domain than in scroll. Note that the uncertainty of the shell contact temperature sensor is limited to approximately 0.003, or an order of magnitude smaller than RMS differences above.

Presented thermal profiles in Subsection 2.2.3 show that the shell temperature of rotary compressor is relatively uniform regardless of the operating condition. On the other hand, the thermal profiles of scroll compressors, found in Subsection 3.2.1, show a significant temperature jump between the low and high pressure parts of the compressor. More specifically, a strong temperature increase is seen at sensors 5-7. Figure 3.16 and Figure 3.17 are graphical illustrations of the thermal behavior of scroll and rotary compressors obtained in Fluent in the same operating conditions at the same compressor speed. The figures depict that temperature fluctuations of rotary compressor are relatively small in comparison with scroll compressor, where most of the shell remains at low temperature. The operating conditions cannot be disclosed for confidentiality reasons.

Figure 3.16. *Temperature contours of rotary compressor shell in absolute temperature (K)*

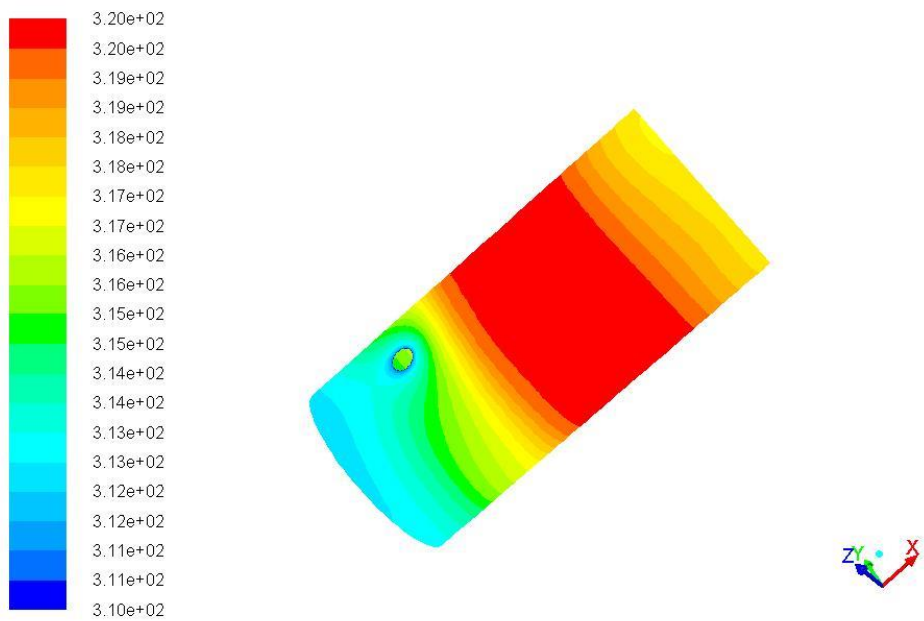

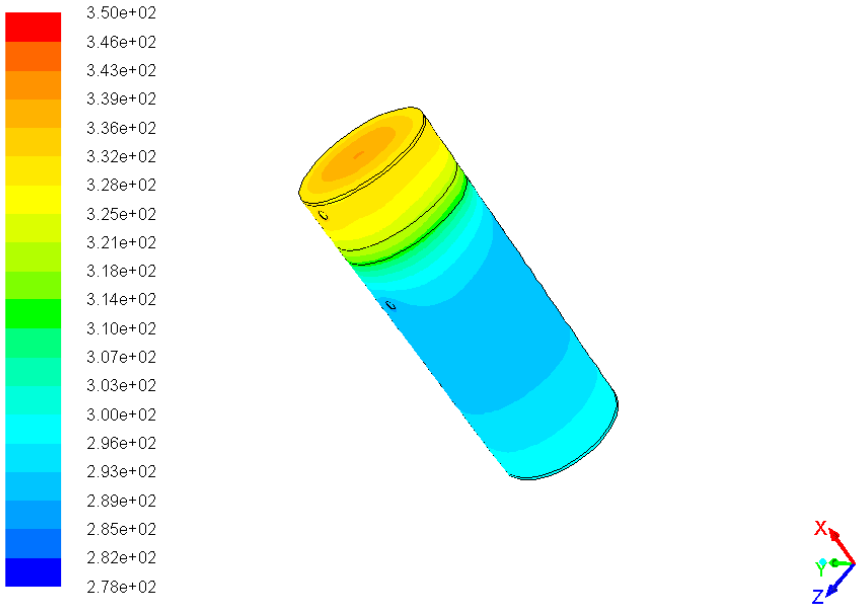

Figure 3.17. *Temperature contours of scroll compressor shell in absolute temperature (K)*

3.3.1 Simplifications

<u>The presence of lubricating oil inside the compressor</u>

In hermetical compressors lubricating oil prevents potential damage of internal components due to friction by lubricating the bearings. In addition to oil being stored in the sump at the bottom, a thin oil film (Figure 3.18) is present over many components inside the compressor, such as the crankcase, stator and the internal surface of the compressor shell. The oil pump is coupled with the crankshaft; as the shaft spins, the lubricating oil flows inside the pump through the crankshaft by centrifugal forces. As it reaches the other extremity of the shaft assembly, part of it is projected as a jet hitting the upper surface of the compressor shell along which it later flows as a thin oil film. The other part of the projected oil returns to the sump by flowing over the compressor crankcase. Oil forms an interface between the refrigerant fluid and the surface of the solid components, which can affect the heat transfer inside the compressor.

Dutra & Deschamps (2013) conducted experimental studies on the effect of the oil flow on the heat transfer of the reciprocating compressor shell for a selected operating condition. It was shown that if the oil heated by the crankshaft is hotter than the refrigerant gas in the discharge plenum, it can contribute to the heating of the discharge gas.

The numerical model considers that oil is still, present only at the bottom. The walls of the interior side of the shell and component surfaces are, therefore, directly in contact with the refrigerant gas. In order to represent the thermal effects of oil film on the crankshaft, its surface temperature was set to T_{oil}. According to Sanvezzo & Deschamps (2012) oil is mainly found on the crankcase, interior side of the compressor shell, and stored at the bottom of the compressor. Therefore, the simplifications made in the numerical model considering oil are justified. However, these simplifications can be responsible for the deviations of numerical values from experimental data.

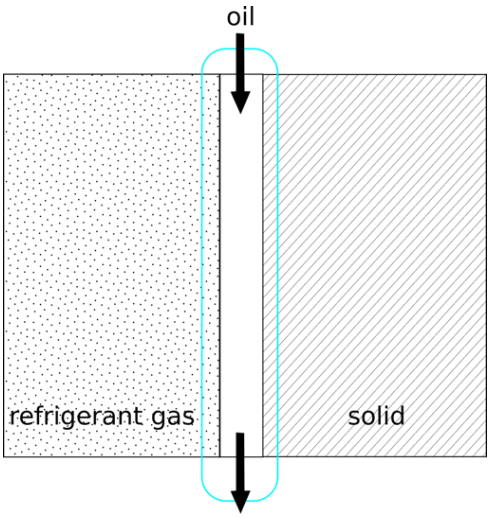

Figure 3.18. *Thin oil film forming an interface betwee the refirgerant gas and a solid component*

Simplified geometry

Intricate geometry of compressor domains is simplified in the second and third steps of the model by removing components that were considered unnecessary from the heat transfer point of view and unnecessary fillets, and overall simplification of the geometrical shapes. Compressor parts consist of cylindrical and rectangular shapes. Geometry and configuration of the internal components modifies the flow dynamics and heat transfer within the domain and, thus, the exterior shell profile. For this reason, simplifications introduced in the geometry of compressor domains were carefully considered: the aim was to find a compromise between sufficient accuracy of the results and reduced complexity level of the model.

Rotating parts, such as crank and rotor, are modeled as stationary in the second part (CFD) of the model. Consequently, the heat transfer coefficients estimated from these surfaces in the second step of the model are inferior to the real ones. However, the third step of the model (thermal network analysis) considers these parts as rotating. If the $\dot{Q}_{comp}$ value in this part deviates by more than 10 % from the value obtained in

the first step of the model (thermodynamic cycle analysis), approximate heat transfer coefficient can be assigned as boundary conditions to the rotating parts in the CFD domain to improve the global convergence of the model. In the simulation results shown in Subsections 3.2.1 and 3.2.2, $\dot{Q}_{comp}$ values obtained from Eqs. (**2.1**) and (**2.29**) in scroll and rotary, respectively, did not deviate more than by 10 % from the Eqs. (**2.15**) and (**2.31**) in scroll and rotary, respectively. Therefore, the thermal profiles were extracted directly from the CFD model, as the model converged.

Rotary compressor used in the test bench had two inlet ports and an accumulator tank on one side. The temperature of the accumulator tank is typically much cooler than the compressor shell, as it serves to accumulate and preheat the fluid in order to ensure that the refrigerant at compressor inlet is in gaseous state. One inlet port compressor was considered in the numerical model, as depicted in Figure 2.4 (b), which might explain some discrepancies between numerical and experimental values in rotary compressors.

Suction superheat in scroll model

It is also important to consider simplifications related to suction superheat in scroll compressors. In the first step of the model (thermodynamic cycle analysis), the suction fluid is assumed to absorb all the heat dissipated by the motor due to electrical losses. Therefore, the temperature of the fluid at the suction of the compression chamber is obtained from the suction enthalpy calculated in Eq. (**2.6**). In reality motor heat is partly absorbed by the fluid and partly dissipated in the ambient air by convective and radiative heat transfer. Refrigerant temperature at suction is, thus, overestimated.

The motor efficiencies are elevated and, therefore, the dissipated motor heat is low and the elevation of refrigerant temperature between inlet and suction cavity is a few degrees only, *i.e.* superheat is low. For these reasons, the part of $\dot{Q}_{mot}$ that escapes to the ambient air can be considered negligible and the overestimated T_{suc} is believed to differ only slightly from the real value. This is particularly the case for scroll compressors with an inlet between the motor and bottom of compression chamber: all of the suction gas is in contact with the top motor surfaces only, and not by the entire motor assembly as in the case of inlet located below the motor. Two refrigerant inlets and their influence on the flow paths are depicted in Figure 3.19.

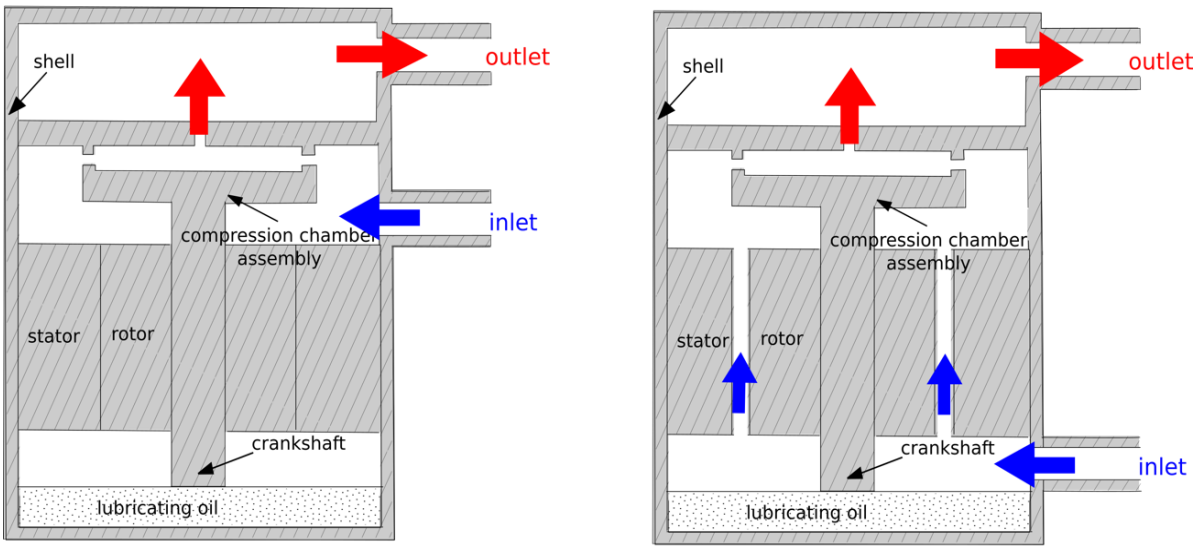

Figure 3.19. *Different inlet locations in scroll compressor and their effect on the refrigerant flow paths*

3.3.2 Model applicability to different compressor dimensions and component layouts

The main purpose of the numerical model was to investigate the thermal behavior of scroll and rotary compressors. However, the component layout of one compressor type – scroll or rotary – can vary, depending on the manufacturer, configuration of the compressor in the refrigeration cycle, *etc*. For instance, the refrigerant inlet of a scroll compressor can be located between the compression chamber and the motor or at the bottom, as depicted in Figure 3.19. In this case the flow dynamics and the internal temperature distribution are altered, which reflects directly on the temperature distribution of the exterior shell.

In order to extend the model to other types of scroll and rotary compressors, first, the component layout of the compressor of interest must be compared to the compressor layout in the numerical model. Specifically, the location of inlet and outlet ports and compression chamber, the refrigerant flow path, and motor assembly (size of stator-shell and stator-rotor gaps) must be examined. Second, if the mentioned characteristics vary significantly from the ones presented in Chapter 2, the component layout must be adapted to the new one in all of the steps of the model, specifically, second and third.

Some deviations between component layouts may require only minor modifications. For example, if the location of the inlet port in scroll compressor is at the bottom, below the motor, then the inlet port must be lowered in the second step (differential part) and a gap in the motor assembly must be inserted in order to create a path for the fluid to reach the compression chamber. Heat transfer coefficients for fluid passing between two concentric cylinders introduced in Appendix C must be employed in the third step of the model.

Other deviations between the layouts may require more extensive changes in the model. An example of such case is if the compression chamber is located at the bottom in scroll compressors. This would imply great modifications, specifically, in the second step.

The model can be easily adapted to compressors that have different dimensions than the ones already configured. This implies modifying the geometry parameters in the CFD part of the model and updating the mesh, and modifying the characteristic lengths and heat transfer areas in the third step of the model.

To conclude, it can be assumed that the model is applicable with few modifications to a wide range of compressors used in residential applications, since only the most essential and general compressor components were modeled including a general component layout scheme, and the dimensions can be adjusted easily. However, if the component layout deviates significantly from the modeled one, some substantial adjustments must be implemented.

3.4 Future development

Numerical model can be employed to investigate exterior thermal profiles in a great variety of operating conditions by varying ambient, evaporation, and condensation temperatures, as well as refrigerant fluids. This information can then be exploited to generalize and validate the instrumentation method to evaluate compressor heat losses on-field, defined in Chapter 4, over a wider range of operating conditions. Since the models are adapted to consider an insulation layer, the influences of different insulation materials and their thicknesses can be investigated as well.

It is observed that in most residential HP applications the compressor is enclosed in a casing and is, therefore, subjected to heat transfer by natural convection. However, in some applications compressors can be exposed to mixed/forced convection. For the moment mixed and forced convection cannot be implemented easily in the CFD part of the model due to convergence issues. Therefore, the possibility of adapting the model to integrate other convection regimes by assigning different air velocities in x, y, or z direction must be investigated.

As mentioned previously, the model can be adapted to different component layouts. For example, the inlet port can be moved from the top to the bottom of the compressor, as depicted in Figure 3.19. In such case the influence of the inlet port location on the exterior thermal profile and compressor heat losses in scroll compressors calculated using the method described in Chapter 4 can be investigated.

The models can also be used to investigate the effects of different operating parameters and motor efficiencies on the internal temperature distribution, as the models provide information about the temperatures of the internal components. This information can then be used to identify the hottest and, thus, most vulnerable to damage, zones in the compressor design.

3.5 Conclusions

Temperatures on the exterior shell of scroll and rotary compressors were compared to the temperatures obtained from an experimental test bench in MHI laboratory in five operating conditions. The second step (CFD part) took approximately 4 and 2 hours to converge in scroll and rotary compressors, respectively. In both cases the difference between $\dot{Q}_{comp}$ values calculated in the first and third steps of the model was below 10 %, and the models were considered to be globally converged. The RMS errors of dimensionless temperature values of external profiles range between 0.04 and 0.08 in scroll compressor and 0.03 and 0.05 in rotary compressor. Results obtained in rotary compressor tend to be slightly more accurate.

The numerical model showed that the shell of rotary compressor is relatively uniform regardless of the operating condition. Scroll compressor, on the other hand, exhibits a strong temperature jump at the level of compression chamber suggesting that a great deal of heat losses occur at the top part of scroll compressors.

There seems to be a good agreement between the temperature values of the internal components obtained from the numerical model for scroll compressors and the experimental values. This information can be of use when evaluating component vulnerability to thermal damage.

Simplifications introduced in the numerical model, such as the simplifications related to lubricating oil and component geometry, influence the accuracy of the model. However, these simplifications were inevitable in order to maintain the model flexible, in terms of its capacity to be applied to different geometrical layouts, and computationally inexpensive.

CHAPTER 4

IMPROVED IN SITU EVALUATION METHOD OF COMPRESSOR HEAT LOSSES FOR PERFORMANCE ASSESSMENT

Dans ce chapitre, les modèles numériques développés sont utilisés pour déterminer le nombre et la position de capteur(s) de température nécessaires à la mesure de température de l'enveloppe des compresseurs. L'objectif est d'améliorer la précision de mesure des sur site.

Pour le compresseur rotary, le capteur situé entre la chambre de compression et le bas du moteur est le plus représentatif de la température moyenne de l'enveloppe. Pour le compresseur scroll, la partie basse du compresseur (basse pression) reste froide et la majeure partie des pertes thermiques ont lieu en sur la partie haute (haute pression). La température mesurée par le capteur sur l'enveloppe au niveau de la chambre de refoulement doit être utilisée pour estimer la température moyenne de la partie haute pression du compresseur. Ainsi, une corrélation développée ici doit être utilisée pour prendre en compte les pertes thermiques totales de ce type de compresseur. La corrélation développée est valable quand la température moyenne de la partie basse pression, mesurée par le capteur situé sur l'enveloppe à mi-hauteur du moteur, est plus élevée que la température de l'air ambiant.

Pour conclure, pour mesurer les pertes thermiques sur site, deux capteurs de température sur l'enveloppe sont nécessaires dans le cas d'un compresseur de type scroll ; un seul dans le cas d'un compresseur de type rotary.

De plus, les corrélations utilisées pour calculer les coefficients de transferts de chaleur en convection naturelle pour les différentes surfaces des compresseurs (haut, bas et surfaces latérales), obtenues à partir d'une revue bibliographique, sont également présentées dans ce chapitre.

4.1 Introduction

This chapter presents the improved calculation method to evaluate rotary and scroll compressor heat losses. This method can be integrated on-field in the performance assessment method. The method includes Nusselt number correlations found in the literature. These correlations account for the nature of the flow and the geometry of the compressor shell. The optimal instrumentation to measure heat losses of rotary and scroll compressors on-field is determined based on the results – thermal profiles and heat flux distribution on the compressor shell – of the numerical models.

4.2 Existing methods of compressor heat loss modelling

One approach to measure compressor heat losses in situ is to model heat losses as a function of compressor power input, $\dot{W}_{comp}$, as described in the work of Fahlén (2004), depicted in the equation below:

$$\dot{Q}_{amb} = \eta \dot{W}_{comp} \tag{4.1}$$

where η is the heat loss factor, assumed to be constant and known, and equal to 0.08. However, experimental data obtained from compressor test bench, described in Chapter 3, in MHI laboratories, where $\dot{Q}_{amb}$ values were obtained from the compressor energy balance, showed that η varies between 7 and 13 % in scroll compressors and between 5 and 47 % in rotary compressors, depending on the operating condition and rotation speed.

Compressor heat losses can be represented using a shell and ambient temperature relationship, as in the work of Tran *et al.* (2013) presented in Subsection 1.2.2, as follows:

$$\dot{Q}_{amb} = a(T_{shell} - T_{amb}) + b(T_{shell}^4 - T_{amb}^4) \tag{4.2}$$

where T_{shell} is the temperature, T_{amb} is the ambient temperature, and factors a and b are obtained from compressor geometry and the nature of heat transfer. Factors a and b represent convective and radiative heat exchange coefficients, respectively, calculated, as follows:

$$a = h_c A \tag{4.3}$$

$$b = \sigma A \tag{4.4}$$

As mentioned in Subsection 1.2.2, it was assumed that T_{shell} is uniform and equal to discharge temperature, $T_{comp,ex}$. This approximation is not justified, particularly, in the case of scroll compressors; as shown in Figure 3.17, most of the scroll compressor shell remains at low temperature and only the top part of the shell approaches the discharge temperature value.

Simulation results have also shown that in rotary compressors the discharge temperature values deviate from the area-weighted average temperatures obtained from the CFD program, presented in Table 4.1 and discussed in more detail in Subsection 4.3. The deviations between the temperature values obtained from different temperature sensor locations and the area-weighted average temperatures of the entire rotary compressor shell can be seen in Table 4.1. It is observed that the shell temperature at discharge overestimates the average shell temperature.

Table 4.1. *The RMS errors of temperature values measured from different temperature sensors from the area-weighted average temperatures of the rotary compressor shell*

Operating conditions				
T_{cond} (°C)	T_{evap} (°C)		T_{amb} (°C)	speed (rps)
40	0		10	60
40	0		10	90
60	0		10	30
60	0		10	60
40	15		25	30
RMS errors (°C)				
T_{out}	Sensor 3	Sensor 4	Sensor 5	Sensor 6
4.84	1.88	5.26	2.30	2.70

Other researchers have suggested that the compressor shell temperature may depend on many factors, such as the pressure ratio, suction pressure, and discharge pressure/temperature. Correlations have been developed in previous works establishing a relationship between T_{shell} and other variables related to the operating conditions. For instance, Kim and Bullard (2002) proposed a linear dependence between T_{shell} and T_{dis} for small hermetic reciprocating, rotary, and scroll compressors. The model was developed based on thermodynamic principles and large data sets from compressor calorimeter and in situ tests. A linear correlation was suggested by Duprez *et al.* (2010), where T_{shell} is a function of evaporation and condensation temperatures in scroll compressors. Li (2013) conducted an analysis of experimental data over a wide range of operating conditions and suggested a non-linear correlation for T_{shell} of reciprocating,

rotary, and scroll compressors, as a function of the pressure ratio and discharge pressure.

It is challenging to determine a correlation that accurately represents T_{shell} and takes into account the physical aspects of heat exchange and compressor geometry, yet remaining relatively simplified in terms of unknown parameters and possessing a good extrapolation capacity. In addition, assuming that T_{shell} is uniform, specifically in the case of scroll compressors with compression chamber on top implies significant simplifications since strong temperature fluctuations (Figure 3.17) take place along the shell.

4.3 Improved calculation method of compressor heat losses

In order to establish a more accurate method to evaluate compressor heat loss on-field, first, appropriate correlations for convective heat coefficient were found in literature. Then, the results of the numerical model were used to define the appropriate instrumentation, in terms of sensor number and their location, to accurately measure T_{shell}.

4.3.1 Nusselt number correlations for convective heat transfer coefficients

Heat exchange between the exterior envelope of the compressor and the environment occurs by radiation and convection. Heat exchange by conduction is considered negligible. Compressor can either be exposed to forced, natural, or mixed convection. Natural convection is believed to occur when the only force generating air movement is gravity, *i.e.* no external force is generating air movement, unlike in forced convection. Changes in fluid temperature result in density changes, and in a gravitational field the lighter fluid is pushed upwards by buoyance force, which is then replaced by a denser and cooler fluid. This results in air movement, thus heat transfer by convection takes place. Mixed convection occurs when the buoyancy forces in forced flows are non-negligible: neither natural nor forced convection mode dominates.

Whether natural, forced, or mixed convection takes place depends on the configuration of the compressor inside the HP exterior/interior unit. In most residential application compressor is enclosed inside a casing and is, therefore, submitted only to natural convection. For this reason only the case of heat transfer occurring by natural convection is investigated.

Correlations available from literature that account for physical characteristics of heat transfer and compressor geometry have been carefully selected. Dimensionless Rayleigh number for natural convection is used to estimate the flow regime of air, and is calculated as follows:

$$Ra_x = \frac{g\beta(T_{shell} - T_{amb})}{\nu\alpha} x^3 \tag{4.5}$$

where g is the gravitational acceleration, β is the thermal expansion coefficient, ν is the kinematic viscosity, α and is the thermal diffusivity. Material properties are considered at T_{film}.

Air can be assumed to be an ideal gas, therefore, the thermal expansion coefficient is depicted in the following equation:

$$\beta = \frac{1}{T_{film}} \tag{4.6}$$

A literature review of available correlations has yielded the following correlations for isothermal surfaces, which are best fitted to the nature of flow and compressor geometry in question. Churchill & Chu (1975) proposed a Nusselt number correlation for vertical plates in laminar flows:

$$\overline{Nu}_L = 0.68 + \frac{0.67 Ra_L^{1/4}}{(1 + (0.492/Pr)^{9/16})^{4/9}} \qquad (Ra_L \leq 10^9) \tag{4.7}$$

where is the Prandtl number and L is the length of the lateral part. The correlation is adapted as follows to turbulent flow regime:

$$\overline{Nu}_L = \left(0.825 + \frac{0.387 Ra_L^{1/6}}{(1 + (0.492/Pr)^{9/16})^{8/27}}\right)^2 \qquad (10^9 \leq Ra_L \leq 10^{12}) \tag{4.8}$$

This empirical correlation was used for the lateral part of the compressor cylinder.

McAdams (1954) recommended an experimental correlation for heated horizontal plates facing up in laminar flow regime:

$$\overline{Nu}_D = 0.54 Ra_D^{1/4} \qquad (10^5 < Ra_D \leq 10^7) \tag{4.9}$$

for turbulent flows as follows:

$$\overline{Nu}_D = 0.14 Ra_D^{1/3} \qquad (10^7 < Ra_D < 3 \cdot 10^{10}) \qquad (4.10)$$

which were used for scroll and rotary compressor top surfaces.

For the bottom surfaces, a correlation suggested by Kadambi & Drake (1960) for heated horizontal plates facing down in laminar and turbulent regimes:

$$0.82 Ra_D^{1/5} \qquad (10^5 < Ra_D < 10^{10}) \qquad (4.11)$$

The correlations recommended by McAdams (1954), Eqs. (**4.9**) and (**4.10**), and Kadambi & Drake (1960), Eq. (**4.11**), were developed for horizontal square plates. However, they were adapted to compressor top and bottom surfaces despite them being of circular shape. Diameter of the plates was selected as the characteristic length instead of the side length, as assumed originally in the correlations.

4.3.2 Optimal on-field instrumentation for T_{shell}

Results obtained from compressor test bench and the second step of the numerical model (CFD model) were used to determine the zones on scroll and rotary compressor shell that contribute the most to compressor heat losses, by investigating their shell thermal profiles and heat flux distributions in various operating conditions.

As seen from the results shown in Subsection 3.2.2, the temperature distribution of rotary compressor shell is quite uniform. The hottest point on the shell is at the level of the middle of the motor assembly (sensor 4 in Figure 3.2 (b)). However, its deviation from the rest of the shell temperatures seems to be small. Therefore, rotary shell can be considered as an isothermal zone.

As mentioned earlier, the area-weighted averages presented in Table 4.1 show that the most representative location for measuring the average temperature of rotary compressors is sensor 3, which is located at the level of the space between compression chamber and motor assembly (Figure 3.2 (b)). However, as seen from Table 4.1, measuring the temperature from the top part of the compressor (sensor 5, at the level of discharge plenum in Figure 3.2 (b)) gives a very close estimation of the area-weighted average as well.

Investigating the thermal profiles of scroll compressor, Subsection 3.2.1, shows that there is a significant temperature gradient along the shell (temperature jump), specifically, at sensors 6 and 7, which are located above the compression chamber as seen in Figure 3.2 (a). Examining the heat flux distribution on the compressor shell using the

results obtained from the numerical model has shown that most of the heat losses occur at the high pressure (HP) part of the compressor: from the bottom of the compression chamber to the top on the lateral side, and the top horizontal surface. Table 4.2 shows the ratio of heat transferred to the ambient from the mentioned zones, $\dot{Q}_{amb,top}$, to the total shell heat losses, $\dot{Q}_{amb,tot}$.

Table 4.2. *Shell heat flux ratio of scroll compressor extracted from Fluent in different operating conditions*

T_{cond} (°C)	T_{evap} (°C)	T_{amb} (°C)	speed (rps)	$\dot{Q}_{amb,top}/\dot{Q}_{amb,tot}$
40	0	10	30	0.76
40	0	10	60	0.86
40	0	10	90	0.89
60	0	10	30	0.75
60	0	10	60	0.81
60	0	10	90	0.86

Table 4.2 shows that the heat flux ratio tends to vary with speed despite the pressure ratio and ambient temperature remaining constant. Furthermore, as the compression ratio is increased, from ($T_{cond} = 40\ °C$, $T_{evap} = 0\ °C$) to ($T_{cond} = 60$ ℃, $T_{evap} = 0$ ℃), the heat flux ratio remains relatively constant at 30 rps, 76% and 75%, respectively, or slightly decreases at 60 and 90 rps.

Oil temperature on the bottom of the compressor is dependent on the outlet temperature, as depicted in Eq. (**2.30**). As the condensation temperature increases, the outlet temperature increases, thus, T_{oil} increases as well. In this case the bottom of the compressor becomes hotter, as the HP part of the compressor becomes hotter. However, when the speed is increased the oil temperature is assumed to remain approximately constant, since the variations in T_{out} are minor. Therefore, the bottom of the compressor remains at the same temperature while the HP part becomes hotter, as the speed increases. For this reason, the heat flux ratio was assumed to depend on the compressor power input: as the speed increases at the same operating condition, the mass flow rate and power input are increased. Since the motor efficiency is considered to be high and constant, and the motor is cooled by the refrigerant in any case, an increase in power input primarily augments the heat exchange of the HP part of the compressor, thus increasing the ratio. The correlation used for the heat flux ratio is depicted in the following equation:

$$\frac{\dot{Q}_{amb,top}}{\dot{Q}_{amb,tot}} = 0{,}036\left(\dot{W}_e/\dot{W}_{nom}\right) + 0.7427 \qquad (4.12)$$

where $\dot{W}_{nom}$ is the electrical power input in operating condition 1 (Table 4.2).

This correlation is valid if the average temperature of the bottom part of the cylinder, the LP part, is higher than the ambient temperature (the reverse situation could occur in a cooling mode but was not considered here). The average shell temperature of LP cylinder part in scroll compressors can be measured from sensor 3 (middle of the motor). If the average LP shell temperature, $T_{shell,LP}$ is higher than the ambient temperature, sensor 6 (at the level of discharge plenum) must be used to determine the average temperature of the HP part and the obtained heat losses must be multiplied by the reciprocal of the heat flux ratio obtained from Eq. (**4.12**).

To sum up, the required instrumentation to determine T_{shell} in rotary compressors is:

- **temperature sensor at the level of the space between the compression chamber and motor bottom** ($\boldsymbol{T_{shell} = T_{shell,3}}$),
- this location reflects the area-weighted average shell temperature the most,
- **one sensor required**.

Similarly, the required instrumentation to determine T_{shell} in scroll compressors is:

- **one sensor at the level of discharge plenum** ($\boldsymbol{T_{shell,HP} = T_{shell,6}}$) **and one sensor at the level of the middle of the motor** ($\boldsymbol{T_{shell,LP} = T_{shell,3}}$),
- heat losses from the high pressure part of scroll compressor are evaluated,
- correlation in Eq. (**4.12**) must be used to account for the total heat flux area,
- correlation is valid if $T_{shell,LP} > T_{amb}$,
- **two sensors required in total**.

Figure 4.1 represents schematically the location and number of temperature sensors required for evaluating heat losses of rotary and scroll compressors on-field.

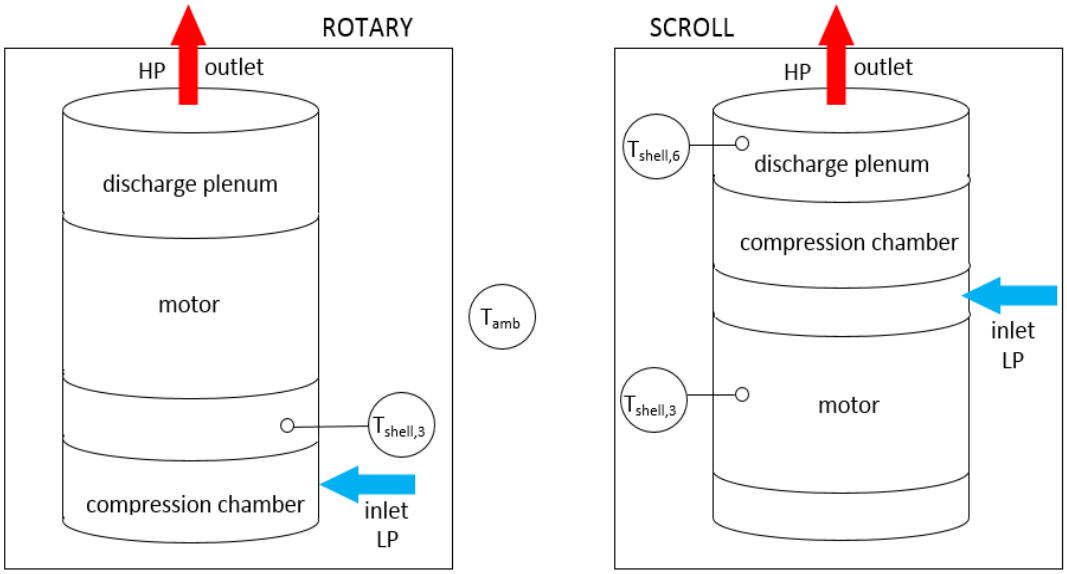

Figure 4.1. *Location of temperature sensors required to evaluate heat losses of rotary (on the left) and scroll (on the right) compressors*

4.3.3 Heat loss expression for compressors

To conclude, compressor heat losses in rotary compressors are calculated from the following equation, already presented in Subsection 1.2.2:

$$\dot{Q}_{amb} = \left(\frac{\overline{Nu}_L k}{L} A_L + \frac{\overline{Nu}_{D,1} k}{D} A_D + \frac{\overline{Nu}_{D,2} k}{D} A_D\right)\left(T_{shell,3} - T_{amb}\right) + \sigma A_{tot}\left(T_{shell,3}^4 - T_{amb}^4\right) \quad (4.13)$$

where $\overline{Nu}_L$ is the Nusselt number for the lateral side, Eq. (**4.7**) or (**4.8**), and $\overline{Nu}_{D,1}$ is the Nusselt number for top surface, Eq. (**4.9**) or (**4.10**), $\overline{Nu}_{D,2}$ is the Nusselt number for bottom surface, Eq. (**4.11**), A_L is the lateral side area, A_D is the top and bottom plate areas.

Similarly, heat losses in scroll compressors are calculated as follows:

$$\dot{Q}_{amb} = \frac{1}{R_{HF}}\left[\left(\frac{\overline{Nu}_L k}{L} A_{L,HP} + \frac{\overline{Nu}_{D,1} k}{D} A_D\right)\left(T_{shell,6} - T_{amb}\right) + \sigma A_{tot,HP}\left(T_{shell,6}^4 - T_{amb}^4\right)\right] \quad (4.14)$$

where $A_{L,HP}$, and $A_{tot,HP}$ are the HP lateral and total HP areas, respectively, and R_{HF} is the heat flux ratio for top and total heat fluxes calculated from Eq. (**4.12**).

4.4 Conclusions

As mentioned earlier the main simplification introduced in the heat loss model presented in Tran *et al*. (2013), was that the compressor shell was considered to be isothermal and equal to refrigerant temperature at discharge, which is not the case, particularly, in scroll compressors, as seen in the results of Subsection 3.2.1. In this chapter the developed numerical models were used to determine the location of the necessary temperature sensors that best represent T_{shell} of scroll and rotary compressors, and thus, allow a more accurate heat loss estimation on-field.

The shell of the rotary compressor is mostly isothermal. The RMS errors between different temperature sensor locations and the area-weighted averages of the shell temperatures obtained from the numerical model in different operating conditions were used to determine the most optimal temperature sensor location. Temperature sensor located between the compression chamber and motor assembly (sensor 3, Figure 3.2 (b)) is the most representative of the average shell temperature in rotary compressors.

In scroll compressors most of the shell (the LP part) remains relatively cold, and most of the heat flux occurs on the top part of the compressor shell (the HP part). Comparing heat flux ratios of the HP part to the total heat flux of the shell showed that approximately 80 % of the heat losses in scroll compressors occur on the top lateral part and top flat horizontal plate. A correlation, Eq. (**4.12**), was derived based on the obtained results, which represents the ratio of HP heat losses to the total shell heat losses. However, the correlation is only valid if the average shell temperature of the LP part of the compressor measured on the shell at the level of the middle of the motor (sensor 3 in Figure 3.2 (a)) is higher than T_{amb}. In such case the shell temperature at the level of discharge plenum (sensor 6 in Figure 3.2 (a)) must be used to determine the average temperature of the HP part. To conclude, two temperature sensors must be used in scroll compressors and one temperature sensor must be used in rotary compressors when estimating compressor heat losses on-field.

In this chapter, the correlations used to calculate heat transfer coefficients in natural convection regime for top, bottom, and lateral compressor surfaces obtained from a literature review were presented. Equations are embarked on-field to calculate heat losses of scroll and rotary compressors, respectively.

CHAPTER 5

EXPERIMENTAL VALIDATION OF THE PERFORMANCE ASSESSMENT METHOD

L'objectif du banc d'essai expérimental était de valider la méthode de mesure des performances intégrant la nouvelle approche d'évaluation des pertes thermiques, définie dans le chapitre 4, pour le compresseur de type rotary. Un prototype a été construit et testé pour plusieurs points de fonctionnement. Les valeurs de référence de la puissance calorifique ont été calculées à partir des mesures sur le circuit d'eau.

Après comparaison avec les valeurs de référence, l'erreur moyenne quadratique de la méthode de mesure des performances améliorée est 2.36 %. L'erreur moyenne quadratique obtenue pour la méthode de mesure des performances intégrant l'ancienne approche d'évaluation des pertes thermiques, décrit par Tran *et al.* (2013), est 7.51 %.

Enfin, le banc d'essai expérimental a permis de :

- valider la nouvelle approche pour évaluer les pertes thermiques du compresseur rotary,
- définir que l'endroit optimal pour mesurer la température de l'air ambiant est en entrée de l'évaporateur dans le prototype,
- déterminer que 0.5 % est une valeur constante plus appropriée pour le taux d'huile

5.1 Introduction

In this chapter the performance assessment method that integrates the improved heat loss evaluation, described in Section 4.3, is experimentally validated for the case of HP equipped with a rotary compressor. For this purpose, an experimental test bench was built using an air-to-water HP prototype to be tested in various operating conditions. The prototype consists of an exterior unit comprising a variable rotary compressor, electronic expansion valve, evaporator, and a fan. The interior unit consists of a condenser that releases heat to a water circuit, which heats a hot water tank. The water inlet temperature is controlled with the aid of a thermal control unit. The tests are performed at different evaporation condensation, and ambient temperatures, as well as various compressor speeds.

The heating capacities estimated with the performance assessment method, which integrates the improved heat loss evaluation method (new location for T_{shell} and new correlations) described in Chapter 4, are compared to the reference values, calculated from the water-side measurements.

Different sensor locations to measure the ambient temperatures and their influence on the discrepancies between the heating capacities were investigated. Based on this information the best location for an ambient temperature sensor in this particular case is selected. One objective is to know if the already-installed outdoor temperature sensor of the HP is sufficient or if an additional sensor is required inside the compressor enclosure. In addition, the influence of the oil mass fraction value is investigated.

5.2 Heat pump prototype

An air-to-water HP prototype was built to validate the performance assessment method that integrates the improved compressor heat loss evaluation presented in Subsection 4.3, Eq. (**4.13**), for rotary compressors. The prototype consists of an exterior and interior unit. The exterior unit comprises a variable speed compressor, EEV, fan, and an evaporator. A metallic sheet envelopes the exterior unit components. Another metallic sheet is used to separate the compressor and expansion valve from the evaporator and fan, as depicted in Figure 5.1. Figure 5.2 and Figure 5.3 portray the exterior unit from the side of the heat exchanger surface and the fan, respectively. Wiring of the temperature and pressure sensors can be seen on the figures as well.

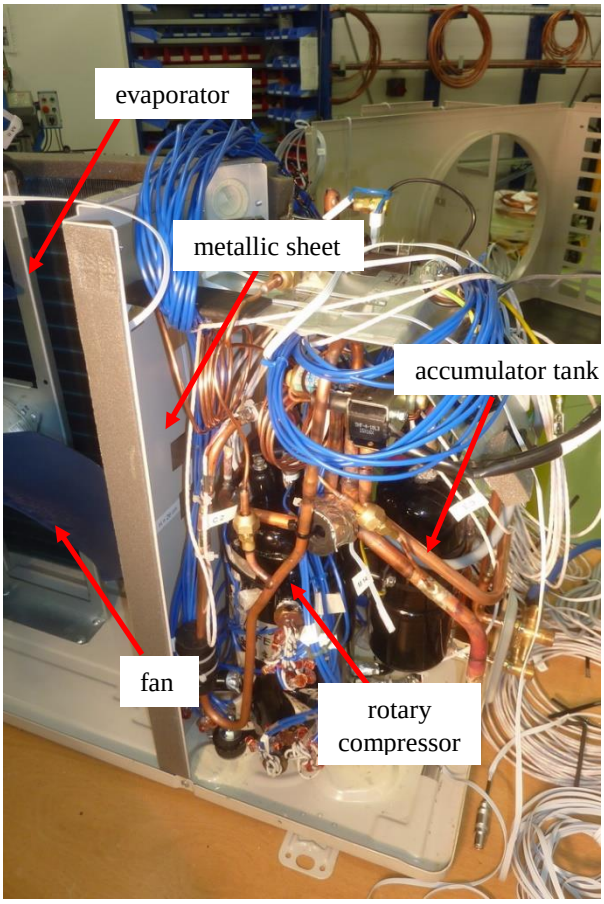

Figure 5.1. *Exterior unit with a compressor and EEV separated by a metallic sheet from the evaporator and fan*

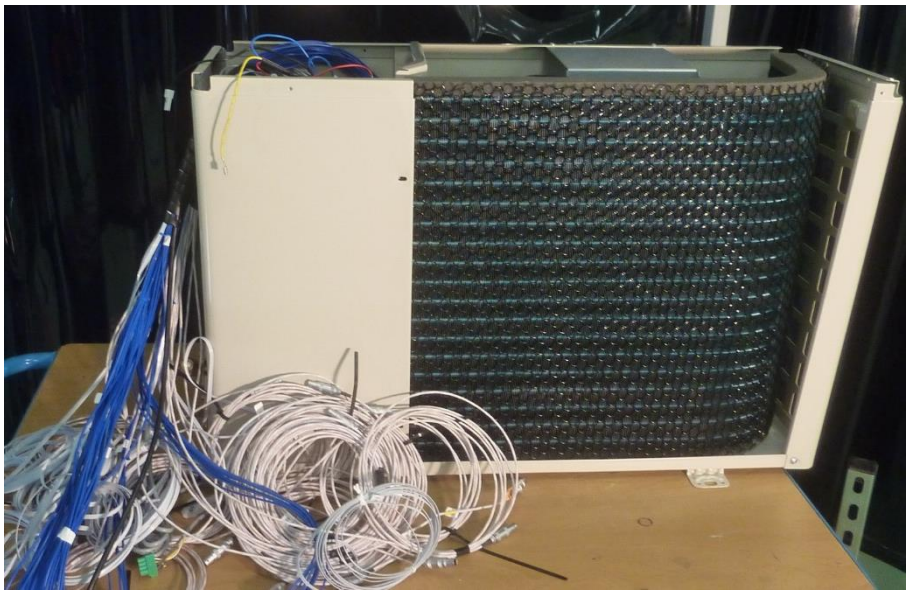

Figure 5.2. *Exterior unit from the side of the evaporator*

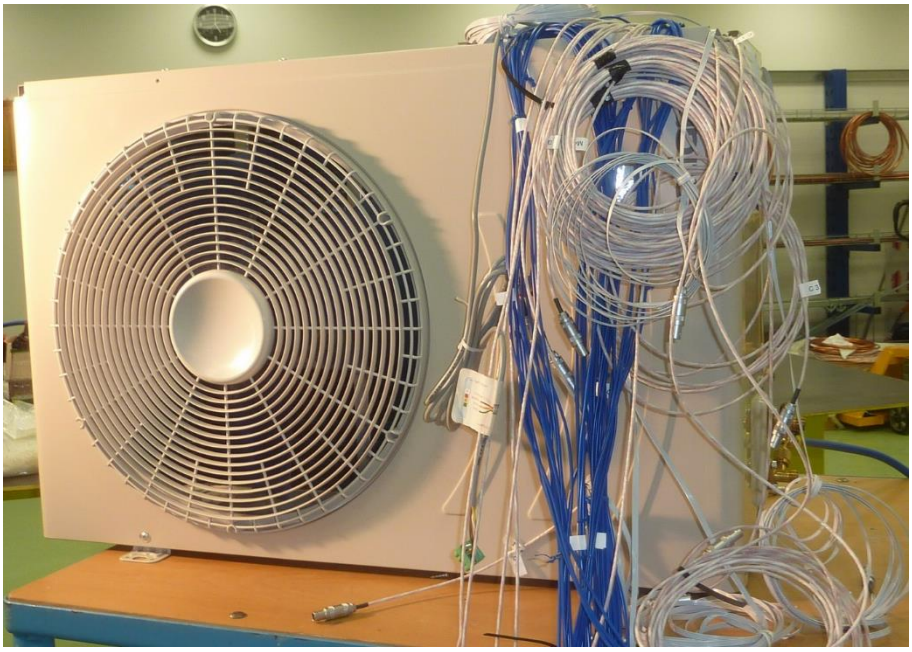

Figure 5.3 *Exterior unit from the side of the fan*

Compressor used in the tests was the same as the one used in the experimental test bench described in Chapter 3 for the validation of the exterior thermal profiles in rotary compressors. The refrigerant used in the tests was R134a. Polyolester oil was used to lubricate the compressor components. In this experimental setup there was no insulation layer around the compressor.

Interior unit consisted of a condenser that released heat to the water circuit.

5.3 Experimental setup

The air-to-water prototype extends over three rooms. The exterior unit (rotary compressor, expansion valve, evaporator, and fan) is set up in climatic chamber number 1 and the interior unit, which consists of a condenser connected to a water loop, is set up in another room (number 2). The water loop is fitted with a tank and water temperature control unit. The control unit of the water inlet temperature is situated in room 3. Temperature control unit is used to cool the water inlet temperature, $T_{w.i}$. The experimental setup can be seen in Figure 5.4, Figure 5.5, and Figure 5.6

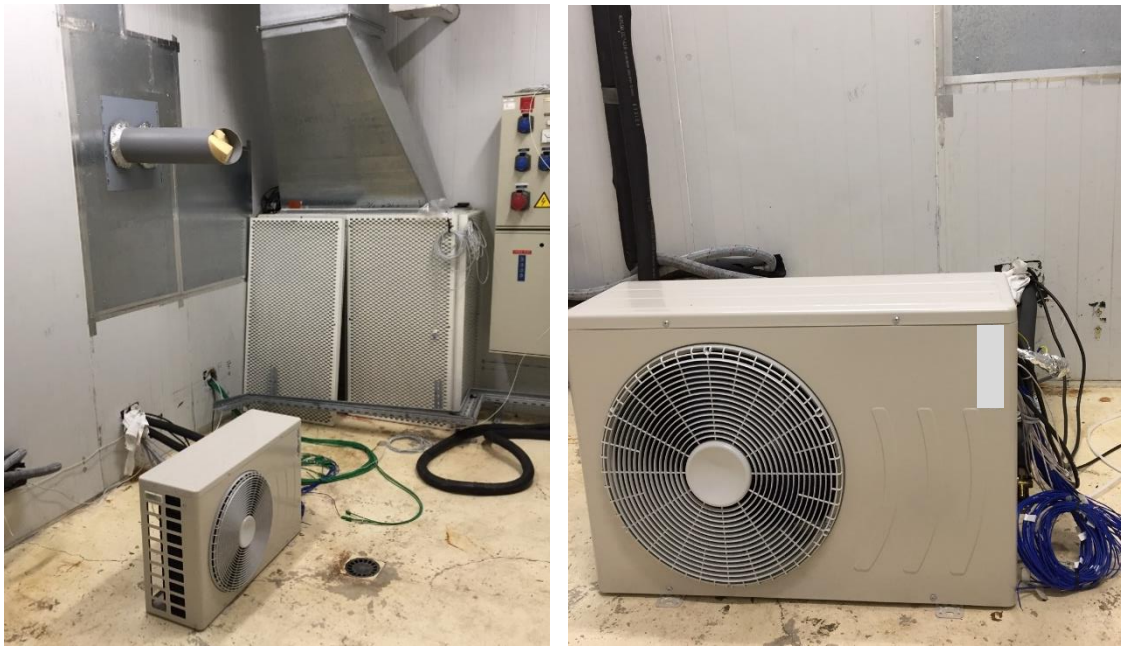

Figure 5.4. *Exterior unit located in the climatic chamber 2 (outdoor chamber)*

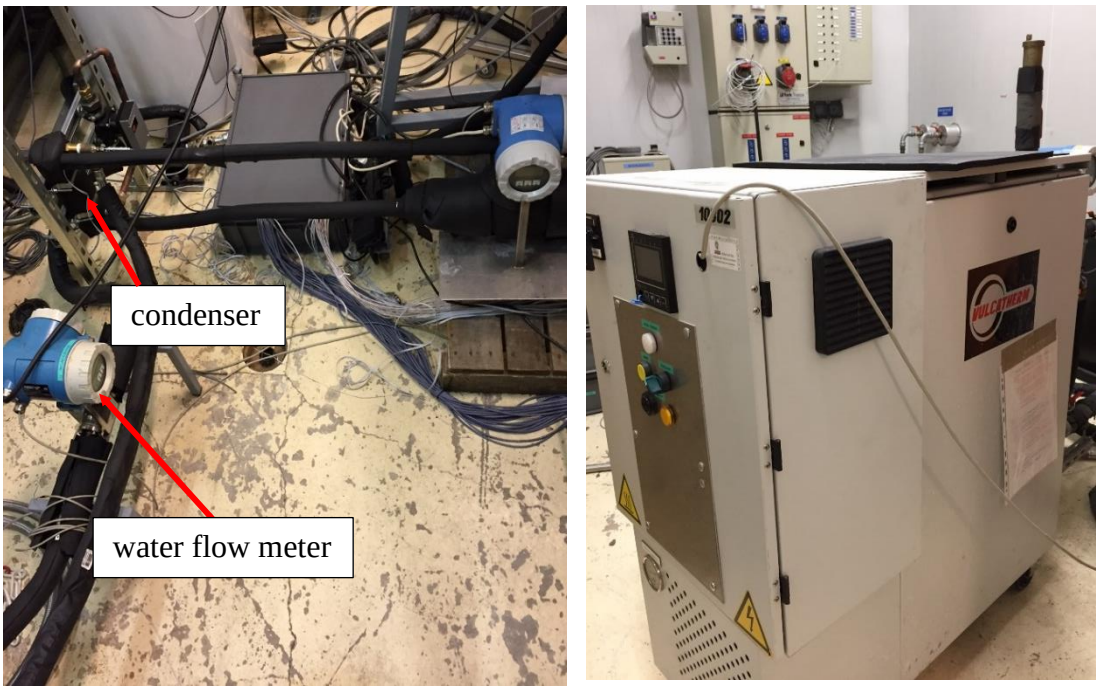

Figure 5.5. *Indoor unit with condenser coupled to a water loop (on the left) and contorl unit of water inlet temperature located in room number 3 (on the right)*

Measurement variable sampling rate is 0.1 Hz for a duration of approximately two hours at each operating condition. Data acquisition and control of temperatures, pressures, water flow rate, *etc.*, is done in Laboratory Virtual Instrument Engineering Workbench (LABview), which is a development environment based on a graphical programming language used to create various applications that interact with measurement signals.

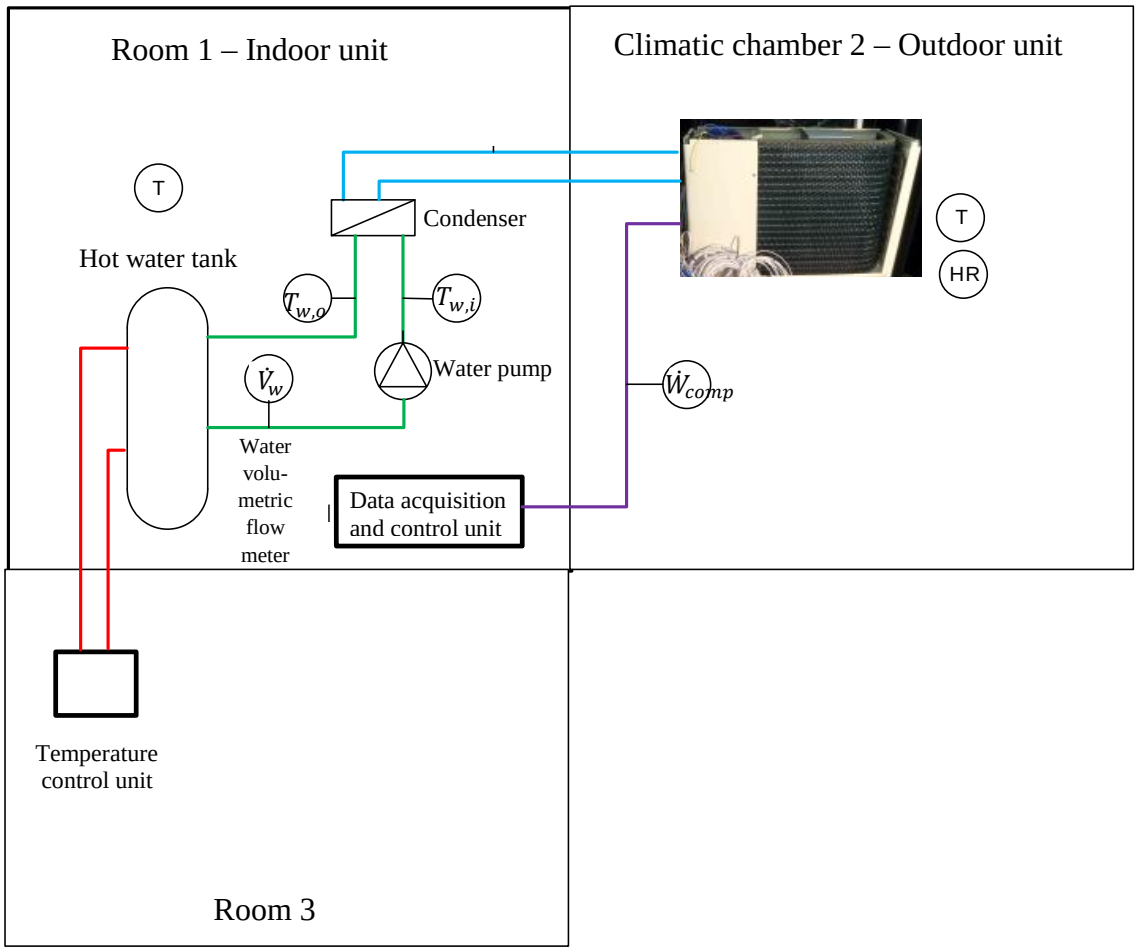

Figure 5.6. *Air-to-water HP prototype and required instrumentation installed in three climatic chambers*

The instrumentation of the experimental setup consists of:

- wattmeter;
- electromagnetic flow meter (for water flow measurements);
- high and low pressure sensors;
- temperature sensors (PT100) and
- humidity sensors.

The mass flow rate of water is used to regulate the condensation temperature, and ambient temperature and relative humidity level are used to regulate the evaporation temperature. The condensation temperatures were set at 40 and 60 °C, and evaporation temperatures ranged from 0 to 2 °C.

In order to determine the compressor heat losses, the air temperature surrounding the compressor must be known. In the work of Tran *et al.* (2013) ambient temperature was taken as the exterior temperature. In order to see whether this is indeed the best location for measuring accurately the temperature of the air surrounding the compressor, various temperature sensors were installed around the compressor (Table 5.1) to test the influence of ambient temperature measurements on the accuracy of the performance measurement method. As seen from the instrumentation schematic (Figure 5.7), eight temperature sensors were installed around the compressor; seven on the metallic walls and one sensor (T_{air7}) was floating right above the top of the compressor, *i.e.* the sensor was hanging by its wire. In addition, one temperature sensor is placed in the calorimeter chamber (outdoor unit) at the evaporator inlet to measure the ambient temperature (Figure 5.8).

Table 5.1. *Location of ambient temperature sensors*

Sensor	Location
T_{air1}	Bottom of the compressor metal enclosure
T_{air2}	Metal sheet between compressor and evaporator
T_{air3}	Side of the compressor metal enclosure
T_{air4}	Side of the compressor metal enclosure
T_{air5}	Top of the compressor metal enclosure
T_{air6}	Side of the compressor metal enclosure
T_{air7}	Hanging above the compressor
T_{air8}	Side (at the bottom) of the compressor metal enclosure
T_{ext}	Center of the exterior unit at the air inlet side

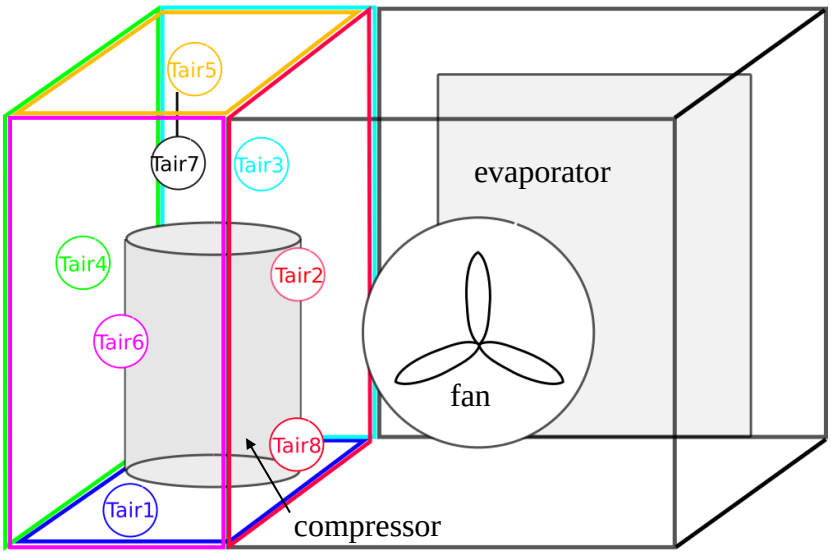

Figure 5.7. *Locations of sensors used to measure the temperature of air surrounding the compressor*

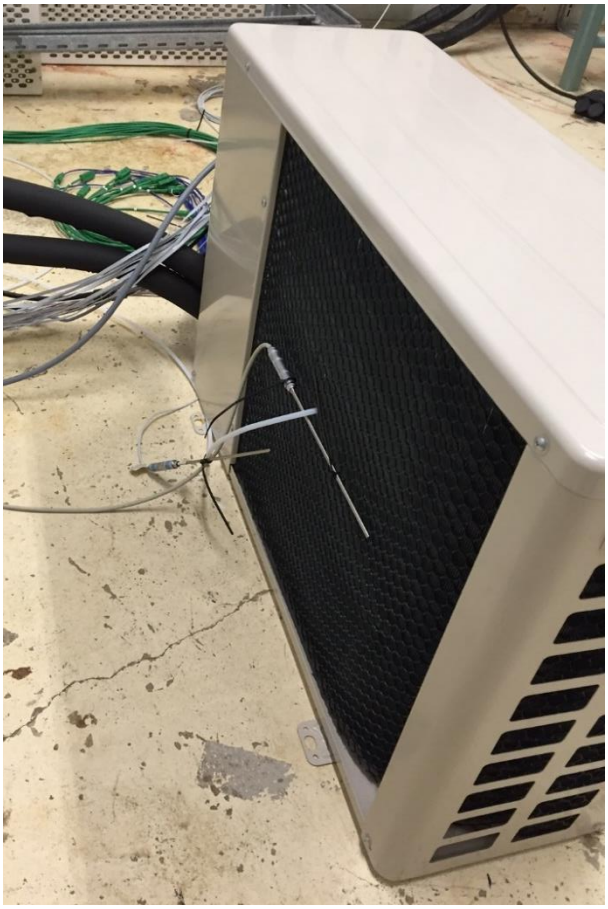

Figure 5.8. *Temperature sensor (PT100) used to measure the evaporator inlet air, i.e.* T_{ext}

Figure 5.9 is a schematic of the P-h diagram (a) and experimental refrigeration cycle (b) with the locations of the measured variables (excluding the T_{air1}-T_{air7} sensors).

The prototype along with its instrumentation is a good representation of on-field installations. The only exception is the fact that the compressor does not have an insulation layer around it; in most residential applications there is an insulation material covering the shell.

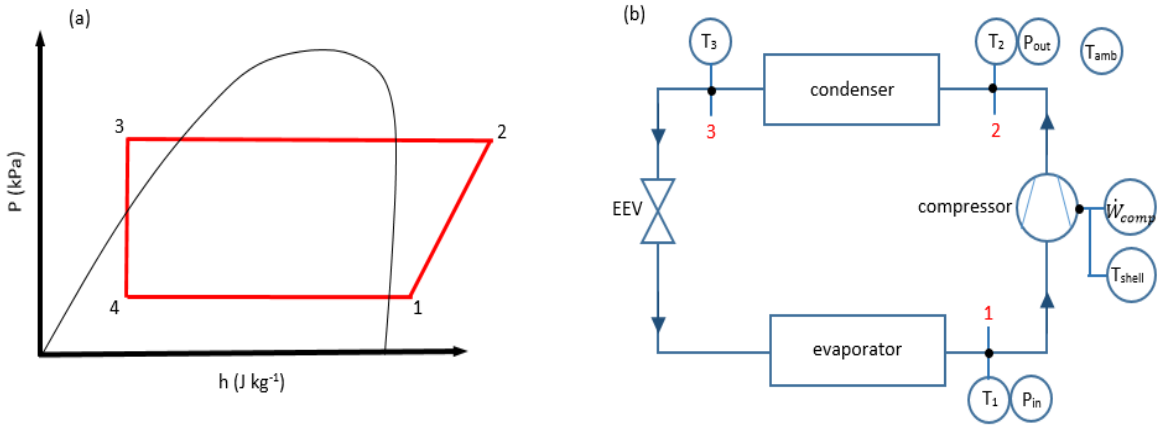

Figure 5.9. *Refrigeration cycle P-h diagram (a) and a schematic with required measurements (b) for the experimental validation of the performance assessment method*

5.4 Comparison of proposed performance assessment method with reference method

As mentioned in Chapter 4, compressor heat losses in rotary compressors are calculated from the following equation:

$$\dot{Q}_{amb} = \left(\frac{\overline{Nu}_L k}{L} A_L + \frac{\overline{Nu}_{D,1} k}{D} A_D + \frac{\overline{Nu}_{D,2} k}{D} A_D\right)\left(T_{shell,3} - T_{amb}\right) + \sigma A_{tot}\left(T_{shell,3}^4 - T_{amb}^4\right) \quad (5.1)$$

The average Nusselt number for the lateral side, $\overline{Nu}_L$, is obtained from the following equation for laminar flows:

$$\overline{Nu}_L = 0.68 + \frac{0.67 Ra_L^{1/4}}{(1 + (0.492/Pr)^{9/16})^{4/9}} \qquad (Ra_L \leq 10^9) \qquad (5.2)$$

and for turbulent flows from the following equation:

$$\overline{Nu}_L = \left(0.825 + \frac{0.387 Ra_L^{1/6}}{(1 + (0.492/Pr)^{9/16})^{8/27}}\right)^2 \qquad (10^9 \leq Ra_L \leq 10^{12}) \qquad (5.3)$$

The average Nusselt number for the top surface, $\overline{Nu}_{D,1}$, in laminar flows is calculated as follows:

$$\overline{Nu}_{D,1} = 0.54 Ra_D^{1/4} \qquad (10^5 < Ra_D \leq 10^7) \qquad (5.4)$$

and in turbulent flows:

$$\overline{Nu}_{D,1} = 0.14 Ra_D^{1/3} \qquad (10^7 < Ra_D < 3 \cdot 10^{10}) \qquad (5.5)$$

Finally, the average Nusselt number for the bottom surface, $\overline{Nu}_{D,2}$, is calculated as follows for both laminar and turbulent regimes:

$$\overline{Nu}_{D,2} = 0.82 Ra_D^{1/5} \qquad (10^5 < Ra_L < 10^{10}) \qquad (5.6)$$

5.4.1 Reference heating capacities

The heating capacity is calculated with the performance measurement method that integrates the new methodology to evaluate rotary compressor heat losses, presented in Eq. (**5.1**). A reference heating capacity value, $\dot{Q}_{cond}^{ref}$, represents the heat that is released by the condenser to the water, calculated from an energy balance equation on the water side, as follows:

$$\dot{Q}_{cond}^{ref} = \dot{m}_w c_{p,w} \left(T_{w,o} - T_{w,i} \right) \qquad (5.7)$$

where $T_{w,i}$ and $T_{w,o}$ is the water inlet and outlet temperatures, respectively, $\dot{m}_w$ is the water mass flow rate measured by an electromagnetic flow meter, and $c_{p,w}$ is the specific heat capacity of water.

The RMS error of the heating capacity calculated from the performance measurement method, which integrates the new compressor heat loss evaluation method, from the reference values is calculated. The deviations between $\dot{Q}_{cond}$ and $\dot{Q}_{cond}^{ref}$ are investigated as a function of compressor speed, compressor power input, evaporation temperature, and shell and ambient temperature difference.

5.4.2 Additional factors influencing the results of the method

The influence of various ambient sensor locations on the discrepancies between $\dot{Q}_{cond}$ and $\dot{Q}_{cond}^{ref}$ in terms of RMS errors can be investigated. Based on the obtained information the best location of the ambient sensor is then chosen.

In hermetic compressors, lubricating oil is in contact with the refrigerant and a fraction of it migrates along with the refrigerant through the cycle. It is difficult and inconvenient to measure precisely the oil mass fraction, C_g, with respect to the working fluid flow in real-time operating conditions. According, to Tran *et al.* (2012), C_g is assumed

to be constant and known, and equal to 2%. The influence of different oil concentration (OC) values is also investigated.

5.4.3 Comparison with other heat loss values

The results obtained when integrating the new heat loss calculation method defined in Eq.(**5.1**) for rotary compressors are compared to the results obtained with the one defined in the work of Tran *et al.* (2013), Eq. (**1.19**) in various operating conditions. Tran *et al.* (2013) estimated that T_{shell} was considered to be equal to the refrigerant temperature at discharge and the average h_c was 6.67 W K^{-1} m^{-2}. The latter value was calculated considering different ambient and refrigerant discharge temperatures to obtain a range of h_c values, from which an average was then taken. Nusselt number correlations suggested for isothermal cylinders (Morgan's correlation) and for hot surface facing up and down (McAdams' correlations) were used to calculate h_c.

Reference compressor heat loss values, $\dot{Q}_{amb}^{ref}$, were calculated from compressor energy balance:

$$\dot{Q}_{amb}^{ref} = \dot{W}_{comp} - \dot{m}^{ref}\left[\left(1-C_g\right)\left(h_{r,comp,out}-h_{r,comp,in}\right)+C_g\Delta h_o^{T_{comp,out}-T_{comp,in}}\right] \quad (5.8)$$

where $\dot{m}^{ref}$ is the refrigerant mass flow rate measured during the experiments from the condenser and water-side energy balance, as follows:

$$\dot{m}^{ref} = \frac{\dot{Q}_{cond}^{ref}}{\left(1-C_g\right)\left(h_{r,cond,i}-h_{r,cond,o}\right)+C_g\Delta h_o^{T_{cond,o}-T_{cond,i}}} \quad (5.9)$$

The RMS error between $\dot{Q}_{amb}^{ref}$ and $\dot{Q}_{amb}$ can be used as the absolute uncertainty of $\dot{Q}_{amb}$ in the uncertainty analysis used to determine the sensitivity index of the compressor heat losses in the final uncertainties of heating capacities obtained with the performance assessment method.

5.4.4 Operating conditions

The energy balances used in the performance assessment method are time-independent. Therefore, they are only applicable in steady-state conditions. In order to ensure steady-state conditions during tests, the following criteria are followed:

- acquisition period of measurement data of at least two hours,
- standard deviations of ambient temperature must be below 0.3 ℃,
- standard deviations of compressor shell and discharge temperatures must be below 0.3 ℃,
- standard deviation of superheat must be below 1 ℃.

Various operating conditions are tested depicted in Table 5.2. Evaporation and condensation temperature, ambient temperature, and compressor speed vary in different operating conditions.

Table 5.2. *Operating conditions tested in the experimental test bench*

Operating condition	T_{amb} (°C)	T_{evap} (°C)	T_{cond} (°C)	speed (rps)
1	5.8	1.0	40.0	30
2	9.0	0.5	40.0	60
3	12.7	0.0	41.0	90
4	3.7	1.0	60.0	30
5	7.7	2.0	60.0	60
6	12.4	1.0	60.0	90

5.5 Uncertainty values analysis

Uncertainties of the measured variables (sensor uncertainties) required in the calculations described in Section 5.4 are shown in Table 5.3.

Table 5.3. *Sensors used in measurements and their respective uncertainties*

Variable	Uncertainty
$\dot{W}_{comp}$	0.2-0.5 %
T_1	0.8 °C
T_2	0.8 °C
T_3	0.8 °C
T_{shell}	0.2 °C
T_{ext}	0.8 °C
P_{in}	0.25 %
P_{out}	0.25 %
$T_{w,i}$	0.2 °C
$T_{w,o}$	0.2 °C
$\dot{V}_w$	0.5 %

Although the measurement uncertainty of temperature sensors (T_1-T_3) was 0.2 °C, it is in fact the pipe surface temperature and not the direct measurement of the fluid inside the pipe. Thus, the uncertainty was expanded to 0.8 °C (Tran, 2012). The uncertainty of the exterior air temperature is 0.8 °C including the heterogeneity of air temperature. The uncertainty of wattmeter varied depending on the frequency: 0.2 %, 0.4 %, and 0.5 % for 30, 60, and 90 rps, respectively.

A measurement of the exterior temperature is performed also with a PT100 temperature sensor located at the center of outdoor unit fan at the air inlet side. The uncertainty introduced by the data acquisition system was included in the uncertainties. Refrigerant pressures were measured at the compressor inlet and outlet.

In some cases a required variable, *Y*, for instance, heating capacity in our case, cannot be measured directly, but is rather calculated as a function of one or more variables, *i.e.* $Y = f(X_1, X_2, \dots)$. Each of the measured variables, X_1, X_2, *etc.*, have an associated random variability. This variability is referred to as the uncertainty of each measured variable. In order to quantify the final uncertainty of the calculated value, *Y*, it must be calculated how the uncertainties in each of the measured variables propagate into the value of *Y*. The standard method described in NIST Technical Note 1297 was used to determine the propagation of uncertainties (Taylor & Kuyatt, 1994). The method assumes that individual measurements are uncorrelated and random. The final uncertainty in the calculated value *Y* can be calculated as follows:

$$\sigma_Y = \sqrt{\sum_i \left(\frac{\delta Y}{\delta X_i}\right)^2 \sigma_{X_i}^2} \qquad (5.10)$$

where σ_{X_i} is the absolute uncertainty of each measured quantity.

The sensitivity index of the variable with respect to the calculated variable is calculated as listed below:

$$S_i = \frac{\left(\frac{\delta Y}{\delta X_i}\right)^2 \sigma_{X_i}^2}{\sigma_Y^2} \qquad (5.11)$$

The sum of all sensitivity indices is equal to unity.

5.6 Results of on-field performance assessment method

As discussed above, the compressor integrated in the air-to-water prototype was the same as the one used in rotary compressor test bench described in Chapter 3. During the compressor test bench, an oil separator was used to separate oil from the refrigerant. The mass flow rate of the working fluid (mix of oil and refrigerant) before passing the oil separator was measured. After oil was separated from the refrigerant, the refrigerant mass flow rate was measured again. Thus, C_g levels were measured during this test bench. These measured values are referred to as experimental C_g values. It was noticed that the oil concentration (OC) was very small, much smaller than the value taken by Tran *et al.* (2013), where $C_g = 2$ %. It was also noticed that OC is not constant and depends primarily on the compressor speed.

Since the compressor used in the prototype is the same, it was assumed that the C_g values are identical at corresponding speeds. Unless otherwise mentioned, heating capacities are calculated with the experimental C_g values.

The RMS errors and deviations of heating capacities from the reference values are presented in Figure 5.10 and Figure 5.11, respectively, where compressor heat losses are calculated with using different ambient temperature sensors. The location of the ambient temperature sensors is illustrated in Figure 5.7 and Figure 5.8

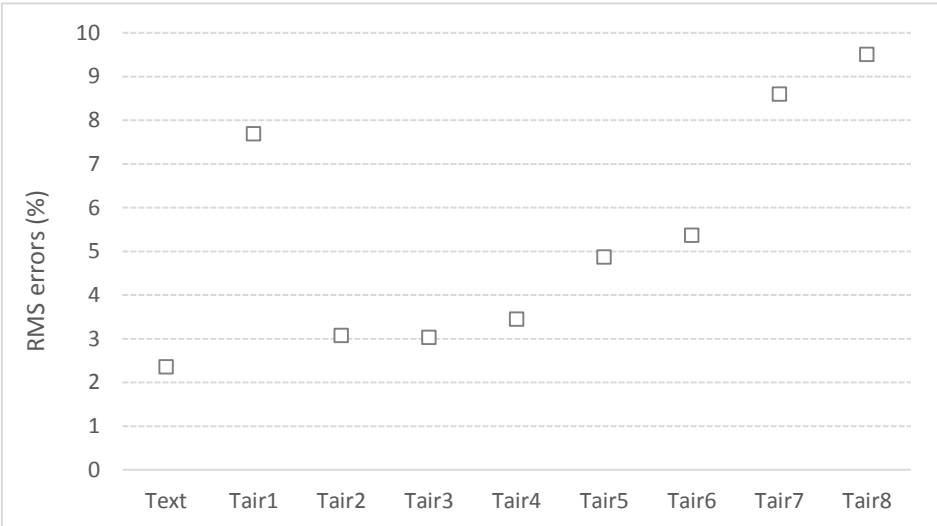

Figure 5.10. *Root mean square errors of the estimated heating capacities when* $\dot{Q}_{amb}$ *is obtained using different air temperature sensors*

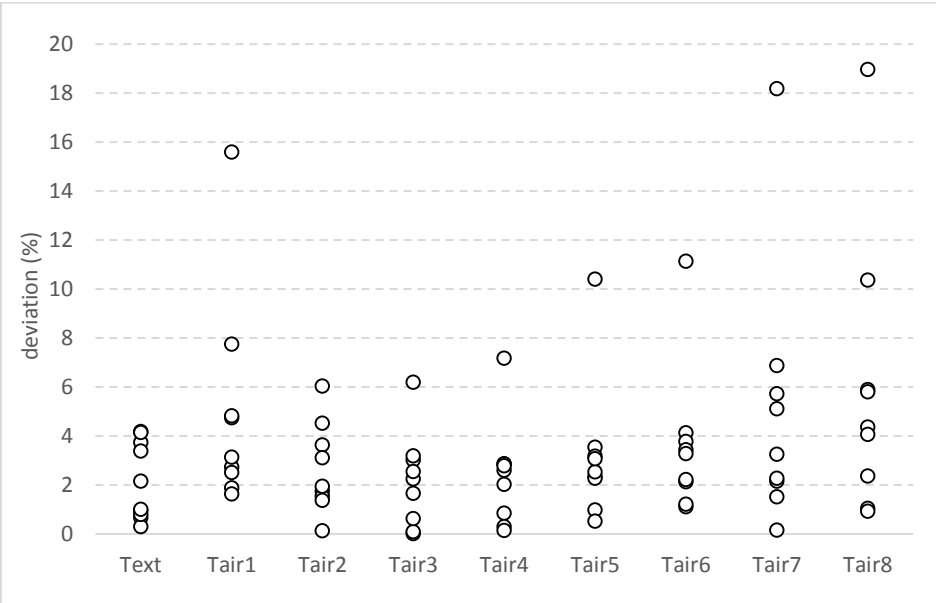

Figure 5.11. *Deviations of heating capacities from reference values when* $\dot{Q}_{amb}$ *is obtained using different air temperature sensors*

It can be seen that when T_{amb} is measured from the exterior air, T_{ext} sensor, it yields the smallest discrepancies between $\dot{Q}_{cond}$ and $\dot{Q}_{cond}^{ref}$. Based on this information it can be concluded that the temperature of the exterior air is the most optimal in terms of accuracy and also in terms of cost and installation facility, since no additional temperature sensor is required for this measurement; temperature measurements of exterior air are already installed in heat pump units.

Heating capacities were calculated from the performance measurement method that integrated the previous methodology used to calculate compressor heat losses defined by Tran *et al.* (2013), at various operating conditions. The deviations of these values were compared to the ones obtained from the method that integrated improved $\dot{Q}_{amb}$ evaluation method, shown in Figure 5.12.

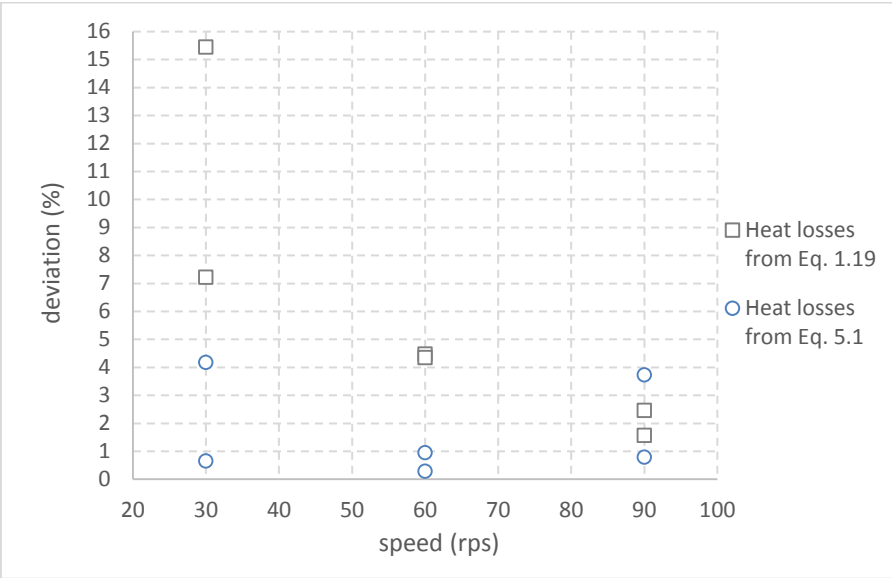

Figure 5.12. *Deviations of heating capacities calculated using the previosuly defined* $\dot{Q}_{amb}$ *evaluation method and the more accurate method from the reference values as a function of compressor speeds*

The RMS error of the heating capacities calculated with $\dot{Q}_{amb}$ from Eq. (**1.19**) is **7.51 %** as opposed to RMS error of **2.36 %** calculated using $\dot{Q}_{amb}$ from Eq. (**5.1**). Exterior air temperature measurement was used for T_{amb}. It was noticed that as the compressor speed increases, the deviations in the old method decrease. As the speed increases, the compressor power input increases significantly, thus weighting more in the compressor energy balance equation, Eq. (**1.9**), and the error introduced by inaccurate heat loss estimation becomes less significant.

Observing the experimental OC values, an approximation of $C_g = 0.5\,\% \pm 100\,\%$ seems to be more reasonable. Heating capacities calculated with experimental C_g values, $C_g = 2\,\%$, and $C_g = 0.5\,\%$ were compared to reference heating capacities in Figure 5.13. In these calculations ambient heat losses were evaluated with the new method.

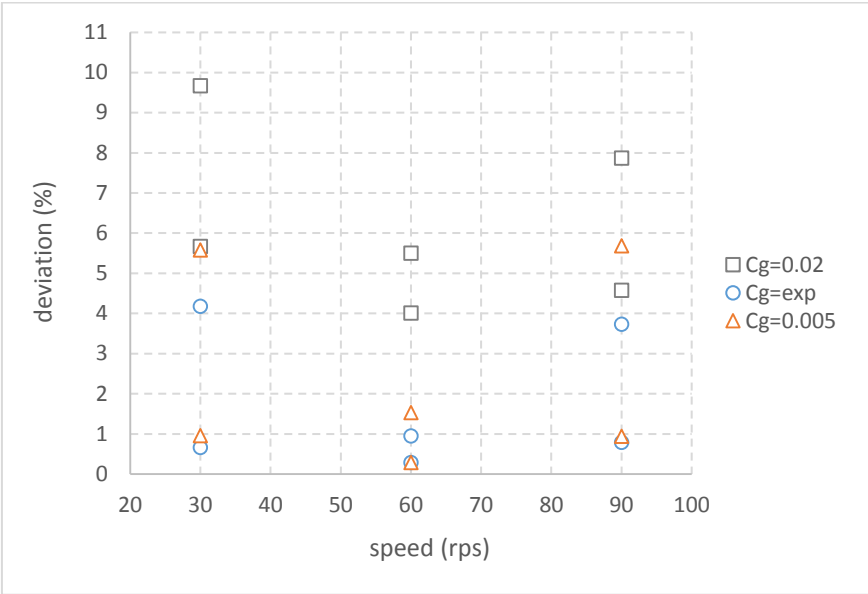

Figure 5.13. *Comparison of heating capacities deviations from the reference values with different* $\boldsymbol{C_g}$ *values*

The RMS error of experimental C_g values, which varied specifically with different compressor speeds, was the smallest in comparison with $C_g = 2$ % and $C_g = 0.5$ % that yielded a RMS errors of 6.52 % and 3.36 %, respectively. Therefore, assuming that the oil mass fraction is constant and equal to 0.5 % gives more accurate performance values than assuming that the oil mass fraction is equal to 2 %.

Optimal instrumentation to accurately measure compressor heat losses on-field is schematically illustrated in Figure 5.14. Figure 5.15 compares reference heating capacities with calculated heating capacities. Reference values include relative uncertainties obtained from the error propagation formula, Eq. (**5.10**).

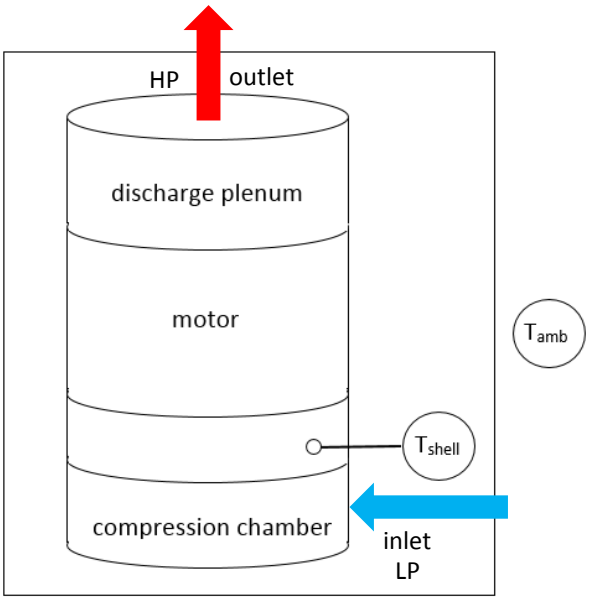

Figure 5.14. *Required instrumentation to measure rotary compressor heat losses on-field*

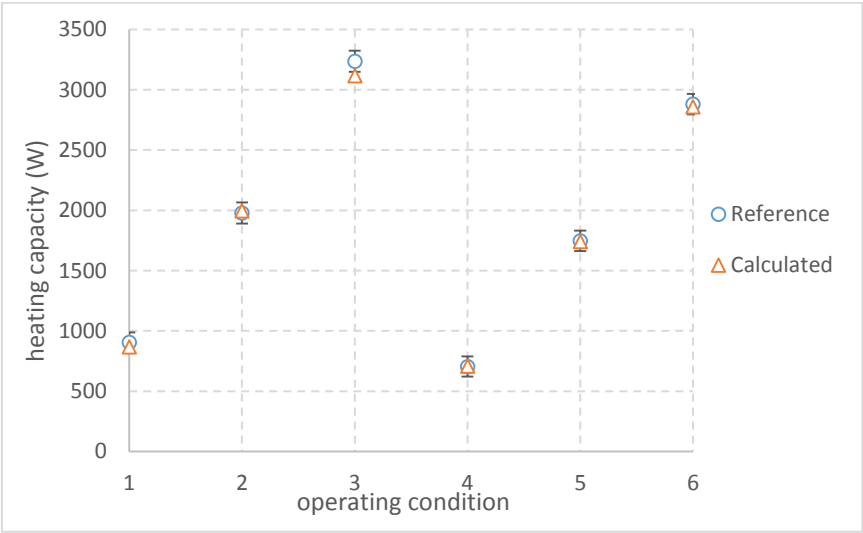

Figure 5.15. *Reference and calculated heating capacities at different operating conditions*

Compressor heat losses calculated from the new heat loss evaluation method, Eq. (**5.1**), old heat loss evaluation method, Eq. (**1.19**), and $\dot{Q}_{amb}^{ref}$ values in different operating conditions (Table 5.2) are presented in Figure 5.16. Reference values of compressor

heat losses, $\dot{Q}_{amb}^{ref}$, were calculated using the refrigerant mass flow rate obtained from the condenser and water-side energy balances, Eqs. (**5.8**) and (**5.9**).

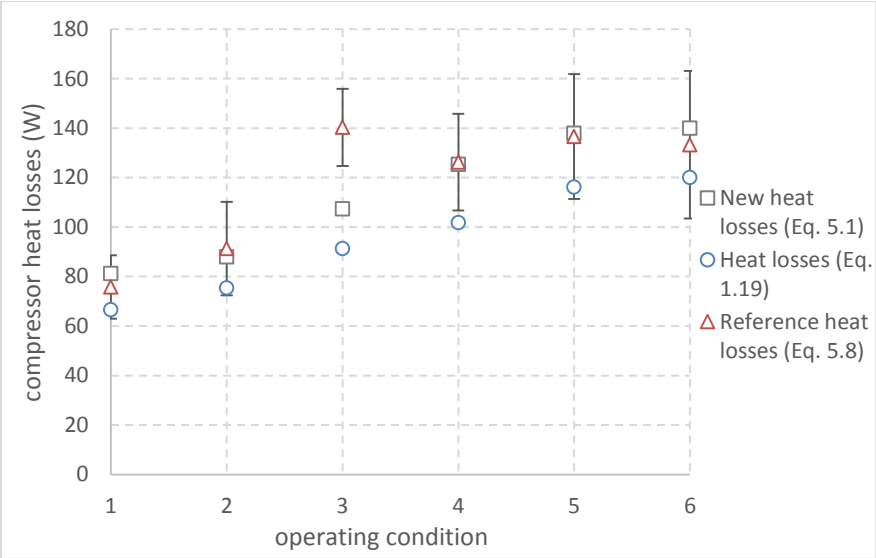

Figure 5.16. *Compressor heat losses calculated from the new heat loss evaluation method, Eq. (5.1), old heat loss evaluation method, Eq. (1.19) and reference values Eq. (5.8) in tested operating conditions*

The RMS error of heat losses from the improved heat loss evaluation method, Eq. (**5.1**), was 10.4 % and the RMS error of the previously defined heat loss evaluation method, Eq. (**1.19**), was 19.9 %.

Assuming that the relative uncertainty of compressor heat losses is the RMS error, *i.e.* 10.4 %, and taking experimental OC values, an uncertainty analysis shows that the **average sensitivity index of the improved compressor heat losses is 27 %**. Table 5.4 shows the sensitivity indices of each variable in the uncertainty of the heating capacity calculated. The oil mass fraction in the uncertainty analysis was equal to 0.02 ± 0.02, the same as in the analysis of Tran *et al.* (2013), which determined that the sensitivity index of compressor heat losses in the final uncertainty was 40 %.

Table 5.4 *Sensitivity index of each variable in the final uncertainty of the calculated heating power in operating condition 6*

Variable	Relative/absolute uncertainty	Sensitivity index (%)
$\dot{W}_{comp}$	0.5 %	0.87
C_g	2.0 %	62.25
T_1	0.8 °C	4.21
T_2	0.8 °C	3.40
T_3	0.8 °C	1.22
P_{in}	0.25 %	0.00
P_{out}	0.25 %	0.02
$\dot{Q}_{amb}$	10.4 %	28.03

The deviations in heating capacity calculated with the performance assessment method, where compressor heat losses were obtained from the new evaluation method, Eq. (**5.1**), are presented in Figure 5.17 as a function of compressor speed, in Figure 5.18 as a function of compressor power input, in Figure 5.19 as a function of evaporation pressure, and in Figure 5.20 as a function of temperature difference between the shell temperature sensor at the level between the compression chamber and the motor (sensor number 3, Figure 3.2 (b)) and the exterior air temperature.

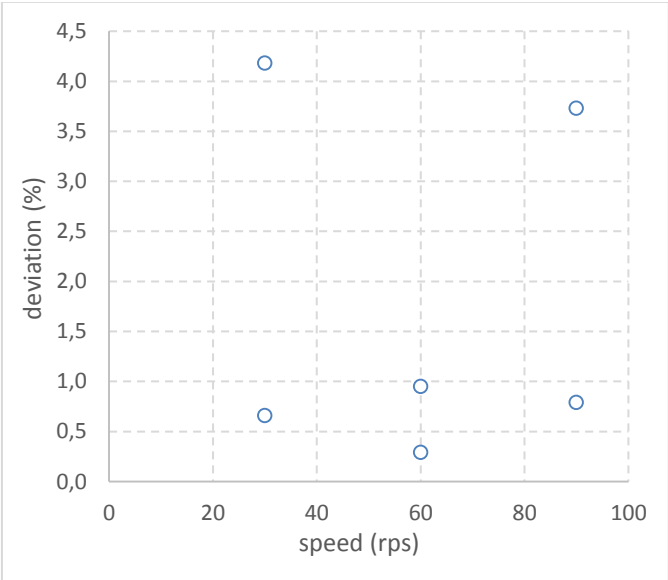

Figure 5.17. *Deviations in heating capacities from reference values as a function of compressor speed*

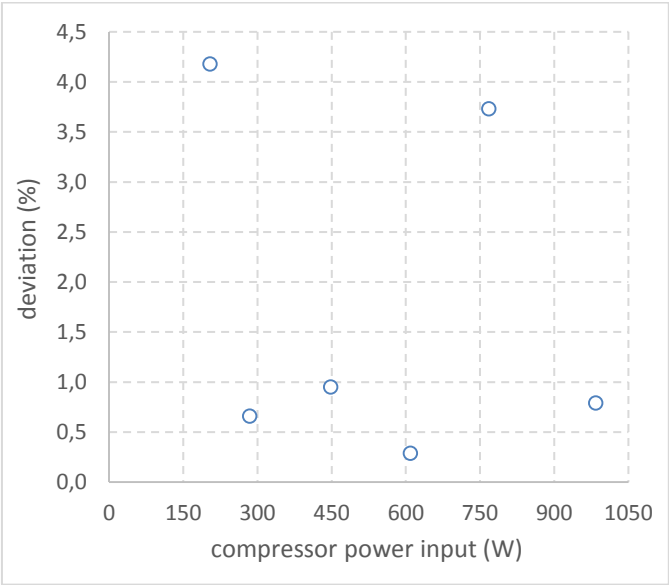

Figure 5.18. *Deviations in heating capacities from reference values as a function of compressor power input*

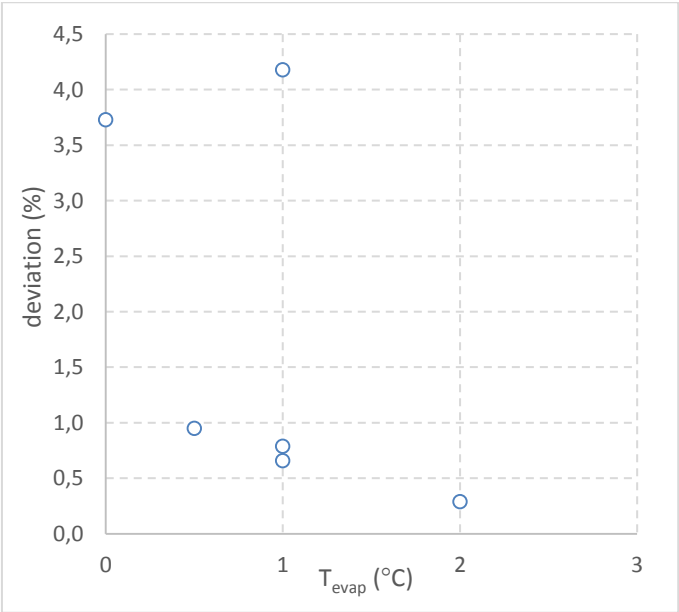

Figure 5.19. *Deviations in heating capacities from reference values as a function of evaporation temperature*

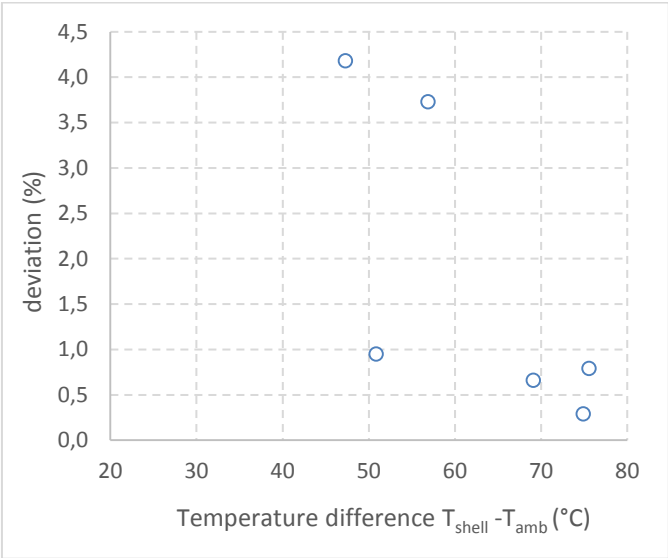

Figure 5.20. *Deviations in heating capacities from reference values as a function of temperature difference between compressor shell and ambient temperatures*

The parametric study shows that there are no particular tendencies when the deviations are plotted as a function compressor speed, power input, and evaporation temperature.

To conclude, based on the information presented above, the criteria to obtain the most accurate results when using the performance assessment method to calculate HP performances are:

- T_{shell} at the level the space between the compression chamber and the bottom of the motor (sensor 3 in Figure 3.2 (b)),
- T_{amb} can be evaluated from the exterior air temperature, for instance, measured at the evaporator inlet,
- $C_g = 0.5$ %,
- steady-state operating conditions.

These criteria are valid for air-to-air and air-to-water HPs that comprise a rotary compressor. Steady-state conditions exclude conditions, where the process variables fluctuate in respect to time. Such operating conditions are, for instance, startup and defrosting periods.

5.7 Conclusions

The aim of the experimental test bench was to validate the performance assessment method that integrated an improved heat loss evaluation method defined in Section 4.3 of Chapter 4 for rotary compressors. For this purpose an air-to-water HP prototype was

built and tested in various operating conditions. The prototype consisted of an exterior unit, which comprised a compressor, EEV, and evaporator, and a fan, and was installed in a climatic chamber. The interior unit comprised a condenser connected to a water loop. The water circuit was coupled with a water tank. All of the mentioned components were installed in another room. And, finally, the water inlet temperature was regulated by a thermal regulator installed in a third room. The reference heating capacity values were calculated from the water side measurements. The compressor used in the tests was a rotary compressor, the same as the one used in the test bench presented in Chapter 3.

The RMS error of the improved performance assessment method is 2.36 % from the reference heating capacity values. This is an improvement when compared to the RMS error obtained from the performance assessment method that integrated the previously defined heat loss evaluation method, described by Tran *et al.* (2013), which is 7.51 %.

The influence of different locations to measure the ambient temperature was investigated. It was concluded that measuring the exterior temperature (outside the exterior unit envelope), for instance, at the evaporator inlet, yields the best results in terms of accuracy and practicality. This location to measure ambient temperature offers more flexibility for adaptation to various HP systems, since it is insensitive to different configurations of internal components inside the exterior unit. In other words, as the component layout inside the exterior unit may change, the ambient sensor located, for instance, on the metal sheet separating the compressor from the evaporator (T_{air2}) may measure temperatures inferior or superior to the ones measured by T_{air2} during the tests on the air-to-water prototype, and may no longer be an accurate representation of air temperature surrounding the compressor. In addition, the chosen location will not require an additional sensor, since the evaporator inlet temperature is, typically, measured by default.

It was also concluded that oil mass fraction of 2 % contributes greatly to the deviations between the heating capacities. A constant oil mass fraction value of 0.5 %, derived from the OC measurements during the experimental test benches described in Chapter 3, yields more accurate results.

The improved heat loss evaluation method needs to be validated also in scroll compressors, which requires the use of Eq. (**4.14**), defined in Section 4.3. Also, as mentioned previously, the energy balances employed in the performance assessment method require steady-state conditions. The error introduced by the method when the operating mode is in unsteady-state conditions should also be evaluated.

The optimal instrumentation used to determine T_{shell} and, thus, allowing a more accurate heat loss estimation of rotary and scroll compressor on-field, is presented in Table 5.5.

Table 5.5. *Optimal instrumentation used to determine T_{shell} in scroll and rotary compressors*

Compressor	Number	Location (internal component level)	Additional information
Scroll	2	discharge plenum (sensor 6, Fig. 3.2 (a))	A correlation for the ratio of HP losses to the total shell losses (Eq. (**4.12**)) must be used to account for the total heat flux area. Correlation is valid if $T_{shell,LP} > T_{amb}$.
		middle of the motor (sensor 3, Fig. 3.2 (a))	Used to measure $T_{shell,LP}$.
Rotary	1	between the compression chamber and motor bottom (sensor 3, Fig. 3.2 (b))	Represents the best the area-weighted average of T_{shell} calculated by the numerical model.

CONCLUSIONS AND PERSPECTIVES

L'objectif de cette thèse a été de déterminer une approche plus précise pour évaluer les pertes thermiques sur site. Pour cette raison, deux modèles numériques, pour les compresseurs scroll et rotary, ont été développés afin d'investiguer les profils thermiques et la distribution de flux de chaleur sur les enveloppes des compresseurs, pour différents points de fonctionnement.

La méthode de mesure des performances intégrant la nouvelle approche pour évaluer les pertes thermiques est validée expérimentalement pour le cas d'une PAC air-eau équipée d'un compresseur rotary, pour plusieurs points de fonctionnement. Cette méthode améliorée présente une erreur quadratique de 2.36 % par rapport aux valeurs de puissance calorifique de référence, alors que la méthode précédente présente une erreur de 7.51 %.

Les perspectives de travail concernant les modèles numériques, la méthode de mesure des performances et la méthode de détection et de diagnostic de défauts sont également évoquées.

.

Conclusions

Heat pumps exhibit a high theoretical efficiency in residential applications. Their development is, therefore, important when attempting to reduce heating energy consumption in dwellings. However, HP performance values established in controlled laboratory conditions may vary from the ones obtained on-field due to several factors, such as controls, oversizing, faults, different temperature and flow set points, and climatic conditions. Real-time on-field performance evaluation provides more reliable data. Nevertheless, measuring accurately on-field heating capacity and coefficient of performance (COP) of HPs is difficult, particularly, of air-to-air HPs, since measuring air enthalpies and specifically air mass flow rate on-field is challenging.

A promising method for measuring heat pump performances on-field has been previously developed and published. The method is based on refrigerant fluid measurements and component energy/mass balances. Nonintrusive sensors, such as surface temperature sensors, are used to estimate pressure and refrigerant mass flow rate in different types of heat pump systems, including air-to-air.

The accuracy of the method is strongly dependent on the evaluation of heat transfer from compressor towards the ambient air, *i.e.* compressor heat losses. It was stated in the work of Tran *et al.* (2013) that the sensitivity index of heat losses in the relative uncertainty of heating capacity predicted by the method is 40 %. For this reason, the objective of this work was to develop an embarked method to evaluate more accurately compressor heat losses on-field.

One of the main simplifications of the previously defined method used to estimate compressor heat losses is the fact that the compressor shell is assumed to be isothermal and equal to the refrigerant discharge temperature. In order to investigate whether the shell is indeed isothermal and whether its temperature is equal to refrigerant temperature at discharge, numerical models for scroll and rotary compressors were developed and experimentally validated in this work.

The numerical models are based on hybrid modeling approach, which combines integral and differential formulations. The calculation procedure in the scroll and rotary models is divided in three fundamental steps: thermodynamic compression cycle analysis, detailed thermophysical flow analysis executed with the aid of a CFD program, and a compressor network analysis. The first step of the model evaluates the initial and boundary conditions used in integral and differential parts of the model, steps two and three, respectively. The second step of the model uses a CFD program and the outputs are transmitted to the final step of the model. A thermal network analysis verifies the validity of the results obtained from the CFD simulations, and determines whether the model can be considered globally converged in the third step of the model.

Experimental validation of the numerical models determined the RMS errors of the dimensionless temperature values of external thermal profiles: 0.04-0.08 and 0.03-0.05 in scroll and rotary compressors, respectively.

The location of the necessary temperature sensors that best represent T_{shell} of scroll and rotary compressors and zones, which contribute most to the heat losses, were determined with the aid of the numerical models. The simulation results showed that the shell of rotary compressor is relatively uniform, unlike in the case of scroll compressor, where a strong temperature jump at the level of compression chamber suggests that an important share of heat losses occur in the high pressure part. In fact, approximately 80 % of the heat losses in scroll compressors occurred in the high pressure part in tested conditions. For this reason, heat losses from the high pressure part of scroll compressor are evaluated.

The required instrumentation to determine T_{shell} in scroll compressors is:

- one sensor at the level of discharge plenum and one sensor at the level of the middle of the motor,
- two sensors required in total.

Similarly, the required instrumentation to determine compressor shell temperature in rotary compressors is:

- temperature sensor at the level of the space between the compression chamber and motor bottom,
- one sensor required.

In addition, the correlations used to calculate heat transfer coefficients in natural convection regime for top, bottom, and lateral compressor surfaces were selected for the embarked compressor heat loss evaluation.

The improved compressor heat loss evaluation is then integrated in the performance assessment method. An air-to-water HP prototype was built and tested in various operating conditions to validate the performance assessment method that integrated an improved heat loss evaluation method rotary compressors, as the compressor of the HP prototype was of rotary type. The reference heating capacity values were calculated from the water side measurements. Experimental validation was also used to determine the most optimal location of the sensor used to measure the temperature of air surrounding the compressor, T_{amb}. Exterior air temperature measured, for instance, at the evaporator inlet, was chosen as the most appropriate representation of T_{amb}.

The improved performance value yielded a RMS error of 2.36 % from the reference values. The RMS error obtained from the performance assessment method that integrated the heat loss evaluation method presented in the work of Tran *et al.* (2013) was 7.51 %.

Perspectives

Suggestions for future work can be divided in three groups. One related to the numerical model, another related to the performance assessment method, and the third related to fault detection and diagnostics.

Numerical model

The model can be exploited to observe the behavior of exterior thermal profiles in a wider range of operating conditions. A matrix consisting of different ambient, condensation, and evaporation temperatures, compressor speeds combinations can be used for the purpose. Also, the influence of different insulation materials and their thicknesses can be investigated, as well as the influence of component dimensions and layout. The model can then be used to characterize scroll and rotary compressors of different sizes and to adapt the heat loss evaluation methods, described in Chapter 4, accordingly.

Performance assessment method

The improved heat loss evaluation method needs to be validated also in scroll compressors. The validation of the method in scroll compressors is, particularly, interesting since the scroll compressor shell is not isothermal; the proposition to measure the heat losses only from the high pressure part of the compressor must be tested.

The performance assessment method is applicable only in steady-state conditions since the energy balances that constitute the method are time-independent. It is interesting to test the validity of and the error introduced by the method in unsteady operating conditions, such as, startup and defrosting periods, where the measured variables fluctuate with time.

Fault detection and diagnostics

The method determines indirectly the refrigerant mass flow rate using the compressor energy balance. This information can be utilized for fault detection and diagnostics purposes. The method on its own provides means to optimize HP performance by providing real-time performance data in terms of COP and heating capacity. However, coupling the method with a fault detection and diagnostics method is of interest, since it can minimize performance degradation, maintenance costs, and machine down-time.

A fault detection and diagnostics method described by Li & Braun (2007) in Chapter 1 can be coupled with the performance assessment method. The most common residential HP faults, such as exchanger fouling and refrigerant overcharge and undercharge, and their detection methodology, could be tested and validated with the air-to-water prototype, described in Section 5.2. The capability of performance assessment method to perform on-field diagnostics can then be validated.

The fault detection and diagnostics method, presented in the work of Li & Braun (2007), compares the deviations between fault-free and faulty decoupling feature values (*e.g.* air mass flow rate at the evaporator side), which are calculated using the indirect evaluation of the refrigerant mass flow rate provided by the performance assessment method. Naturally, the uncertainty of the mass flow rate will influence the uncertainty of the calculated decoupling feature value. Therefore, if the uncertainty is significant, some faults may be falsely detected or ignored. However, since the improved compressor heat loss evaluation decreases noticeably the uncertainty of the performance assessment method, a more efficient fault detection could be enabled.

BIBLIOGRAPHY

Almbauer, R. A., Burgstaller, A., Abidin, Z., & Nagy, D. (2006). 3-Dimensional Simulation for Obtaining the Heat Transfer Correlations of a Thermal Network Calculation for a Hermetic Reciprocating Compressor. *Proc. of International Compressor Engineering Conference.* Purdue, USA.

Birari, Y. V., Gosavi, S. S., & Jorwekar, P. P. (2006). Use of CFD in design and development of R404a reciprocating compressor. *Proc. of International Compressor Engineering Conference.* Purdue, USA.

Bouafia, M., Bertin, Y., & Saulnier, J. B. (1988). Analyse expérimentale des transferts de chaleur en espace annulaire étroit et rainuré avec cylindre intérieur tournant. *Int. J. Heat Mass Transfer, 41,* 1279-1291.

Breuker, M. S., & Braun, J. E. (1998). Evaluating the performance of a fault detection and diagsnotic system for vapor compression equipment. *HVAC&R Research, 4,* 401-425.

Chen, Y., & Lan, L. (2009). A fault detection technique for air-source heat pump water chiller/heater. *Energy and Buildings, 41,* 881-887.

Chikurde, R. C., Loganathan, E., Dandekar, D. P., & Manivasagam, S. (2002). Thermal mapping of hermetically sealed compressors using computational fluid dynamics. *Proc. of International Compressor Engineering Conference.* Purdue, USA.

Churchill, S. W., & Bernstein, M. (1977). A correlating equation for forced convection from gases and liquids to a circular cylinder in crossflow. *J. Heat Transfer, 99,* 300-306.

Churchill, S. W., & Chu, S. H. (1975). Correlating equations for laminar and turbulent free convection from a vertical plate. *Int. J. Heat Mass Transfer, 18,* 1323-1329.

Conde, M. R. (1996). Estimation of thermophysical properties of lubricating oils and their solutions with refrigerants: An appraisal of existing methods. *Appl. Therm. Eng.,* 51-61.

COSTIC. (2004). *Pompes à chaleur en habitat individuel.* Projet EU-CERT.HP. AFPAC.

Cowan, A. (2004). Review of Recent Commerical Rooftop Unit Field Studies in the Pacific Northwest and California. *Northwest Power and Conservation Council and Regional Technical Forum.* Portland, Oregon.

Diniz, M. C., Perira, E. L., & Deschamps, C. J. (2015). A lumped-parameter thermal model for scroll compressors including the solution for the temperature distribution along the scroll wraps. *Int. J. Refrig., 53*, 184-194.

Downey, T., & Proctor, J. (2002). What can 13,000 air conditioners tell us? *ACEEE 2002 Summer Study on Energy Efficiency in Buildings. 1*, pp. 53-68. Washington D.C.: American Council for an Energy-Efficient Economy.

Duprez, M. E., Dumont, E., & Frère, M. (2010). Modeling of scroll compressor - improvements. *Int. J. Refrig., 33*, 721-728.

Dutra, T., & Dechamps, C. J. (2013). Experimental Characterization of Heat Transfer in the Components of a Small Hermetic Reciprocating Compresor. *Appl. Therm. Eng., 58*, 449-510.

Dutra, T., & Deschamps, C. J. (2013). Experimental Characterization of Heat Transfer in the Components of a Small Hermetic Reciprocating Compressor. *Applied Thermal Engineering, 58*, 499-510.

EN 14511. (2004). Air conditioners, liquid chilling packages and heat pumps with electrically driven compressors for space heating and cooling. European Committee for Standardization.

Ertesvåg, I. S. (2011). Uncertainties in heat pump coefficient of performance (COP) and exergy efficiency based on standardized testing. *Energy and Buildings, 43*, 1937-1946.

EU climate action - Climate Action - European Commission. (2017, May 03). Retrieved from Climate Action - European Commission: https://ec.europa.eu/clima/citizens/eu_en

Fahlén, P. (2004). Methods for commissioning and performance checking of heat pumps and refrigerant equipment. *Proc. IIR Conference Compressors 2004.* Castá Papiernicka, Slovakia.

French Environment and Energy Management Agency. (2014). *Chiffres-clés: climat, air, énergie.* Angers: ADEME.

Gnielinski, V. (1976). New equations for heat and mass transfer in turbulent pipe and channel flow. *Int. Chemical Engineering, 16*, 359-368.

Goossens, M., Rivière, P., Teuillieres, C., Tran, C. T., Cauret, O., & Marchio, D. (2016). Experimental validation of on-field measurement method for a heat pump system with internal heat exchanger. *Int. J. Air-Cond. and Refrig. , 24*(2), 1650011.

Heo, J., Jeong, W., Baek, C., & Kim, Y. (2011). Comparison of the heating performance of air-source heat pumps using various types of refrigerant injection. *Int. J. Refrig., 34*, 444-453.

Hirsch, C. (2007). *Numerical Computation of Internal & External Flows.* Oxford: John Wiley & Sons.

Ichikawa, T., Anna, W., & Satoshi, Y. (2007). Study on running performance of a split-type air conditioning system installed on a university campus in suburban Tokyo. *Proc. Climate 2007 WellBeing Indoors Congress.* Helsinki, Finland.

Incropera, F. P., & DeWitt, D. P. (2002). *Fundamentals of heat and mass transfer.* USA: John Wiley & Sons.

ISO 5151. (1994). Non-ducted air conditioners and heat pumps – Testing and rating for performance. International Organization for Standardization.

Jang, K., & Jeong, S. (2005). Experimental investigation on convective heat transfer mechanism in a scroll compressor. *International Journal of Refrigeration, 2006*, 744-753.

Kadambi, V., & Drake, R. M. (1960). *Free convection heat transfer from horizontal surfaces for prescribed variations in surface temperature and mass flow through the surface.* Technical Report, Mech. Eng. HT-1: Princeton University.

Kim, M.-H., & Bullard, C. W. (2002). Thermal performance analysis of small hermetic refrigeration and air-conditioning compressors. *JSME International Journal, 45*, 857-864.

Kim, W., & Braun, J. E. (2015). Extension of a virtual refrigerant charge sensor. *Int. J. Refrig., 55*, 224-235.

Kreith, F., Roberts, L. G., Sullivan, J. A., & Sinha, S. N. (1963). Convection heat transfer and flow phenomena of rotating spheres. *Int. J. Heat Mass Transfer, 6*, 881-895.

Lee, S. J., Shim, J., & Kim, K. C. (2016). Development of capacity modulation compressor based on a two stage rotary compressor. 2. Performance experiments and P–V analysis. *Int. J. Refrig., 61*, 82-99.

Li, D., Zhou, Y., Hu, G., & Spanos, C. (2016). Fault detection and diagnosis for building cooling system with a tree-structured learnign method. *Energy and Buildings, 127*, 540-551.

Li, H., & Braun, J. E. (2007). Decoupling features and virtual sensors for diagnosis of faults in vapor compression air conditioners. *Int. J. of Refrig., 30*, 546-564.

Li, H., & Braun, J. E. (2009). Decoupling features for diagnosis of reversing and check valve faults in heat pumps. *Int. J. Refrig, 32*, 316-326.

Li, W. (2013). Simplified steady-state modeling for variable speed compressor. *Appl. Therm. Eng., 50*, 318-326.

Liley, P., & Gambill, W. R. (1973). *Chemical Engineering Handbook.* New York: McGraw-Hill.

Madani, H. (2014). The common and costly faults in heat pump systems. *The 6th International Conference on Applied Energy - ICAE 2014* (pp. 1803-1806). Taipei City: Energy Procedia.

Madani, H., & Roccatello, E. (2014). A comprehensive study on the importnt faults in heat pump system during the warranty period. *Int. J. Refrig., 48*, 19-25.

McAdams, W. H. (1954). *Heat Transmission.* New York: McGraw-Hill.

McWilliams, J. (2002). Review of airflow measurement techniques. In *Contract for U.S Department of Energy.* Contract No. DEAC03e76SF00098.

Mills, A. F. (1999). *Basic Heat and Mass Transfer.* USA: Prentice Hall.

Ooi, K. T. (2003). Heat transfer study of a hermetic refrigeration compressor. *Appl. Therm. Eng., 23*, 1931-1945.

Padet, J. (2008). *Convection thermique et massique. Nombre de Nusselt: partie 1.* Techniques de l'ingénieur.

Padhy, S. K. (1992). Heat Transfer Model of a Rotary Compressor. *Proc. of International Compressor Engineering Conference*, (pp. 1405-1418). Purdue, USA.

Pereira, E. L., & Deschamps, C. J. (2012). A numerical study of convective heat transfer in the compression chambers of scroll compressors. *Proc. of International Compressor Engineering Conference.* Purdue, USA.

Petukhov, B. S. (1970). *Heat transfer and friction in turbulent pipe flow with variable physical properties* (Vol. 6). (J. P. Hartnett, & T. F. Irvine, Eds.) New York: Academic Press.

Raja, B., Lal, D., & Kalanidhi, A. (2003). A numerical model for thermal mapping in a hermetically sealed reciprocating compressor. *Int. J. Refrig., 26*, 652-658.

Ribas, F. A. (2007). Thermal analysis of reciprocating compressors. *Proc. of International Conference on Compressor and Their Systems*, (pp. 227-287). London, UK.

Ribas, F. A., Deschamps, C. J., Fagotti, F., Morriesen, A., & Dutra, T. (2008). Thermal analysis of reciprocating compressors - critical review. *Proc. of International Compressor Engineering Conference.* Purdue, USA.

Saleh, B., & Aly, A. A. (2016). Artificial neural network models for depicting mass flow rate R22, R407C and R410A through electronic expansion valve. *Int. J. Refrig., 63*, 113-124.

Sanvezzo, J., & Deschamps, C. J. (2012). A Heat Transfer Model Combining Differential and Integral Formulations for Thermal Analysis of Reciprocating Compressors. *Proc. of International Compressor Engineering Conference*, (pp. 1343, 1-10). Purdue, USA.

Scroll Compressor: SRL Series (Oil-Free Scroll Compressor) Features: Hitachi Industrial Equipment Systems. (2017, May 03). Retrieved from Hitachi-ies.co.jp: http://www.hitachi-ies.co.jp/english/products/air/scroll/features.htm

Sim, Y. H., Youn, Y., & Min, M. K. (2000). A study on heat transfer and performance analysis of hermetic reciprocating compressors for refrigerators. *Proc. of Ineternational Compressor Engineering Conference*, (pp. 229-236). Purdue, USA.

Singer, E., Tran, C. T., & Rivière, P. (2014). On-field measurement method of vapor injection heat pump system. *Int. J. Refrig., 41*, 147-156.

Taylor, B. N., & Kuyatt, C. E. (1994). Guidelines for Evaluating and Expressing the Uncertainty of NIST Measurement Results. In *Technical Note 1297*. National Institue of Standars and Technology.

Teodorese, V., Detroux, L., & Lebrun, J. (2007). *Testing of a Room Air Conditioner-High Class RAC Test Results-Medium Class RAC Test Results.* Liège: Université de Liège.

Todesca, M. L., Fagotti, F., Prata, A. T., & Ferreira, R. T. (1992). Thermal analysis in reciprocating hermetic compressors. *Proc. of International Compressor Engineering Conference*, (pp. 1417-1428). Purdue, USA.

Tran, C. T. (2012). *Méthodes de mesure in situ des performances annuelles des pompes à chaleur air/air résidentielles.* Paris: Mines ParisTech.

Tran, C. T., Rivière, P., Marchio, D., & Arzano-Daurelle, C. (2012). Refrigerant-based measurement method of heat pump seasonal performances. *Int. J. Refrig., 35*, 1583-1594.

Tran, C. T., Rivière, P., Marchio, D., & Arzano-Daurelle, C. (2013). In situ measurement methods of air to air heat pump performance. *Int. J. Refrig., 35*(5), 1442-1455.

White, F. (2005). *Viscous Fluid Flow*. New York: McGraw-Hill Science.

Wichman, A., & Braun, J. E. (2008). Fault detection and diagnostics for commercial coolers and freezers. *Proc. of International Refrigeration and Air Conditioning Conference.* Purdue, USA.

APPENDIX A

EXTENSION OF THE PERFORMANCE ASSESSMENT METHOD TO A FDD METHOD

A.1 Fault detection and diagnostic methods

There is a wide range of fault detection and diagnosis methods; from detailed physical models to simple polynomial black-box models. Each method shows advantages and disadvantages in terms of applicability of on-field implementation, cost, accuracy, and data required. Ideally, FDD methods utilize low cost sensors, such as temperature sensors, and preferably sensors that are already integrated in the machine or as little supplementary sensors as possible in order to keep the hardware costs at minimum. However, the diagnosis provided by the method must be reliable and of high quality. The FDD method must be applicable to a wide range of HP types and sizes, and must require low computational effort for on-field calculations.

Black-box models

Black-box models rely on statistical methods to establish a relationship used to determine whether a measured parameter indicates a fault and, thus, do not account for physical characteristics and phenomena of the system. For example, clustering algorithms based on fuzzy clustering or neural networks, designed to associate measured parameter values to corresponding faults, are used (Saleh & Aly, 2016). Black-box model can also be based on multivariate analysis technology, such as principle component analysis (PCA), which is used to transform a number of related variables to a smaller set of uncorrelated variables. This can then be used in parameter residual generation, where the discrepancies between the expected value and the measured value are used to detect and quantify a fault. An example of such FDD model for air-source heat pump water chillers/heaters is described and validated by Chen & Lan (2009).

Despite a great variety of black-box modeling approaches, some more optimized than others, they all have one important disadvantage in common: the need for a large database in order to learn machine operation. The database over a full-range of fault-free operating conditions that include summer and winter seasons. The learning period required for the database must be either executed in laboratory conditions, where different operating conditions will be simulated, or in already-installed machines, which is time consuming and cost-prohibiting. Furthermore, the algorithm will use this database that is machine specific to extract the required data concerning machine operation and is poorly adaptable directly to another machine, as it needs to go through a learning period again.

Fault-tree analysis

Fault-tree analysis is a deductive failure analysis that relies on Boolean algebra to determine all the possible event combinations that can potentially lead to undesirable consequences in the machine (Li *et al.*, 2016). The method, thus, establishes the cause

of a specific fault, as well as their probability, and can be generalized to various HP types. It is based on practical experience and expert opinion, reported during interventions. Therefore, the reliability and precision of the method depends on the quantity and quality of failure data available.

Physical models

Physical models, such as the model described in Wichman & Braun (2008); Li & Braun (2007); Li & Braun (2009), for commercial coolers and freezers, are based on studying the physical phenomena occurring in the system. Such models typically require real-time measurements of values that are characteristic to specific faults. These values are then compared to nominal or fault-free values typically provided from equipment manufacturers. Any discrepancies between the values indicate a fault.

Intrusive flow meters cannot be used in already-installed machines. For this reason, Li & Braun (2007) developed a decoupling-based diagnostic technique that relies on real-time indirect flow measurements, such as the one obtained from the performance measurement method. The method identifies diagnostic features that are decoupled, *i.e.* insensitive, to other faults and operating conditions. Quantities necessary to determine decoupling features rely on low-cost, non-intrusive measurements and physical models of components. In addition, the method can be extended to different vapor compression cycles, including HPs. Furthermore, it does not require extensive datasets for training. Low-cost implementation, robustness of the model, and the capability to handle multiple-simultaneous faults make the method perfectly suitable for on-field applications in already-installed machines. This particular FDD method and its possibility to adapt to air-to-air heat pumps is described in the following subsection.

A.2 Promising fault detection and diagnostic method

Real-time measurements performed by the performance assessment method can be coupled with some complementary measurements to constitute a practical and promising FDD tool, termed **decoupling-feature diagnostic method**, as presented in the work of Li & Braun (2007).

Most common faults occurring in residential HPs can be detected and distinguished with the proposed FDD method solely with the aid of non-intrusive low-cost sensors, particularly temperature sensors. The following list is an example of faults that can be analyzed with the decoupling feature-based diagnostic technique:

- refrigerant overcharge;
- refrigerant undercharge;
- evaporator fouling and
- condenser fouling.

These faults are the most common in residential HP applications. Furthermore, these faults are important and difficult to diagnose, and they impact the system's thermal capacity, efficiency and equipment life (Breuker & Braun, 1998).

The primary impact of **exchanger fouling** is a decrease in air flow. The decoupling feature for such fault is, therefore, volumetric air flow, determined with virtual sensors that employ energy balances of the air and refrigerant sides. This decoupling feature is strongly influenced by the level of fouling and fan problems. It is also independent of other faults occurring in the unit in systems that incorporate fixed-speed fans. It can also be used to diagnose exchanger fan problems. Conductance can also characterize exchanger fouling. However, it is less precise since it is not only representative of air-side fouling since it may depend on refrigerant flow parameters and characteristics. Air flow rate is, therefore, more representative of exchanger fouling, since it is decoupled from other faults.

Condenser fouling

Condenser fouling can be detected by employing a virtual air flow rate sensor that is obtained from a steady-state energy condenser energy balance including virtual pressure measurements from saturation temperatures and other temperature measurements, as depicted in the following equation:

$$\dot{V}_{ca} = \frac{\upsilon_{ca}}{c_{p,air}} \frac{\dot{m}\left(h_{cond,in} - h_{cond,out}\right)}{\left(T_{ca,out} - T_{ca,in}\right)} \qquad (A.1)$$

where $\dot{V}_{ca}$ is condenser air volume flow rate, υ_{ca} is condenser air specific volume, $c_{p,air}$ is the air specific heat, $T_{ca,in}$ and $T_{ca,out}$ are condenser inlet and outlet temperatures, $h_{cond,in}$ and $h_{cond,out}$ are refrigerant enthalpy at condenser inlet and outlet, respectively, estimated from condenser inlet and outlet pressures, respectively, and condenser inlet and outlet temperatures, respectively. The method requires refrigerant mass flow rate, which can be obtained from compressor energy balance depicted in Eq. (**1.10**). Thus, this diagnostic feature is coupled with the performance assessment method.

The obtained air flow rate is compared to a nominal air flow rate value estimated from condenser fan map. The change in physical properties of air can be considered negligible with the pressure drop across condenser coil due to fouling. Therefore, specific heat capacity of air evaluated at constant pressure is suitable to represent heat absorbed by the traversing air. Air absolute humidity is assumed to remain constant across the condenser. Figure A.1 is a flow chart representation of condenser fouling detection algorithm.

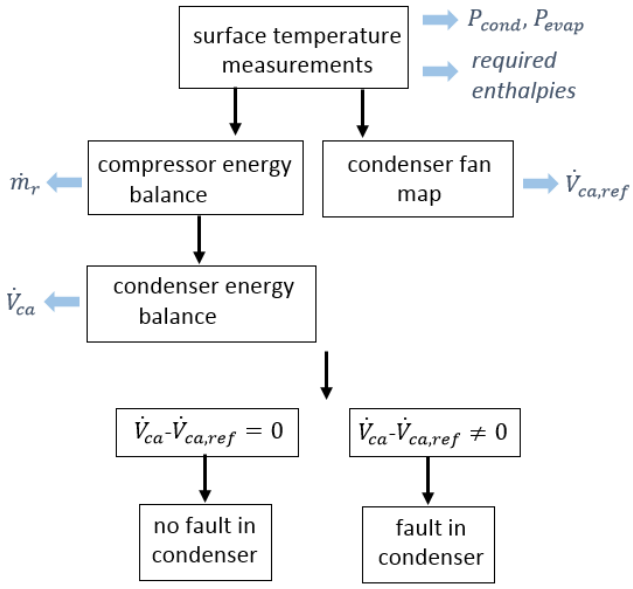

Figure A.1. *Flow chart diagram of condenser fouling detection algorithm*

<u>Evaporator fouling</u>

Similar to condenser fouling, the principle impact of **evaporator fouling** is decrease in air flow rate, which can be measured with a virtual sensor, as follows:

$$\dot{V}_{ea} = \frac{v_{ea}\dot{m}\left(h_{evap,out} - h_{evap,in}\right)}{\left(h_{ea,in} - h_{ea,out}\right)} \qquad (A.2)$$

where $\dot{V}_{ea}$ is evaporator air volume flow rate, and v_{ea} is evaporator air specific volume, $h_{evap,in}$ and $h_{evap,out}$ are refrigerant enthalpy at evaporator inlet and outlet, respectively, and $h_{ea,in}$ and $h_{ea,out}$ are air enthalpy at evaporator inlet and outlet, respectively. Relative humidity of evaporator inlet and outlet air must be known to obtain air enthalpies. However, in order to reduce on-field instrumentation and simplify the

measurements, the heat absorbed by the air can be estimated with the aid of specific heat capacity at constant pressure, as in the case of condenser, as listed below:

$$\dot{V}_{ea} = \frac{v_{ea}}{c_{p,air}} \frac{\dot{m}\left(h_{evap,out} - h_{evap,in}\right)}{\left(T_{ea,in} - T_{ea,out}\right)} \tag{A.3}$$

where $T_{ea,in}$ and $T_{ea,out}$ are evaporator inlet and outlet air temperatures.

Air flow rate measurement is compared to a nominal flow rate value estimated from evaporator fan map. Figure A.2 is a flow chart representation of evaporator fouling detection algorithm.

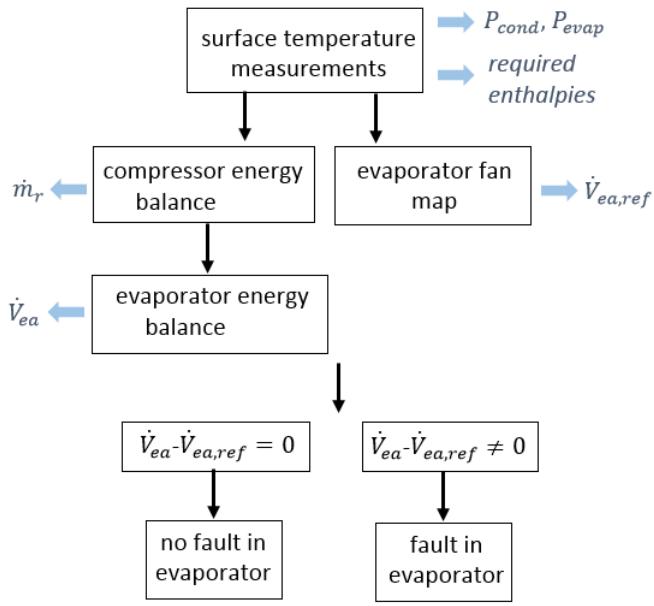

Figure A.2. *Flow chart diagram of evaporator fouling detection algorithm*

<u>Refrigerant undercharge/overcharge</u>

Refrigerant undercharge decreases the subcooling at the condenser exit, and when the unit is significantly undercharged the refrigerant may be in two-phase state in the liquid line. Refrigerant undercharge will provoke an increase in superheat. A thermostatic and electronic expansion valves will try to compensate and regulate this increase in superheat by lowering the evaporation pressure.

In case of a severe overcharge, the liquid line will become filled and refrigerant will start flowing back to the condenser, thus, deteriorating the thermal capacity due to

diminished exchange area (condenser is filled with more liquid). In such cases, subcooling will increase as well as the condensation pressure in order to compensate for the losses in thermal capacity.

Refrigerant overcharge or undercharge is a type of fault that has an impact on the whole system, and not just one single component, since it modifies multiple parameters in the system. For this reason, measuring the mass flow rate with a virtual sensor is not possible. The decoupling feature for refrigerant charge is calculated from the following equation:

$$\Delta T_{sc\rightarrow sh} = \left(T_{sc} - T_{sc,rated}\right) - \frac{k_{sh}}{k_{sc}}\left(T_{sh} - T_{sh,rated}\right) \qquad (A.4)$$

where k_{sh}/k_{sc} is a constant characteristic to a specific system and represents the slope of a straight line plot relating the superheat and subcooling in two operating conditions, as follows:

$$\frac{k_{sh}}{k_{sc}} = \frac{T_{sc,0} - T_{sc,rated}}{T_{sh,0} - T_{sh,rated}} \qquad (A.5)$$

where $T_{sh,rated}$ and $T_{sc,rated}$ is the superheat and subcooling at rated conditions, respectively, and $T_{sh,0}$ and $T_{sc,0}$ is the superheat and subcooling, respectively, at another fault-free operating condition; a change in the operating condition parameters, must ensure a change in the superheat and subcooling, *e.g.* change in condenser inlet temperature, humidity, flow rate, condenser or evaporator inlet temperatures, or any combination of these variables. If the feature is negative there is an undercharge in the system, positive value indicates an overcharge in the system.

According to Li & Braun (2007), this feature is relatively independent of operating conditions and almost uniquely dependent on refrigerant charge. In addition, it is applicable to expansion organs with a fixed area and a variable expansion area, such as TXV. Li & Braun (2009) determined that for fixed orifice (FXO) expansion valve and TXV, is estimated to be 1/2.5. On the other hand, the coefficient for electronic expansion valves (EEVs) is equal to zero, since the superheat of a system is kept constant with such devices.

The difference in superheat and subcooling indicates a fault related to refrigerant charge in the system. In the work of Li & Braun (2009), Eq. (A.**4**) was modified in order to quantify the deviation from the nominal charge level. Furthermore, Kim & Braun (2015) added another term to the equation, which estimates charge deviation that incorporates vapor quality, in order to adapt the equation better to variable speed compressors and more extreme operating conditions, such as severe overcharge or very

low ambient temperatures. The validity of equation (decoupling feature) is when the charge deviation ranges from 60 to 140%. Outside of this range, the precision suffers, as well as when the compressor speed is relatively low in order to achieve very low subcooling and superheat. Kim & Braun (2015) suggested a modification in the equation and extended the validity of the model to 50 to 150% of charge deviation. However, the modifications and adjustments mentioned above complicate the implementation of the method on-field, due to their requirement of additional quantities that are difficult to measure on-field, such as vapor quality, or the requirement of additional data from the manufacturer making the method system specific.

A.3 Conclusions

A promising method based on the **decoupling-feature diagnostic method** is presented. Decoupling features required to measure each individual fault along with the necessary temperature and virtual sensors are presented in Table A.1.

Table A.1. *Fault decoupling features, required temperature measurements, and virtual measurements*

Fault	Decoupling feature	Temperature measurement	Virtual measurement
Condenser fouling	$\dot{V}_{ca}$	T_{cao}, T_{cai}, $T_{r,cond,i}$, $T_{r,cond,o}$	$P_{r,cond}$, $P_{r,evap}$, $\dot{m}$
Evaporator fouling or frost accumulation	$\dot{V}_{ea}$	T_{eao}, T_{eai}, $T_{r,evap,i}$, $T_{r,evap,o}$	$P_{r,cond}$, $P_{r,evap}$, $\dot{m}$
Refrigerant undercharge or overcharge	$\Delta T_{sc\rightarrow sh}$	$T_{r,cond,o}$, $T_{r,comp,i}$	$P_{r,cond}$, $P_{r,evap}$

The benefits of the method include on-field applicability, low calculation effort, low implementation cost, and its capacity to adapt to numerous vapor compression cycles, since fault detection is based on physical phenomena of thermodynamic cycles. This is mainly achieved with virtual sensors. The primary inconvenience of the method is the fact that it relies on reference values provided by the manufacturer or obtained by testing the HP in a laboratory. On the other hand, methods that do not require manufacturer data demand extensive and costly learning periods, thus, making them less versatile and less convenient for on-field use of already-installed machines. Manufacturer's data required for the decoupling feature method is typically readily provided with equipment.

APPENDIX B

EXPERIMENTAL TECHNIQUES FOR COMPRESSOR THERMAL ANALYSIS

The thermal behavior inside the compressor is yet to be understood. Thorough modeling of compressor thermal profile requires extensive resources due to many complex phenomena occurring inside the compressor, mainly as a result of the presence and distribution of oil and the flow dynamics of the refrigerant gas. The task becomes even more difficult, and specifically costly, if the thermal profile is required for a wide-range of operating conditions and compressor types.

In order to acquire the necessary experimental data to determine correlations that describe the thermal behavior of a compressor, several techniques can be employed. It must be noted that the most straightforward and conventional way to perform experimental measurements is to use thermocouples. Other techniques to determine compressor thermal behavior is using heat flux sensors and infrared cameras. Table B.2 is a compilation of different techniques along with their methods of employment, advantages and disadvantages. Such measurement approaches were found to be used by other researchers.

It must be stressed that determining the refrigerant compressor thermal profile through experimental techniques is challenging, since hermetic compressors are typically tightly assembled (compact) machines with a large number of geometrically complex components besides the essential components, such as various coils, filets and pins, and complicated flow dynamics inside. However, one of the main difficulties encountered when performing such analysis is the fact that some important components from the heat transfer point of view are in motion. For instance, the rotor, which primarily consists of an assembly of magnets, rotates, as well as the crankshaft. Also, the gap between the rotor and stator is small; hence measuring the rotor and stator temperatures separately seems to be complicated if not impossible. Therefore, a great deal of studies encountered seemed to lack experimental information of many interior components, such as the rotor-stator assembly and crankshaft. It can be speculated that it is mainly due to the difficulty of measuring the temperatures of rotating surfaces. In some studies the temperature of the stator-rotor assembly was determined as a whole, referring to the “motor temperature”, however, with no explanation of how and which part of the motor assembly was actually measured.

Measurements are typically obtained from such parts of the compressor, as the inlet, outlet, exterior shell temperature distribution and rarely some interior locations, such as the refrigerant temperature at the suction cavity of the compression chamber.

Table B.2 *Measurement techniques used to determine compressor thermal behavior*

	Technologies		
	Thermocouples	Infrared cameras	Heat flux sensors
Description:	• Consists of two conductors that generate a voltage when a temperature difference occurs	• Emissivity of the surface is estimated and the temperature field is determined	• Heat flux determined from the temperature difference between opposite sides of a separator material attached to a surface
Advantage:	• Very simple and straightforward technique to directly thermally map the compressor	• Provides temperature values over larger surface areas • Little impact on the heat transfer process due to a no-contact technology	• When combined with temperature measurements, the thermal conductances of each component can be derived directly
Disadvantage:	• Slow response time does not allow to register the instantaneous fluctuations of the gas temperature • An intrusive technique that can affect the flow dynamics of the fluid – location of the thermocouple must be considered carefully • Complex geometry of the components	• Poor accuracy when the surface emissivity is non-uniform • Measuring internal components of the compressor (use of infrared transparent windows are mandatory)	• Limited space available inside the compressor • Rotation of the components • Thermal contact resistance between the surface and the sensor reflects poorly on the accuracy • Possible difference in the radiation properties (emissivity) between the sensor surface and the actual component surface

	provokes unequal distribution of temperature • Rotation of the components complicates the analysis (typically, thermocouples are attached to wires) • Limited amount of space inside the compressor		• Lubricating oil with refrigerant can be an aggressive environment for heat flux sensor materials in hermetic compressors

APPENDIX C

ADDITIONAL NUSSELT NUMBER CORRELATIONS

C.1 Nusselt number correlation for the stator-rotor gap

The turbulent Taylor-Coutte flow (flow between two rotating cylinders) with an axial throughflow has to be considered in order to calculate the heat transfer coefficient of the stator-rotor gap. A correlation was found that represents such flow between two concentric cylinders with the inner one in rotating motion and the outer one stationary Bouafia *et al.* (1988). The heat transfer correlation takes into account the fact that the inner cylinder, in this application the rotor, is heated. The inner surface of the stator is assumed to be perfectly smooth. The correlation for the average Nusselt number is calculated as follows:

$$\overline{Nu}_{D_h} = 0.025 Re_{eff}^{0.8} \qquad (\mathbf{1.1 \cdot 10^4 < Re_a < 3.1 \cdot 10^4; 500 < Re_t < 3.1 \cdot 10^4}) \tag{C.6}$$

where Re_{eff} is the effective Reynolds number obtained from the following equation (Bouafia *et al.*, 1997):

$$Re_{eff} = \sqrt{Re_a^2 + \alpha Re_t^2} \tag{C.7}$$

where α is the weighting coefficient set as 0.5 (optimal value) for a rotor-stator assembly, Re_a is the axial Reynolds number and Re_t is the tangential Reynolds number:

$$Re_a = \frac{v_a x}{\nu} \tag{C.8}$$

where v_a is the axial velocity.

$$Re_t = \frac{\Omega R_{ext} x}{\nu} \tag{C.9}$$

where R_{ext} is the exterior radius of the rotor. The characteristic length, x, is the hydraulic diameter in this case, calculated from:

$$D_h = \frac{4A}{p} \tag{C.10}$$

where A is the cross-sectional area of the flow and p is the wetted perimeter of the cross-section.

C.2 Nusselt number correlation for the stator-shell gap

Heat transfer between the shell and stator can be approximated by a correlation used for heat transfer between two concentric cylinders (Mills, 1999):

$$Nu_x = 0.0605 Ra_x^{1/3} \qquad (C.11)$$

where Ra_x is the Rayleigh number for which the gap width is the characteristic length. It is assumed that convection in such regions is natural, since fluid passes with a low velocity in the gap. In this case both cylinders are station

Résumé

Actuellement, la plupart des fabricants de pompes à chaleur (PAC) fournissent les valeurs de coefficients de performances (COP) obtenus en laboratoire en conditions contrôlées et standardisées. Une méthode prometteuse, appelée méthode de mesure des performances dans la suite, d'évaluation des performances de PAC in situ, basée sur le bilan énergétique du compresseur, a été présentée par Tran et al. (2013). Cette méthode détermine le débit de fluide frigorigène et est compatible avec différents types de PAC, notamment air-air, et des cycles frigorifiques plus complexes.

Tran et al. (2013) ont déterminé que l'incertitude sur l'évaluation de pertes thermiques du compresseur contribue à hauteur de 40% sur l'erreur d'estimation de la puissance thermique. L'objectif de cette thèse est d'établir une méthode simplifiée quant à l'instrumentation pour mesurer les pertes thermiques in situ. Pour cela, deux modèles numériques détaillés sont développés afin d'examiner la distribution de température sur l'enveloppe de deux types de compresseurs, scroll et rotary. Les mesures expérimentales fournies par un fabricant de compresseurs, Mitsubishi Heavy Industries (MHI), sont utilisées pour calibrer et valider les modèles numériques. Ces derniers permettent de définir deux protocoles de mesures différents pour les deux compresseurs. Ensuite, le protocole établi pour le compresseur rotary est intégré dans la méthode de mesures des performances. Les puissances thermiques calculées sont comparées avec des valeurs de référence, obtenues à partir d'un prototype en banc d'essai à EDF Lab Les Renardières.

Mots Clés

Pompes à chaleur, coefficient de performances, rotary, scroll, puissance calorifique, CFD, modèle numérique, transfert de chaleur, compresseur, pertes thermiques, incertitude, in-situ, fluide frigorigène, cycle thermodynamique

Abstract

Currently, most heat pump (HP) manufacturers provide coefficient of performance (COP) values obtained in laboratories under standardized controlled operating conditions. These COP values are not necessarily representative of those obtained on-field. A promising method, referred to as the performance assessment method, that measures heat pump performances in-situ based on compressor energy balance, was presented by Tran et al. (2013). The method determines refrigerant mass flow rate and has the capability of measuring performances of various HP types, such as air-to-air, as well as more complex refrigeration cycles. The method abstains from intrusive measurements, and is, therefore, perfectly suitable for in-situ measurements.

As shown in the work of Tran et al. (2013), compressor heat losses account for 40% in the final uncertainty of performance values obtained with the performance assessment method. The objective of this thesis is to establish a rather simplified measurement method, in terms of instrumentation, that is used to determine compressor heat losses in-situ. For this purpose two detailed numerical models for assessing the temperature fields of the scroll and rotary compressor shells were developed. Experimental measurements obtained with the help of compressor manufacturer, Mitsubishi Heavy Industries (MHI), are used to validate and calibrate the numerical models. The developed numerical models allow to define two different measurement protocols for both compressors. Established compressor heat loss protocol for rotary compressor is then integrated in the performance assessment method and the obtained heating capacities are compared with reference measurements in an experimental test bench in EDF Lab Les Renardières.

Keywords

Heat pump, coefficient of performance, rotary, scroll, heating capacity, CFD, numerical model, heat transfer, compressor, heat losses, uncertainty, refrigerant, thermodynamic cycle